Optimization of a Turboramjet Hot Section with an Interstage Turbine Burner

by

Caitlin R. Thorn

A dissertation submitted to the Graduate Faculty of
Auburn University
in partial fulfillment of the
requirements for the Degree of
Doctor of Philosophy

Auburn, Alabama
May 7, 2016

Approved by

Roy Hartfield, Chair, Walt and Virginia Woltosz Professor of Aerospace Engineering
John Burkhalter, Professor Emeritus of Aerospace Engineering
David Scarborough, Assistant Professor of Aerospace Engineering
Brian Thurow, W. Allen and Martha Reed Associate Professor of Aerospace Engineering

Abstract

A turbine based combined cycle engine (TBCC) is currently in development for use in the SR-72 reconnaissance aircraft, the successor to the SR-71 Blackbird. With a proposed operating range of Mach 0-6, there is a need for an efficient transition from the turbine engine to the ramjet cycle. This work introduces an interstage turbine burner (ITB) in between the high and low pressure turbine stages of a turboramjet model and utilizes a hybrid genetic and evolution strategies algorithm in conjunction with a multi-block high fidelity flow solver to aerothermally optimize the three-dimensional turbine blade geometry of the high and low pressure turbines stages within the TBCC model. This allows for an engine performance improvement in thrust and thrust specific fuel consumption (TSFC) and thus a more efficient transition to the ramjet cycle. The hybrid genetic and evolution strategies algorithm used in this research utilizes a Navier-Stokes viscous flow solver and allows for a two stage turbine optimization within six days utilizing a computer cluster and parallel processing. The viscous flow solver performs a multi-block optimization in which a turbine stage is optimized simultaneously versus a serial optimization in which the stator is first optimized, followed by the rotor. Results indicate the multi-block optimization method provides superior results to that of the sequential row optimization method. A turboramjet or TBCC engine is modeled in Numerical Propulsion System Simulation (NPSS) utilizing known F100 engine parameters as a baseline validation case for the turbine cycle of the engine. An aerothermal hot section optimization is performed in which an ITB is inserted between the high and low pressure turbine stages and the geometry of

the turbines are three-dimensionally optimized within the NPSS model utilizing thrust and TSFC as the objective functions. The hot section optimization of the turboramjet results in a 2%-6% increase in thrust and 6%-8% improvement in TSFC over the baseline turboramjet engine at the three design optimization points. The method of optimizing the turbine stages within the engine model architecture proves superior to the method in which the turbine stages are independently optimized aerothermally outside of the engine architecture. This work provides for a novel method in which to optimize the hot section of a turboramjet engine, resulting in a more efficient transition to the ramjet cycle and improved results over conventional turbine optimization methods.

Acknowledgements

There are many people to thank for the successful completion of this work. I would first like to thank Dr. Hartfield, for always having an open door and being more than willing and able to help when roadblocks were encountered. I would also like to thank my committee members, Dr. Burkhalter, Dr. Thurow, Dr. Scarborough, and Dr. Carpenter, for their insights and knowledge in the completion of this work. Thanks are also due to the graduate students at Auburn, for being helpful with any and all issues. Also, much gratitude is due to Bobby Watson and especially Jim Clark for their help with the computer cluster. Jim's prompt weekend and evening response to emails was invaluable in completing this work on time. And finally, thanks go to my husband, Knox, and children, Jackson and Avery, for their continued support in the completion of this research.

Table of Contents

List of Figures

List of Tables

List of Symbols

A	Area
a_0	Speed of Sound
Bi	Biot Number
C	Characteristic Variable
c_p	Specific Heat
e	Polytropic Efficiency
F_c	Centrifugal Force
F	Thrust
f	Fuel/Air Ratio
h	Enthalpy
I	Moment of Inertia
K_{cool}	Cooling Flow Factor
$\dot{m}$	Mass Flow Rate
M	Moment
p	Static Pressure
p_0	Total Pressure
P	Coordinate
e	Polytropic Efficiency
q	Heat per Unit Mass

Q	Heat
r	Radius
R	Specific Gas Constant
T	Static Temperature
T_0	Total Temperature
Tt_4	Burner Exit Temperature
V_9	Exit Velocity
V_{19}	Fan Exit Velocity
v	Velocity
w	Weight
$\dot{W}$	Power
γ	Ratio of Specific Heats
ε	Emissivity
ξ	Turbine Work Distribution
η_{int}	Internal Cooling Efficiency
η_s	Isentropic Efficiency
θ	Theta
λ	Diffusion
π_c	Compressor Pressure Ratio
ρ	Density
σ	Stress
τ_c	Compressor Temperature Ratio
τ_f	Fan Temperature Ratio

τ_r	Freestream Temperature Ratio
τ_λ	Burner Temperature Ratio
ϕ	Cooling Air Mass Flow Rate
ω	Rotational Speed

List of Abbreviations

ANN	Artificial Neural Network
AUSM	Advection Upstream Splitting Method
BPR	Bypass Ratio
CFD	Computational Fluid Dynamics
COTS	Commercial Off the Shelf
DMRJ	Dual Mode Ramjet
ES	Evolution Strategies
FEA	Finite Element Analysis
FPR	Fan Pressure Ratio
GA	Genetic Algorithm
HPCC	Virtual Symmetric Multiprocessing High Performance Computing
HPT	High Pressure Turbine
ITB	Interstage Turbine Burner
LPT	Low Pressure Turbine
MDO	Multidisciplinary Design Optimization
NASP	National Aerospace Plane
NASA	National Air and Space Administration
NPSS	Numerical Propulsion System Simulation
NURBS	Non-Uniform Rational Basis Spline

OPR	Overall Pressure Ratio
QRBC	Quadratic Rational Bezier Curve
SCRAM	Supersonic Combustion Ramjet Missile
SSTO	Single Stage to Orbit
TBCC	Turbine Based Combined Cycle
TSFC	Thrust Specific Fuel Consumption
2-D	Two-dimensional
3-D	Three-dimensional

Chapter I

Introduction

Since its advent in the early 20th century, gas turbine engines have become a fundamental component for power generation, playing an essential role in heavy frame industrial applications and aeroderivative designs due to its high power-to-weight ratio. Gas turbine technology has steadily advanced and continues to evolve, emphasizing gains in efficiency as a means of producing more power with less fuel. This is particularly important in aircraft engines as a typical passenger plane burns approximately one gallon of fuel per second, and jet aircraft can burn more than four times that amount. With the United States Air Force spending 84% of its total energy consumption on jet fuel[1] and commercial airlines spending one-third of their operating costs on jet fuel, just a small increase in aircraft efficiency could result in millions of dollars saved per year. Component optimization, engine design, and higher engine operating temperatures contribute to increased engine efficiency. Such research is particularly important for engines operating at supersonic and hypersonic speeds in which large amounts of fuel is burned in a short period of time. There is a growing desire for hypersonic vehicles in the commercial and military sectors in which speed will allow for the faster transportation of goods as well as increase the effectiveness of reconnaissance vehicles and tactical missiles. The focus of this research is optimizing the revolutionary SR-72 engine, a reconnaissance vehicle currently in development with a proposed operating Mach number range of 0-6.

In November 2013 Lockheed Martin confirmed its development of a new hypersonic reconnaissance aircraft, the SR-72,[2] to serve as the successor to the SR-71 Blackbird, which was

retired in the late 1990s. Developed in the 1960s and operational for three decades, the SR-71 was a long-range strategic aircraft capable of flying at speeds over Mach 3.2 and at altitudes as high as 85,000 feet. The aircraft utilized a turboramjet engine and still holds the record as the fastest air-breathing aircraft. The SR-72, dubbed the "son of the blackbird," is proposed to pick up where the SR-71 left off, filling the gap between current surveillance aircraft that can loiter for long periods of time, but don't have the ability to transit to a new area quickly. With the advancement of aircraft detection technology, speed may very well be the next aviation advancement to counter emerging threats. However, designing an engine with a proposed operating range of the subsonic, supersonic, and hypersonic regimes does not come without significant challenges. A turbine based combined cycle engine (TBCC) must be utilized to employ a turbine based cycle at subsonic speeds and then transition to a ramjet cycle at high supersonic and hypersonic speeds. Due to the challenging nature and expense of a complete new engine design, the use of a commercial off the shelf (COTS) turbine engine is highly desirable before transition to the ramjet cycle. The problem lies in the fact that current engine technology is suitable for speeds up to Mach 2.5. At speeds higher than this, the turbine inlet temperature exceeds the material limits of the turbine blade. The SR-71 engine design bypassed air around the final compressor stage in order to reach Mach numbers above 2.5, however, this required a third duct and is not desirable for the proposed dual-mode ramjet (DMRJ) for the SR-72. To overcome this dilemma, a more efficient turbine engine is requisite to increasing the operating Mach number closer to Mach 3.0 at which the ramjet cycle can take over. For this research, it is proposed to increase this operating Mach number in two ways: the first being implementing an interstage turbine burner between the high pressure and low pressure turbines and the second being performing a complete three-dimensional turbine stage optimization.

1.1 Literature Review

Before the objectives and research goals of this paper can be discussed, a thorough literature review on the three separate components that compose of this research is warranted. The history of the hypersonics program and previous investigations in the development of turbine based combined cycles is discussed. In addition, a review of gas turbine blade design and optimization methods as well as past research in these areas is presented. And finally a discussion of the relatively new concept of interstage turbine burners and research conducted in this area is investigated. Based on this review, objectives for this research are presented and validated.

1.2 History of Hypersonics

Hypersonics has many space launch, civil, and military applications. Space launch applications include using an air-breathing engine for a Single-Stage-To-Orbit (SSTO) to reduce operating costs and improve safety. Cost models indicate that up to one order magnitude reduction in cost is possible by using oxygen from the atmosphere rather than storing it on board. Safety benefits include the ability to abort the mission over most of the flight with horizontal takeoff and powered landing capabilities. Civil applications include a hypersonic vehicle that can transport goods and people at hypersonic speeds. And perhaps the most feasible application for hypersonics is that for the military, to include global range, tactical missile, and high speed reconnaissance aircraft.

With continual advances in radar and detection technology, some say that speed is the new stealth for reconnaissance aircraft. For this reason, it is desirable for a stealth aircraft to reach speeds higher than Mach 3.3, the current speed record for an air-breathing aircraft. To

reach speeds of this nature, an engine with no moving parts must be utilized as the engine temperature exceeds the limits of composite materials. A ramjet engine cycle is one in which the compression of the air intake is achieved through the inlet by the speed of the supersonic vehicle. The freestream air slows to subsonic speeds through a normal shock as it enters the combustor at an increased temperature and pressure. The air is ignited and accelerates through a nozzle at supersonic speeds, producing thrust. At flight speeds of around Mach 6, these increases in temperature and pressure make it inefficient to slow the freestream air to subsonic speeds for combustion. For this reason, the flow is slowed to low supersonic speeds as it enters the combustion. This engine cycle is termed a supersonic combustion ramjet or scramjet.

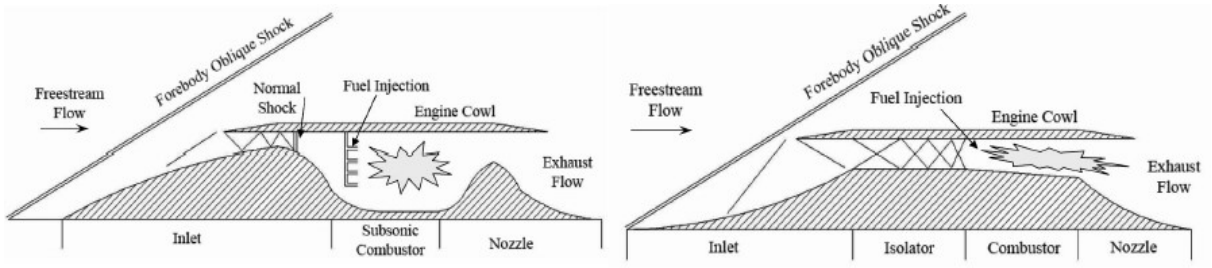

(a) **(b)**

Figure 1.1. Schematic diagram of ramjet (a) and scramjet (b) engine[3]

The hypersonic regime is defined by the speed at which the physics of flow is dominated by aerodynamic heating, and is generally thought to start at Mach 5. It is advantageous for an air-breathing aircraft to travel at speeds in the hypersonic regime rather than rocket powered craft as ramjets and scramjets have much higher specific impulse levels due to the simple reason that oxygen is collected from the atmosphere versus having to be stored on board. In addition, air-breathing engines produce higher engine efficiency, have longer powered range, and are completely reusable. It is for this reason that ramjet and scramjet research has been on-going

since the early 1930s with the first major program in the United States, the NASA Hypersonic Research Program, starting in 1964.

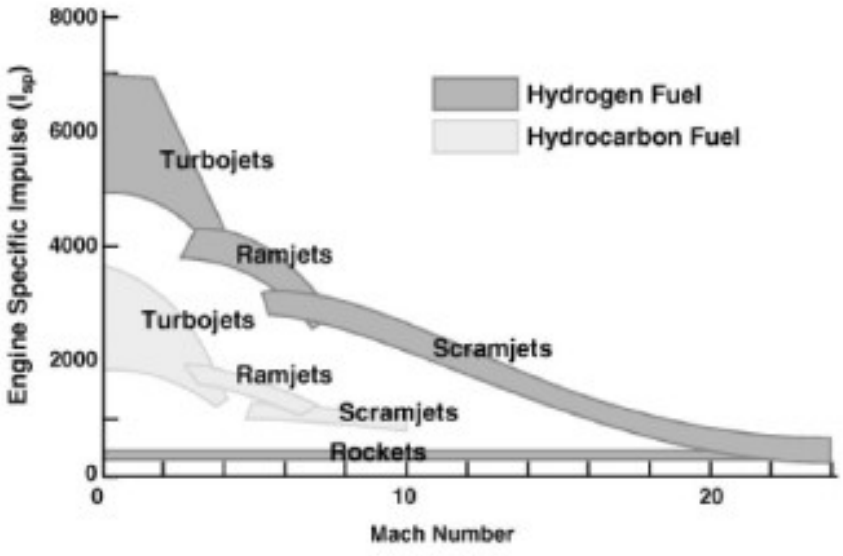

Figure 1.2. Specific impulse for various engines[3]

The aim of the program was to install a scramjet engine on the X-15 A-2 rocket research airplane to demonstrate flight-weight, variable geometry, hydrogen fueled scramjet technology, however, the program was ended in 1974 due to high costs. Another hypersonic program carried out during this same time frame was the Supersonic Combustion Ramjet Missile Program (SCRAM) from 1962-1977. This program, oriented towards ship-launched missiles, was successful in demonstrating the technology necessary to proceed into flight training. The next extensive hypersonic program in the United States did not start until 1989 and was National Aerospace Plane Program (NASP) aimed at developing a Single-Stage-To-Orbit (SSTO) hypersonic combined cycle air-breathing engine to propel a research vehicle, the X-30. Due to a lack of funding, the X-30 experimental SSTO was never built, and the program ended in 1994.

Although the NASP program was short lived, it served as an inspiration for a new major initiative by NASA to explore the performance of an airframe-integrated dual-mode scramjet-powered vehicle. The eight year Hyper-X program was a high-risk, high-payoff program as it undertook challenges never before attempted. The vehicle designed for this program, the X-43, was attached to a Pegasus Solid Propellant Booster and air-launched from a B-52 aircraft. The first successful flight of the X-43 occurred in March of 2004, reaching a speed of Mach 7. The aircraft reached a speed of Mach 10 in a second test flight in November 2004. Although setting a speed record, this successful flight test demonstration of a scramjet engine was the second program to do so, with the first belonging to the HyShot program in Australia in 2002.

Air Force Research Lab's Scramjet Engine Demonstrator program started in late 2003 with the goal of demonstrating powered flight with a hydrocarbon-fueled scramjet engine. The engine used for this program was originally developed by the short-lived HyTECH program in the early 1990s. The scramjet flight test vehicle was designated the X-51 and was propelled by solid rocket boosters to Mach 4.5 before being jettisoned and then accelerated to Mach 6 by the scramjet engine. Ground testing began in late 2006 with the first successful powered flight occurring in May 2010. The X-51 reached a speed of Mach 5 and flew for over 200 seconds, much longer than the 12 second flight of the X-43. Two subsequent unsuccessful test flights were performed in 2011 and 2012 and it wasn't until the fourth test flight in 2013 that the X-51 performed its first fully successful flight test. The X-51 and booster detached from a B-52H and was powered to Mach 4.8 before separating from the booster and igniting the scramjet engine. The X-51 accelerated to Mach 5.1 and flew 210 seconds before running out of fuel. With over six minutes of total flight time, the X-51 achieved the longest air-breathing hypersonic flight.

Following the end of the X-51 program, in November 2013, Lockheed Martin confirmed the development of a new hypersonic aircraft, the SR-72. Envisioned as an unmanned reconnaissance vehicle, the SR-72 would be the first aircraft capable of traveling in the subsonic, supersonic, and hypersonic regimes, with an operating range of 0-6 Mach. In order to successfully operate a vehicle through this Mach range, a combined cycle must be utilized.

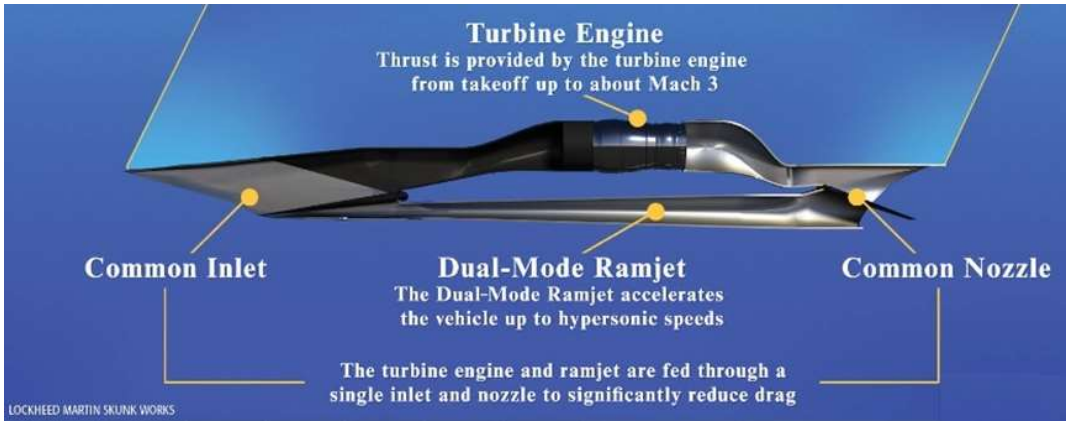

Figure 1.3. Proposed TBCC for SR-72[4]

A combined cycle is an engine which integrates components and operating modes of multiple engines into a single, common flow path in order to provide superior performance to an individual engine across a wider flight range. A revolutionary turbine based combined cycle (TBCC) is proposed in which a turbine engine would power the vehicle up to approximately Mach 2.5 at which the engine cycle would transition to a ramjet. In theory a TBCC provides an excellent solution, however, it does not come without significant design challenges. The most critical challenges of implementing the TBCC are a high Mach number turbine engine development and low Mach number dual-mode scramjet operation. Increasing the Mach number at which the turbine transitions to the ramjet mode would increase cycle efficiency considerably as a ramjet operates more efficiently above Mach 3.

Due to the challenge and expense of a developing a complete new engine design, in 2014 NASA tasked Lockheed Martin to study the viability of integrating an existing COTS engine with a very low mode Mach ignition dual mode ramjet (DMRJ) in the SR-72 concept. Research is on-going in this area with the objective of increasing the turbine operating range to above Mach 3 and developing an efficient transition to the ramjet cycle in the range of Mach 3-4.

1.3 Turbine Based Combined Cycles

One of the most critical challenges in the design and development of air breathing gas turbine engines lies in guaranteeing the propulsion system operates efficiently and effectively along a very wide operating range. As the Mach number approaches the range of 2.5-3.0, the temperature exiting the combustor is greater than the material limits of composite turbine blades. To mitigate this effect, in order to meet the requirement for a vehicle to operate from the subsonic to the hypersonic regimes, a gas turbine cycle must transition to one in which there are no moving parts to form a turbine based combined cycle or TBCC. The design of a TBCC system is very complex and although some work has been done to demonstrate the complexity and design issues of such a system,[5,6,7] there is limited research on the actual engine model itself. Clough[8] performed an optimization on a TBCC engine model, but the model is rather simple and the optimization rudimentary at best. According to the National Aeronautics and Space Administration (NASA), the most critical TBCC enabling technologies include mode transition, high Mach turbine engine development, and low Mach number dual mode scramjet operation.[9] Currently, the upper limits of a gas turbine engine is Mach 2.5. It is desirable to increase this number to above Mach 3 and preferably well in the range of Mach 3-4 for an efficient transition to the ramjet.[10] Figure 1.4 shows the specific fuel consumption of an ideal ramjet as the Mach number increases at sea level. This is a significant area of focus for this research.

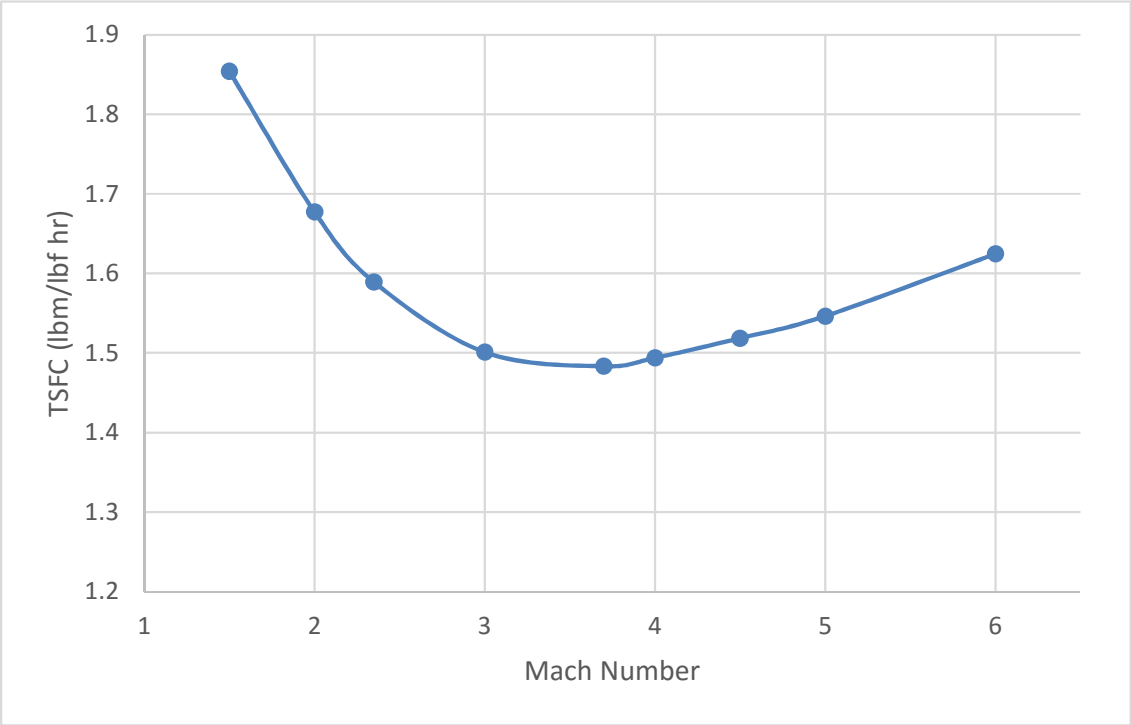

Figure 1.4. Specific fuel consumption vs. Mach number ideal ramjet at sea level.

Increasing the thrust and decreasing the thrust specific fuel consumption (TSFC) of the engine will in turn increase the transition Mach number of the TBCC.[11] By defining the initial flight Mach number and altitude as well as the fuel properties, turbine inlet temperature (Tt_4), and three design variables of the compressor pressure ratio (π_c), fan pressure ratio (π_f), and bypass ratio (α), one can use Eqs. (1.1)-(1.11) to solve for the thrust and TSFC in Eqs. (1.9) and (1.11) respectively.

$$R = \frac{\gamma - 1}{\gamma} c_p \tag{1.1}$$

$$a_0 = \sqrt{\gamma R T_0} \tag{1.2}$$

$$\tau_r = 1 + \frac{\gamma - 1}{2} M_0^2 \tag{1.3}$$

$$\tau_\lambda = \frac{T_{t4}}{T_0} \tag{1.4}$$

$$\tau_c = (\pi_c)^{(\gamma-1)/\gamma} \tag{1.5}$$

$$\tau_f = (\pi_f)^{(\gamma-1)/\gamma} \tag{1.6}$$

$$V_9 = a_0 \sqrt{\frac{2}{\gamma-1}\{\tau_\lambda - \tau_r[\tau_c - 1 + \alpha(\tau_f - 1)] - \frac{\tau_\lambda}{\tau_r \tau_c}\}} \tag{1.7}$$

$$V_{19} = a_0 \sqrt{\frac{2}{\gamma-1}(\tau_r \tau_f - 1)} \tag{1.8}$$

$$F = \dot{m}_0 a_0 \frac{1}{1+\alpha}\left[\frac{V_9}{a_0} - M_0 + \alpha\left(\frac{V_{19}}{a_0} - M_0\right)\right] \tag{1.9}$$

$$f = \frac{c_p T_0}{h_{pr}}(\tau_\lambda - \tau_r \tau_c) \tag{1.10}$$

$$TSFC = \frac{f}{(1+\alpha)(F/\dot{m}_0)} \tag{1.11}$$

The relationship of Mach number versus thrust and TSFC can then be plotted as shown in Figs. 1.5 and 1.6 respectively.

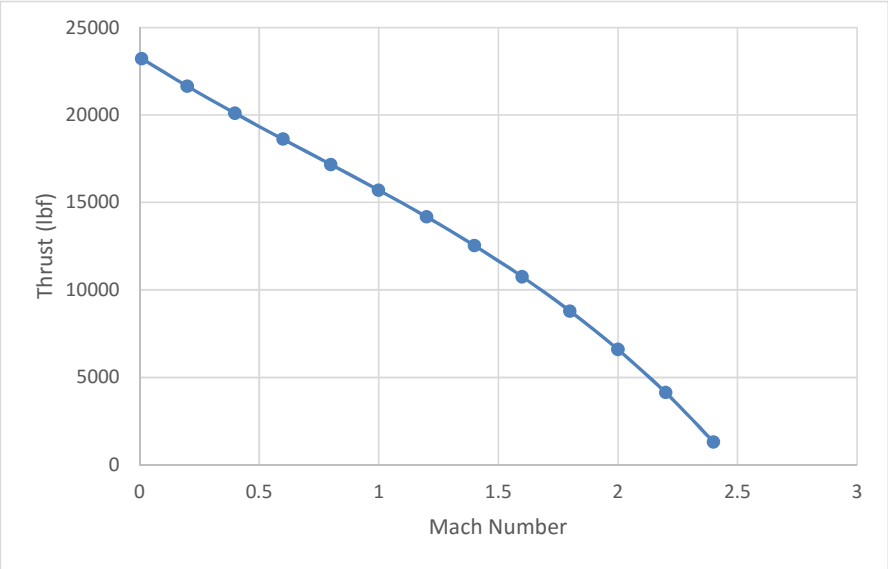

Figure 1.5. Ideal turbofan performance vs. Mach number at sea level for π_c=32.4 and π_f=3.55

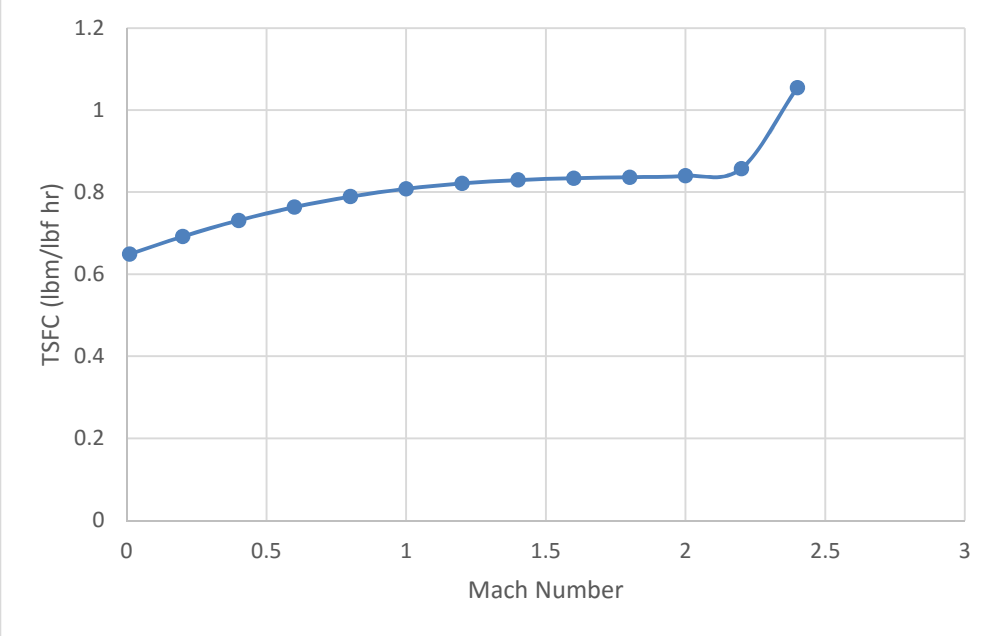

Figure 1.6. Ideal turbofan performance vs. Mach number at sea level for π_c=32.4 and π_f=3.55

As shown from the trend in Fig. 1.5, an increase in thrust will prove beneficial in allowing the turbofan cycle to increase its maximum Mach number prior to transitioning to the ramjet cycle.

Decreasing the TSFC does not display this same trend as the slope tends to zero as the Mach number approaches the supersonic regime, however, designing an engine for the lowest fuel consumption possible is an important design consideration in saving long term fuel costs and should still be considered in the engine design and optimization process.

1.4 Gas Turbine Flow and Turbine Blade Design

The flow in turbomachinery is three-dimensional, unsteady, compressible and highly complex as it involves laminar and turbulent flow regimes, stator-rotor interactions, vortical flows, flow separation, shocks, heat transfer, etc. In order to achieve a complete turbine blade optimization, it is imperative that a three-dimensional (3-D) optimization is conducted rather than a simple cascade analysis. Secondary flow, tip leakage, and boundary layer are features of the flow that are three-dimensional in nature and cannot be accounted for in two-dimensional (2-D) analysis or even quasi three-dimensional flow analysis. Simply performing an optimization on the 2-D airfoil geometry neglects the losses causes by the 3-D features of the flow and does not yield an optimal turbine blade design. In addition, optimizing a stator or rotor separately without taking into account the stator-rotor interactions may lead to a less than desirable stage performance. A simultaneous stage optimization is required to achieve an optimal stage geometry.

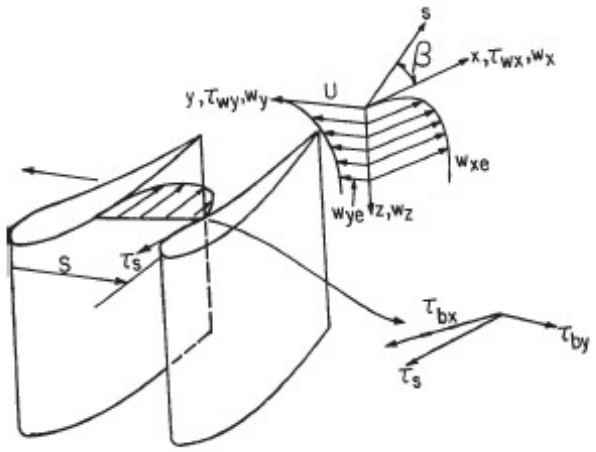

Figure 1.7. Three-dimensional boundary layer in turbomachinery flow[12]

Inverse design and design optimization are the two conventional design optimization techniques. The inverse design approach utilizes a prescribed blade performance to obtain the blade geometry solution. This method is very straightforward, however, prescribing "good" target design variables may prove challenging in 3-D blade design. In the design optimization method, the blade performance is prescribed with a set of objective functions restricted to design constraints. The design variables are then optimized for the best performance. This type of approach provides high flexibility and can be applied to problems with a large design space. This type of design optimization technique is applied to the current research.

1.5 Turbine Optimization Methods

A typical optimization routine for a turbine blade is an iterative process, utilizing a blade geometry, flow solver, and optimization algorithm. Generating a blade geometry is a rather quick and straightforward process with current computational power. The type of flow solver used may greatly influence the computational time required and the fidelity of solution achieved as there is

usually a trade-off between the two, with a higher fidelity solution (such as one achieved with a Navier-Stokes solver) requiring a significant amount of computation time as compared to a simple Euler code. The optimization algorithm employed is also an important choice in turbine optimization as certain methods are better suited than others at finding an optimal solution for the particular problem at hand. In addition, the type of algorithm used may also significantly influence computation time. It is important to choose a flow solver and algorithm that will yield a high fidelity solution in a reasonable timeframe. This will be a focus in the current research.

General optimization methods can be divided into deterministic and stochastic methods. The deterministic approach is a gradient based method which starts with a single design point and uses the local gradient of the objective function with respect to changes in the design variables to determine a search direction. This type of method is usually faster than stochastic methods, but runs the risk of being stuck in a local minimum for aerodynamic problems with usually have nondifferentiable and multimodal objective functions. Stochastic methods are evolution based algorithms that are robust for finding global optimum as they start with multiple design points over the entire design space and search for true optimums according to the objective function values through its use of selection, recombination, and mutation. When compared to other optimization methods, these evolutionary algorithms have shown to lead to better results in general for aerodynamic problems.

Popular evolutionary algorithms for use in turbine blade optimization include particle swarm optimizers, genetic algorithms, and evolution strategy. Particle swarm optimizers (PSO) are inspired by a swarm of bees or flock of birds. This method optimizes a problem by improving a candidate solution iteratively with regard to a given objective function. PSO optimizes a problem by moving a population of candidate solutions or particles around in the search space

according to the particle's position and velocity. Each particle's local best known position influences its movement and is also guided towards the best known positions in the search space, which are updated as better positions are found by other particles. This is the phenomenon which causes the swarm to move toward the best solutions. Although easy to implement with fairly fast convergence, PSOs are sensitive to initial input parameters, making them more at risk to fall into a local optimum.

Genetic Algorithms (GA) are search algorithms based on the principles of evolution observed in nature. The optimization mimics the process of natural selection by using techniques such as inheritance, mutation, selection, and crossover to achieve an optimal solution. The evolution starts with a population or generation of randomly generated individuals. In each generation, the fitness of each individual is determined based on a selected objective function. A new generation is then determined by a combination of selection, crossover, mutation, and elitism. First, an initial pool of candidate parents is created by either a roulette wheel or a tournament selection process. In roulette wheel, each candidate is assigned a portion of the wheel proportional to their current fitness value. The pool of candidate parents is then selected randomly from the wheel. The next generation, or offspring, is generated by a crossover technique in which two parents are selected from the pool at random and genes from each parent are combined to form a child. A certain proportion of the next generation of offspring is also generated by a random mutation from a randomly selected parent. Finally, the top few of the best performers in the previous generation are generally identically passed down to the next generation to ensure that the fitness solutions of each generation are preserved. GAs have proven successful in finding the global optimum in a very large search space and are not easily trapped

in a local minimum or maxima. However, they generally do require a large population size and can require a long computation time if parallel processing is not used.

Evolution Strategies (ES) algorithms are similar to GAs in that they operate according to evolutionary principles with the difference being that ES algorithms generate offspring for the next generation from 100% mutation from the most fit parent of the previous generation. After the designated number of offspring have been mutated from the parent solution, the solutions are evaluated and sorted and the most fit proceed to the next generation. The move operator, or the method of producing offspring, fluctuates in proportion to the fitness of the offspring as compared to the fitness of the parents. ES algorithms perform well with small population sizes and a relatively small number of design variables. However if the number of design variables is too large or the parent population is far from the global optimum, the algorithm has the possibility of getting stuck in a local minimum or maximum.

1.5.1 Previous Turbine Optimization Work

In recent years, a large amount of research activity has been devoted to turbomachinery optimization for both two-dimensional and three-dimensional analyses. Aerodynamic shape optimization is the most prevalent design optimization objective in the literature as a more efficient airfoil shape results in reduced fuel consumption for the same power output. The work of Dennis et al[13] used a GA with a viscous code analysis for a multi-objective optimization of a two-dimensional turbine cascade. The blade geometry was modeled with a B-spline and a binary representation of the 18 design variables was used in the GA. The computation utilized parallel computing and consumed a wall-clock time of 50 hours to complete the aerodynamic optimization. The work of Mengisu[14] used a GA with an artificial neural network (ANN)

surrogate model to substitute a computational fluid dynamics (CFD) model in an effort to reduce computation time. Many optimization constraints were implemented to include mass flow rate, inlet and exit angles, exit static pressure, chord and spacing, and thickness distribution. In addition, a non-uniform rational basis spline (NURBS) curve was used to model the two-dimensional blade geometry. Curriston[15] also used a NURBS curve to model blade geometry in his evolution strategies optimizer. The algorithm used in this work allowed for a reduced population size and thus computation time on a single processor. A multi-objective aerodynamic and thermal optimization was performed for a two-dimensional cascade.

Two-dimensional optimizations produce a blade geometry to account for the flow through the blade passage, however, they fail to fully optimize the annular turbine as three-dimensional flow phenomenon such as secondary flow, tip leakage, and 3-D boundary layer are unaccounted for. The work of Mohammed[12] accounts for these features using a three-dimensional design optimization of a turbine blade. A GA was used along with a surrogate ANN model. A NURBS curve was used to model the 3-D blade geometry and a structural check was used to validate blade feasibility. The two-dimensional airfoil profile was not optimized in this work. In addition, stator-rotor interactions were taken into account with the stator blade optimization carried out within the stage environment with a frozen rotor shape. Oyama[16] also performed a 3-D optimization using a unique real coded adaptive range genetic algorithm where the range is adapted according to the fitness of the current population. The routine optimizes four B-spline airfoil curves at four cross sections of the blade geometry. Parallel processing was utilized and the wall clock time was approximately two months for a complete rotor optimization. Chen[5] performed a more complete three-dimensional optimization using a GA with a viscous code analysis by using NURBS curves to represent the blade airfoil shape as well as

the lean, sweep, and twist stacking line. A complete stage optimization was performed with 99 design variables in 128 hours.

In summary, the examples of the published research work on turbine optimization demonstrate the feasibility of using numerical optimization methods such as GA and ES in conjunction with Navier-Stokes flow solvers and parallel computing to carry out a turbine stage optimization in a reasonable time period.

The review also indicates that there is a need for a turbine stage optimizer in which the stator and rotor are optimized simultaneously rather than sequentially due to stator-rotor interactions that significantly affect flow across the blades. In addition, the need for a complete 3-D blade optimization is evident as the vast majority of the published works neglect to perform both a two-dimensional airfoil optimization as well as a three-dimensional optimization to optimize geometry features such as blade sweep, stagger, and lean. Structural checks and additional constraints such as velocity distribution along the suction surface and the uncovered turning angle must be accounted for in the optimization routine to ensure complete blade feasibility and was generally not included in the research presented. A multi-objective optimization to include aerodynamic and thermal or aerothermal optimization is imperative to ensuring a maximum engine power output and was only performed in one of the works presented and only for a 2-D cascade. This work aims to bridge the gap among the turbine optimization literature to present a complete three-dimensional aerothermal turbine stage optimization with viscous flow analysis in an acceptable computation time.

1.6 Interstage Turbine Burner

The use of an interstage turbine burner (ITB) in current engine cycles is a relatively new area of research, but one that has some promising results, especially employed in supersonic vehicles. The thermodynamic Brayton cycle for both a conventional engine and one with an interstage turbine burner is shown in Fig. 1.8.

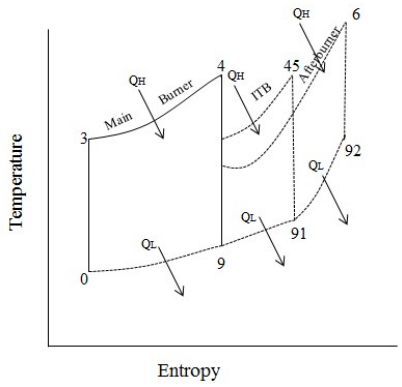

Figure 1.8. Brayton cycle for conventional engine, ITB, and afterburner

$$\eta_{T_{CC}} = \frac{Q_H - Q_L}{Q_H} = 1 - \frac{\sum Q_L}{\sum Q_H} = 1 - \frac{T_9 - T_0}{T_4 - T_3} \tag{1.12}$$

$$\eta_{T_{ITB}} = \frac{Q_H - Q_L}{Q_H} = 1 - \frac{\sum Q_L}{\sum Q_H} = 1 - \frac{T_{91} - T_0}{T_{45} - T_3} \tag{1.13}$$

$$\eta_{T_{AB}} = \frac{Q_H - Q_L}{Q_H} = 1 - \frac{\sum Q_L}{\sum Q_H} = 1 - \frac{T_{92} - T_0}{T_6 - T_3} \tag{1.14}$$

In a conventional Brayton cycle, the as the flow exits the combustor at state 4, the temperature decreases until it exits the nozzle at state 9. If an interstage turbine burner is inserted between the high pressure and low pressure turbines, the flow is then heated again in the ITB to state 45, thus increasing the entropy of the nozzle's flow and thus increasing thrust before entering the LPT and exiting through the nozzle at state 91. If an afterburner is used, the flow is heated to state 6 before exiting the nozzle at state 92. As can be seen from Eqs. (1.12)-(1.14), the cycle efficiency with an ITB is less efficient than that of a conventional engine, but more efficient than that of an afterburner. The extent of the tradeoff between efficiency and increased thrust is highly dependent on Mach number and engine type, and will be a focus of study in this research.

1.6.1 Previous Interstage Turbine Burner Investigations

The use of a combustor between the high pressure and low pressure turbines has been shown to increase the power and thermodynamic efficiency of a gas turbine engine. Liu and Sirignano[17] investigated the effects of incorporating an ITB on the performances on both a turbojet and turbofan via parametric studies at design point conditions. Their findings include an enhance overall pressure ratio, higher flight Mach numbers with high specific thrusts, an increase in turbine inlet temperature, and an increase in lower extraction from the low pressure turbine. Although findings are promising, the exact cooling flow requirement was unaccounted for in this research. Liew et. al[18] used a more refined methodology to investigated the performance of an ITB engine in a two-spool separate exhaust stream turbofan engine. The findings were consistent with those of Liu and Sirignano and show that an ITB engine produces a higher thrust with only a minimal increase in specific fuel consumption. The research found that the benefit of an ITB was enhanced as the flight Mach number increased. Soon[19] investigated the performance of an

ITB in an F-100 equivalent engine. Results indicate that the implementation of an ITB is a more favorable engine for supersonic cruising due to its lower specific fuel consumption when compared to that of the baseline F-100 engine with afterburner. Another advantage of including an ITB in an F-100 engine is to extend the operating envelope of the engine.

1.7 Multidisciplinary Optimization

Performance and cost are primary factors taken into consideration in the design and development of a jet engine. The present engine systems development process takes place at the original equipment manufacturer level, in which individual engine components are optimized independently of the engine system in which they are to be integrated. This practice may yield optimal engine component performance, but when integrated into an engine system may yield less than optimal engine performance, specifically in the areas of thrust and specific fuel consumption. Although model integration and engine system optimization is a critical process in achieving optimal engine performance, this practice is relatively lacking in the aerospace industry as compared to component optimization. Research efforts in the field of multidisciplinary optimization[20] (MDO) seek to close the gap between component and model optimization, with the majority of work being done as a master model approach[21] or cycle optimization.[22] Although these engine optimization techniques improve engine system performance through optimization of engine design variables such as BPR, fan pressure ratio, etc., they fail to optimize individual engine components at a detailed level. There is an inadequacy of research in this area, much to the detriment of engine design and performance. To ensure optimal component design for optimal engine performance, the component must be optimized within an engine architecture in which the optimization objective functions are the engine performance parameters.

1.8 Current Investigation

Based on the above literature review, there are several motivations for this current work. The first being a need for a complete three-dimensional turbine stage optimization, utilizing a viscous flow solver and parallel processing computational resources to arrive at an optimal stage solution in a reasonable timeframe. The second being a need to incorporate an interstage turbine burner into a turboramjet engine cycle to increase the efficiency and thrust of the turbine cycle. And the final motivation being a complete hot section optimization of a turboramjet engine cycle with an ITB, to include a high pressure turbine and low pressure turbine three-dimensional stage optimization. It is the goal of the current research to optimize the turbine stage geometry in such a way as to allow for an increase in maximum operable flight Mach number of the turbine cycle, allowing for a later and thus more efficient transition to the ramjet cycle.

1.8.1 Objective 1: Multi-row/Multi-stage Turbine Optimization

The first objective of the current research is to perform a simultaneous two-dimensional turbine stage optimization utilizing an evolution strategies algorithm. The stage optimization results are compared to a sequential row optimization in which the stator is first optimized, followed by the rotor using the exit properties from the stator as the inlet properties to the rotor. A Navier-Stokes flow solver is used in conjunction with parallel processing to achieve results in a relatively expedient timeframe. An aerothermal optimization is performed with the goal of increasing stage efficiency as well as optimizing the blade geometry to allow for a maximum turbine inlet temperature into the stage.

1.8.2 Objective 2: Three-Dimensional Turbine Stage Optimization

The second objective of the current research is to perform a complete three-dimensional aerodynamic and aerothermal stage optimization utilizing a viscous flow solver and parallel processing. A hybrid genetic algorithm and evolution strategies algorithm is used with a viscous flow solver and parallel processing. The stage two-dimensional airfoil geometry is optimized in addition to the lean, sweep, and twist of the rotor and stator. Additional constraints such as monatomic increasing Mach number, uncovered turning angle, and structural checks are implemented to ensure a feasible solution.

1.8.3 Objective 3: Turboramjet Hot Section Optimization

The final objective of this research is to model a turboramjet with an interstage turbine burner in the Numerical Propulsion System Simulation[23] (NPSS) code and pair it with the three-dimensional turbine stage optimizer. A complete hot section design optimization will be performed in which the high pressure and low pressure turbine stage geometries are optimized for a given engine objective function, which in this case will be maximum thrust and minimum TSFC. A complete aerothermal optimization is expected to allow for an increase in flight Mach number and turbine inlet temperature of the turbine, allowing for a more efficient transition to the ramjet cycle. A validation case for an F100-PW229 engine is first conducted to provide validation for the NPSS model and optimization scheme.

Chapter 2

Multi-row/Multi-stage Turbine Optimization

The turbine plays a critical role in the power extraction and efficiency of a gas turbine engine. With the development of these engines that can power aircraft to speeds approaching Mach 3, a highly efficient and effective turbine is imperative to maximize power output at reduced fuel consumption. Although today's turbines have achieved a very high degree of performance, there is a demand for even higher performing turbines as state of the art engines continue to evolve, as seen from the current development of the turbine based combined cycle engine with the proposed ability to transverse through the subsonic, supersonic, and hypersonic regimes.

Computation time required for an optimization can range from a few hours to many weeks, largely depending on the optimization method, type of flow solver, and the number of stages or blade rows being optimized. Generally, the flow solver type is the most influential element of the optimization process on computation time, with run times ranging from a few seconds for a simple potential solver to hours with a flow solver utilizing the full Navier-Stokes equations. Often times, a high fidelity solution is sacrificed for a faster optimization, yielding an adequate but less than optimal design. For this reason there is a need for an optimization method that yields optimal results in an acceptable timeframe. Much work has been done on optimizing turbine stages; however, computation time for a stage optimization has a wide range, with run times from recent work spanning from six days[24] to two months.[16] An evolutionary strategy optimization method[15] has been shown to drastically reduce optimization time with comparable

or improved results over similar type algorithms. This method coupled with parallel processing and a computational fluid dynamics code specifically designed for analysis of three-dimensional viscous flows in turbomachinery allows for a turbine blade stage multi-objective optimization in a reasonable timeframe.

The multi-block capability of the flow solver in this work allows for an analysis and thus optimization of all blade rows simultaneously. A successive blade row method is which an analysis of a turbine stage is performed by using the average flow properties from the exit of the stator as the inlet flow properties of the rotor has been used in many works;[25,26] however, may introduce many modeling issues. First, flow properties have a nonlinear relationship, making it impossible to define an average state across three-dimensional flow that maintains all original properties of the flow. Second, since the inlet velocity profile and mass flow develop as part of the solution it is generally not possible to match the spanwise distribution of properties between blade rows. In addition, this method of analysis may have higher implications for an optimization performed by way of the successive blade row method. By optimizing each stage individually and successively, the method fails to take into account the stator-rotor interactions and may not yield an optimized solution for the entire stage.

2.1 Optimization Method

The work of Curriston details a novel evolution strategies approach for two-dimensional turbine blade optimization that yields improved results in drastically less time than other genetic algorithms and particle swarm optimizers. This optimization method is used in this work and will be briefly described here. An evolution strategy algorithm is similar to a genetic algorithm in that it uses a population of solutions to produce offspring, sort the offspring based on an objective function, and select the best offspring to proceed as parents for the next generation; however, the

move operator, or the method of producing offspring is different. The method the optimizer uses to produce offspring and move solutions through the search space has a substantial effect on the algorithm's performance.

Control Point	Upper Surface		Lower Surface	
	x	y	x	y
1	0	0	0	0
2	0	0.1	0	-0.05
3	0.5	0.2	0.15	-0.1
4	0.7	-0.1	0.35	0
5	0.9	-0.3	0.8	-0.4
6	1	-0.65	1	-0.65

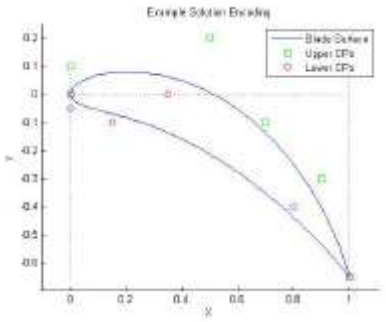

Figure 2.1. Control points and Bezier curve[15]

In this work, the optimizer uses a set of twelve control points to define two Bezier curves which make up a turbine blade's upper and lower surface, shown in Fig. 2.1. Bezier curves were chosen to represent the blade geometry due to its ability to represent almost any curve, ease of use, and small number of variables. This evolution strategies algorithm, shown in Fig. 2.2, mutates all of the offspring from the parent solutions through a random perturbation to the control points using a normal distribution and a user defined standard deviation. The standard deviation is adjusted with each generation according to the fitness value of the offspring as compared to the parents. If greater than one-fifth of the offspring are more fit than the parents, the standard deviation is increased to prevent the algorithm from being stuck in a local optimum. If less than one-fifth of the offspring are more fit than the parents, then the standard deviation is decreased to intensify the search and find better solutions. To prevent the method from stagnating, if the standard deviation gets too small, the standard deviation is reset to its initial value or some other designated number. This ensures that a global optimum is found instead of a nearby local optimum.

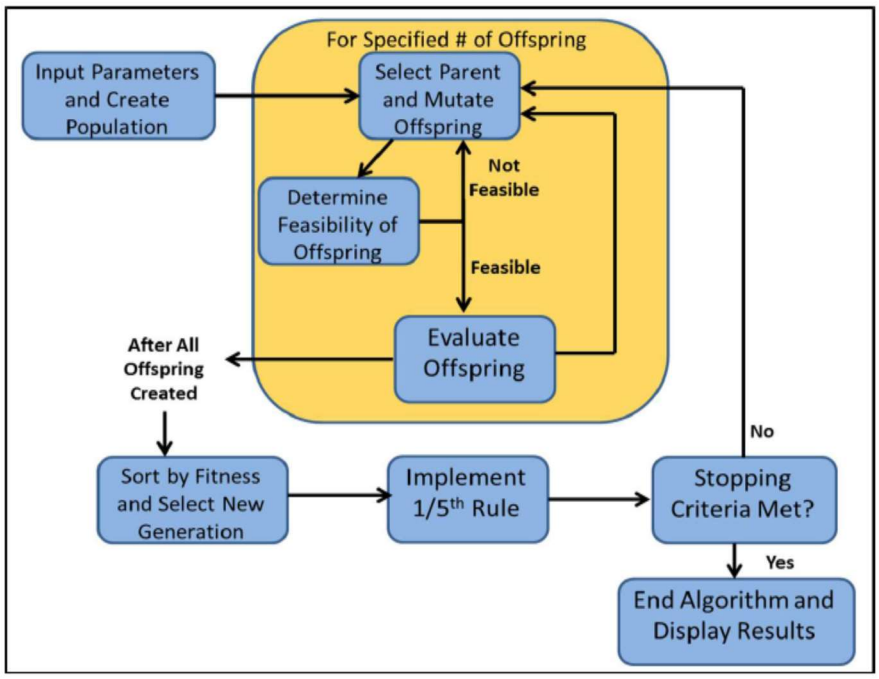

Figure 2.2. Optimizer flow chart[15]

The use of Bezier curves with the canonical move operator adjusting the standard deviation according to the one-fifth rule allows for the algorithm to search outward very effectively, thus negating the need for restricting the Bezier control points to certain regions in space. This may allow the algorithm to find better solutions more efficiently than other similar types of algorithms. Results indicate that the evolution strategies algorithm coupled with Bezier curve encoding is a very efficient and effective technique for aerodynamic optimization and may offer gains in thermal optimization as well. In this work, this 2-D blade shape optimization method is applied to a three-dimensional stacked turbine stage at the midspan.

2.2 Flow Solver

A critical part of any aerodynamic optimizer is the type of flow solver used. A CFD flow solver is highly desirable and yields the highest fidelity solution; however, computation time is extensive and can take on the order of weeks or even months to yield a fully optimized solution.

Faster, more efficient codes that neglect viscous effects are often preferred for optimization algorithms, yielding time savings at the expense of a less optimal solution. For this reason, a rapid optimization algorithm is essential in offsetting the increased computation time that comes with utilizing a viscous Navier-Stokes solver. Coupling a fast optimization method with parallel processing allows for comparable if not faster optimization time than simpler flow solvers, making it feasible to use a CFD flow solver as part of the optimizer.

Utilizing a single block CFD code for a multi-row/multi-stage optimization necessitates a successive analysis and optimization of isolated blade rows. In this case, the first blade row is optimized, and by using the average of the spanwise flow properties from the exit of the first blade row as the inlet boundary conditions for the second blade row, the next blade row is then optimized. This introduces a variety of modeling issues, both with optimization and flow analysis.

First, flow properties vary in the spanwise direction and are not well represented by average properties. An example of this phenomenon is shown using the space shuttle main engine two stage fuel turbine. The exit total pressure properties of each blade row were compared using a successive blade row analysis and a simultaneous blade row or average plane analysis. As seen from Fig. 2.3, the successive row analysis overpredicts total pressure loss in the spanwise direction, with as much as a 1% difference from the average plane method near the blade hub and tip. This differential is due to the characteristic boundary conditions used at the blade row interface, which is discussed below. From these results it is evident that a robust three-dimensional analysis or optimization is not feasible using average flow properties in the spanwise direction.

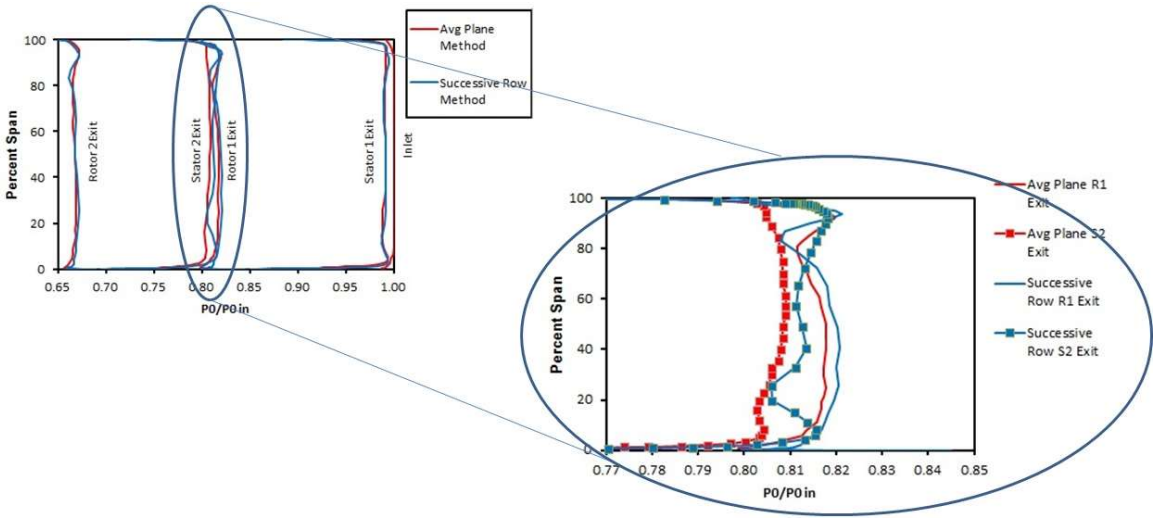

Figure 2.3. Spanwise pressure comparison between successive row method and average plane method.

Next, utilizing a single block flow solver forces a successive blade row optimization to be performed. Although improved results have been achieved and the optimizer proven effective in turbine optimization, optimal stage results may not be achieved with this method. The major problem with using a single block flow solver and thus a successive row optimization is not accounting for the stator-rotor interaction. The upstream stator blade shape affects the rotor performance. Optimizing the stator in absence of the rotor may have a negative effect on the rotor blade performance and result in a less than optimal stage performance.

In this work, a computational fluid dynamics code specifically designed for use with turbomachinery, SWIFT,[27] is used as the flow solver in the optimizer. SWIFT solves the thin-layer Navier-Stokes equations on body-fitted grids using an explicit finite-difference scheme. Viscous terms are included in the blade-to-blade and hub-to-tip directions, but are neglected in the streamwise direction using the thin-layer approximation. The AUSM+ scheme and Wilcox k-w turbulence model are used for this analysis. SWIFT allows for a multi-block capability solely

for use with turbomachinery problems. The code utilizes an averaging-plane method in which all blade rows are solved simultaneously, exchanging spanwise distributions of averaged flow quantities at a common grid interface between blade rows. This allows for spanwise consistency between blade rows.

The averaging technique and characteristic boundary conditions used at the blade row interface are described in detail in Chima's work and will be briefly summarized here. The general form of the non-reflecting one-dimensional unsteady boundary conditions developed by Giles[28] is used in SWIFT. By using the characteristic variables, Eq. (2.1) that correspond to an entropy wave, a downstream-running pressure wave, two vorticity waves, and an upstream-running pressure wave; the density, pressure, and velocity components can be solved in terms of their average conditions and speed of sound.

$$\begin{bmatrix} C_1 \\ C_2 \\ C_3 \\ C_4 \\ C_5 \end{bmatrix} = \begin{bmatrix} -\bar{c}^2 & 0 & 0 & 0 & 1 \\ 0 & \bar{\rho}\bar{c} & 0 & 0 & 1 \\ 0 & 0 & \bar{\rho}\bar{c} & 0 & 0 \\ 0 & 0 & 0 & \bar{\rho}\bar{c} & 0 \\ 0 & -\bar{\rho}\bar{c} & 0 & 0 & 1 \end{bmatrix} \begin{bmatrix} \rho - \bar{\rho} \\ v_x - \bar{v}_x \\ v_\theta - \bar{v}_\theta \\ v_r - \bar{v}_r \\ p - \bar{p} \end{bmatrix} \tag{2.1}$$

The inlet and exit boundary conditions for subsonic flow at the boundary are shown in Eqs. (2.2) and (2.3) respectively:

$$\begin{aligned} \rho &= \bar{\rho} + \frac{C_{5ex}}{2\bar{c}^2} \\ v_x &= \bar{v}_x - \frac{C_{5ex}}{2\bar{\rho}\bar{c}} \\ v_\theta &= \bar{v}_\theta \\ v_r &= \bar{v}_r \\ p &= \bar{p} + \frac{C_{5ex}}{2} \end{aligned} \tag{2.2}$$

$$
\begin{aligned}
\rho &= \overline{\rho} + \frac{-C_{1ex} + \dfrac{C_{2ex} + C_5}{2}}{\overline{c}^2} \\
v_x &= \overline{v}_x - \frac{C_{2ex} - C_5}{2\overline{\rho c}} \\
v_\theta &= \overline{v}_{\theta ex} \\
v_r &= \overline{v}_{rex} \\
p &= \overline{p} + \frac{C_{2ex} + C_5}{2}
\end{aligned}
\tag{2.3}
$$

where the $(\,)_{ex}$ implies extrapolation from the interior. For supersonic inflow at the inlet boundary, C_5=0 and all boundary values are equal to their specified values. For supersonic outflow at the exit boundary, C_5=C_{5ex}. The computational grid at the blade row interface overlap by one cell and is shown in Fig. 2.4, where the two grids are displayed vertically for clarity.

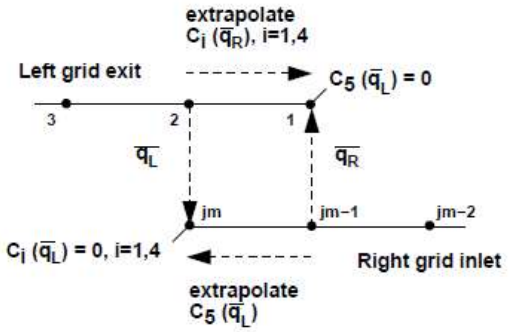

Figure 2.4. Implementation of characteristic boundary conditions at blade row interface[27]

The interior solution is first updated on a grid, then the solution next to the boundary is integrated circumferentially at each spanwise location. The average flow vector is stored for use in the boundary conditions on the neighboring grid. The average Mach number on the neighboring grid is checked for subsonic or supersonic conditions and the characteristic boundary conditions from Eqs. (2.2) or (2.3) are applied as appropriate.

Average flow properties are required at the boundaries for the characteristic boundary conditions. A mixed out average technique was used for this work and is described in detail by Denton.[29] The average can be derived by formally integrating the two-dimensional Euler equations in the y direction. Although many averaging techniques have been proposed to be used with the average plane method, the mixed out average has been shown to conserve mass well and produce no obvious differences between a kinetic energy averaging technique.

An essential part of this research utilizes the multi-block capability for an aerodynamic and aerothermal turbine stage optimizations. This allows for an efficient and effective simultaneous blade row optimization that includes a reliable analysis of the flow properties in the spanwise direction and between blades rows. The success of this method shows promise for a three-dimensional multistage optimization.

2.3 Design Optimization Problem

Due to the dearth of publicy availabe gas turbine data, an uncooled NASA axial turbine that was experimentally tested and described by Whitney et al.[30,31] was chosen for analysis. This work was selected as it offers well documented experimental one stage and two stage gas turbine data. In addition, the blades were specifically designed for engines with high temperature engine applications, while not noticeably impairing turbine aerodynamic performance, making for an ideal aerothermal optimization case. An aerothermal optimization was chosen to be performed in addition to an aerodynamic optimization as previous results indicate that the use of Bezier curves to represent blade geometry that may produce turbine blades that have better heat transfer characteristics at the leading edge, and thus may allow for an increase in turbine inlet temperature.

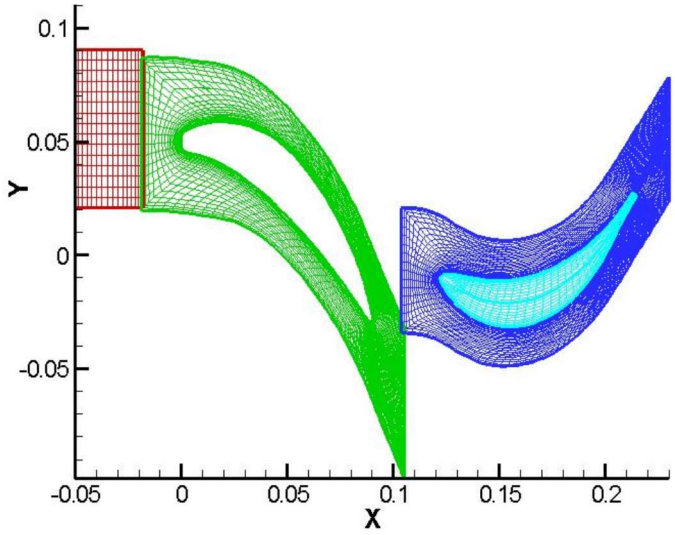

Figure 2.5. Grid for uncooled NASA turbine stage. Inlet H grid, C grids over blades, and O grid over rotor tip, 50% span

Since the optimization being performed for this work is on a 2-D blade shape, only the midspan blade geometry of the stage is considered and thus stacked in the spanwise direction. The work of Curriston has already proven the potential of the 2-D aerothermal optimization algorithm utilizing a successive blade row optimization method, thus the primary goal of this research is to perform a comparison of the multi-row simultaneous blade row optimization method to the successive isolated blade row optimization method. The midspan two-dimensional blade geometry of the stator and rotor were optimized simultaneously and compared to a successive row optimization using the midspan exit properties of the optimized stator as the inlet properties to the rotor. A single objective aerodynamic optimization in which the stage isentropic efficiency is optimized was performed for both the simultaneous row optimization method and the successive blade row optimization method, followed by a multi-objective aerothermal optimization with both methods. For both the aerodynamic and aerothermal optimizations, the two-dimensional midspan geometries of the stator and rotor were constrained

to the initial exit flow angles. The aerodynamic objective function used for the successive row optimization of the stator and rotor was the total pressure loss across the stator and the total to total efficiency across the rotor. The stage isentropic efficiency shown in Eq. (2.4) was used as the objective function for the simultaneous blade row optimization.

$$\eta_s = \frac{1 - \frac{T_{0,ex}}{T_{0,in}}}{1 - \left(\frac{p_{0,\mathrm{ex}}}{p_{0,in}}\right)^{\frac{R}{c_p}}} \tag{2.4}$$

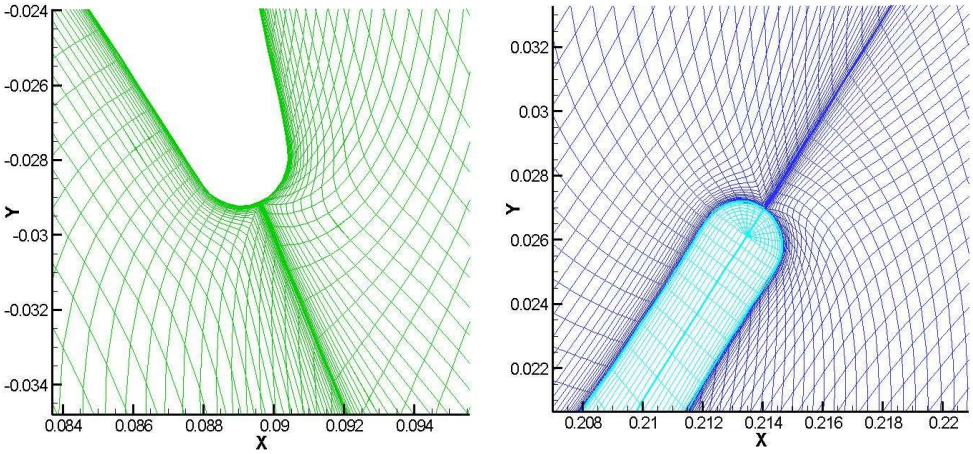

a) Stator **b) Rotor**

Figure 2.6. Trailing edge C-grid

The heat transfer model used for the aerothermal optimization is incorporated into the SWIFT analysis code. The code uses the k-w turbulence model with transition effects to predict the Stanton number at locations around the blade. The Stanton number may then be used to calculate the heat transfer coefficient around the blade. The heat transfer of the blade may be calculated from the convective heat transfer equation as shown in Eq. (2.5). For evaluating an optimized blade it can be assumed that the heat transfer into the blade and the blade temperature

are held the same, and therefore a change in the heat transfer coefficient will result in a change in allowable turbine inlet temperature. The new allowable turbine inlet temperature is shown in Eq. (2.6). Because the main goal of the aerothermal optimization is to investigate the trade-off between thermal and aerodynamic performance, the heat transfer objective function relates the heat transfer coefficient on the blade to the ideal engine power output. The ideal engine analysis discussed in Mattingly[32] provides a relation between a turbine inlet temperature increase and power increase and is shown in Eq. (2.7). By selecting a compressor ratio, a linear relationship can be established between the turbine inlet temperature ratio and the shaft power ratio, resulting in the heat transfer objective function in Eq. (2.8). A compressor ratio and initial allowable total temperature for this optimization was selected consistent with that of a high temperature engine. This rudimentary thermal analysis is meant to provide a simplified means in which to compare the successive and simultaneous optimization methods for a thermal analysis and mirrors the thermal objective function used in Curriston's work. Equation (2.8) along with the stage isentropic efficiency compose of the objective functions for the aerothermal optimization.

$$q = h(T_0 - T_{wall}) \tag{2.5}$$

$$T_{0,new} = \frac{h_{new}}{h_{old}}(T_{0,old} - T_{wall,\text{old}}) + T_{wall,old} \tag{2.6}$$

$$\dot{W}_{shaft} = \dot{m}_0 C_p T_0 \left(\frac{T_{0,turbine}}{T_{0,\infty}} \left(1 - \frac{1}{\pi_c^{\frac{\gamma-1}{\gamma}}} \right) - \left(\pi_c^{\frac{\gamma-1}{\gamma}} - 1 \right) \right) \tag{2.7}$$

$$\frac{\dot{W}_{new}}{\dot{W}_{old}} = 1.5935 \frac{T_{0,new}}{T_{0,old}} - 0.5935 \tag{2.8}$$

In addition to performance based optimization, "detailed airfoil design must include considerations of the internal flow characteristics not evaluated by performance analysis."[33] Two such aspects of turbine blade design were captured in the aerodynamic and aerothermal optimizations in the form of penalty functions, the first of which was ensuring a monatomic increase in velocity along the suction surface. It is generally accepted that suction surface velocity should increase smoothly from the inlet to a maximum value and then remain essentially constant over the aft portion of the blade. Such a distribution ensures a continually decreasing pressure which in turn slows boundary layer build up and minimizes flow separation. If the suction surface velocity decreased prior to the throat location, a penalty factor was applied to the objective function in proportion to the gradient of the velocity decrease. A limit was also applied to the suction surface diffusion, shown in Eqs. (2.9) and (2.10), to ensure the uncovered turning angle did not get so large as to cause additional total pressure loss at the end of the blade. A penalty function was applied in proportion to the suction side diffusion over 0.25.

$$\lambda_{stator} = \frac{\left(\frac{P}{P_0}\right)_{ex} - \left(\frac{P}{P_0}\right)_{\max V}}{1 - \left(\frac{P}{P_0}\right)_{\max V}} \tag{2.9}$$

$$\lambda_{rotor} = \frac{\left(\frac{P}{P_0}\right)_{ex} - \left(\frac{P}{P_0}\right)_{\max W}}{1 - \left(\frac{P}{P_0}\right)_{\max W}} \tag{2.10}$$

Structural considerations were implemented to account for a minimum blade thickness and blade area as well as a maximum surface distance to blade area ratio to ensure proper blade cooling. The maximum thickness to chord ratio for the original blade was also maintained for the optimization. While not intending to constitute a thorough structural analysis, this simple check

was completed as part of the feasibility routine shown in the optimizer flow chart, and ensured a feasible solution.

A single objective aerodynamic and multi-objective aerothermal optimization were performed using a simultaneous and successive row optimization method. Table 2.1 summarizes the optimization runs performed for this work.

Table 2.1. Optimization Runs

Run 1	Aerodyamic Optimization Simultaneous Row
Run 2	Aerodyamic Optimization Successive Row
Run 3	Aerothermal Optimization Simultaneous Row
Run 4	Aerothermal Optimization Successive Row

2.4 Results

The single stage viscous analysis optimizations for both the aerodynamic and aerothermal cases were completed using the two optimization methods detailed previously. The optimizer utilized eight offspring per generation for a total of 800 function evaluations over 100 generations. Considering that the geometry of each offspring is generated independently, a high performance computer cluster was utilized to compute the flow analysis of each offspring in the same generation simultaneously. In addition, parallel processing was utilized for the 3-D Navier Stokes solver, with a total of eight processors used for each flow computation. With eight processors used for each flow computation and the flow analysis of eight offspring occurring at the same time, 64 processors were used concurrently for each optimization. This allowed for an expedient optimization, with each generation taking approximately 22 minutes and the entire optimization computation time being 25.66 hours for the multistage aerothermal run and only 18.33 hours for the multistage aerodynamic run. The vast majority of the run time, 97%, was taken during the CFD analysis with the remaining 3% of the run time spent on the optimization.

The convergence history for the aerodynamic optimization is shown for the optimization in Fig. 2.7.

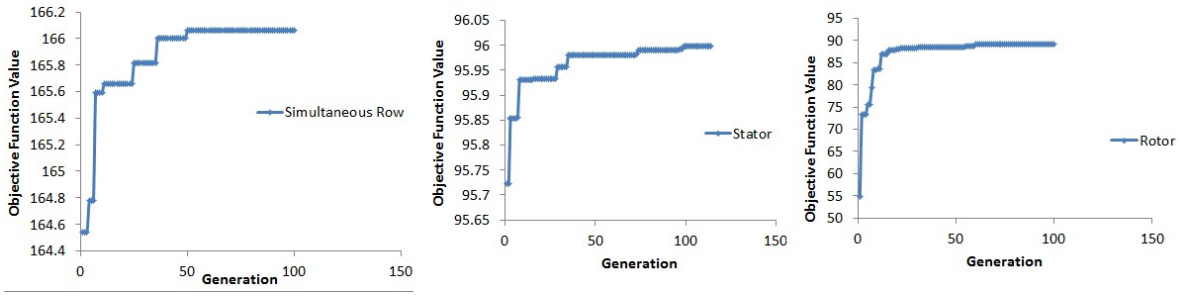

Figure 2.7. Convergence history for aerodynamic optimization

It is important that the optimizer achieve convergence within a similar time frame for repeat optimization runs. Good agreement among runs has been shown for a single row optimization and is also demonstrated for a simultaneous row optimization in this work. Figure 2.8 shows the optimization history for three different simultaneous row aerodynamic optimization runs. Good agreement was achieved, with each run converging within 50 generations. In addition, stage efficiency results were achieved within 0.1% of each other. For the purposes of this research, only the results of the first run will be shown here.

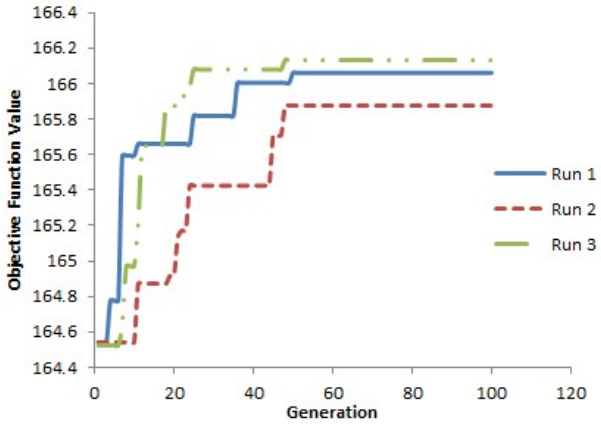

Figure 2.8. Convergence history simultaneous row aerodynamic optimization

2.4.1 Aerodynamic Optimization

A preliminary CFD analysis of the complete three-dimensional stage yielded an initial isentropic efficiency of 0.881 with a midspan value of 0.907. The overall initial isentropic efficiency matched well with the design value of 0.885. The stage was then modeled with the stator and rotor midspan cross sections to complete the two-dimensional analysis. A successive stator-rotor analysis of the initial stage yielded a midspan isentropic efficiency of 0.914. This increase from the multi-row analysis is expected as the successive row method is shown to overpredict the total pressure loss as shown from the SSME analysis.

Table 2.2. Aerodynamic optimization results

	Isentropic Efficiency			
Run	Initial		Optimized	
Simultaneous Row	0.907		0.912	
Successive Row	Successive	0.9138	Successive	0.9143
	Multirow	0.907	Multirow	0.899

For the simultaneous row aerodynamic optimization, the stage isentropic efficiency increased 0.53%. The successive row optimization yielded a modest 0.05% increase; however, when the optimized stator and rotor from the successive optimization were analyzed simultaneously with the SWIFT CFD code, the performance of the stage actually decreased by 0.86%.

The differences in results between the simultaneous row and successive row optimization methods are due to differences in the optimized stator blade shape as well as the flow velocity over the suction side of the blades of the two methods. Figure 2.9 shows the optimized stator and rotor blade geometries of the two optimization methods. As seen from the figure, the successive row optimization of the stator led to a much smaller leading edge radius than that of the optimized stator from the simultaneous row optimization. This smaller leading edge resulted in

an undesirable velocity distribution over the rotor in which the optimizer corrected for at the expense of a much smaller increase in stage isentropic efficiency than the simultaneous row optimization.

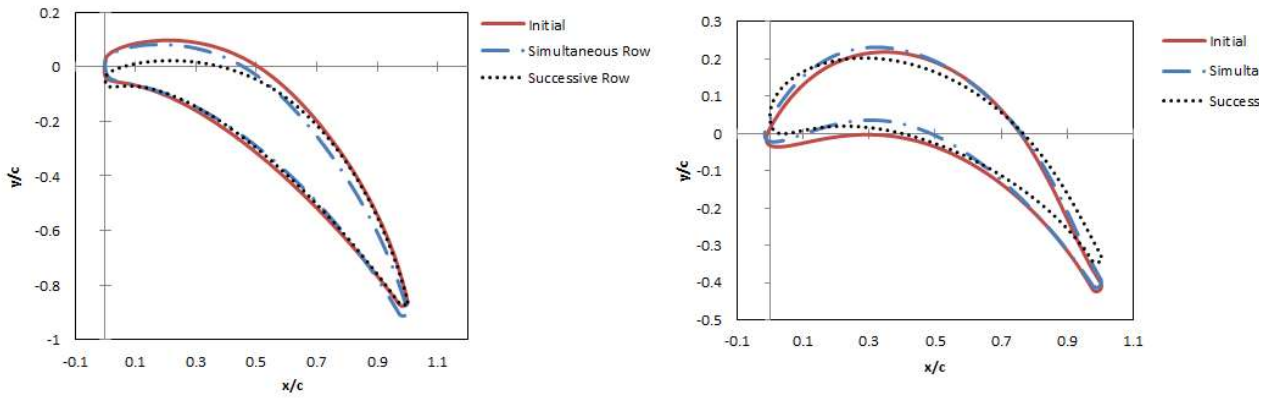

a) Stator **b) Rotor**

Figure 2.9. Blade geometries aerodynamic optimization

It is of particular interest to note that the CFD analysis of the stage using the exit properties of the stator as the inlet properties of the rotor as compared to the multi-row analysis not only yields different results regarding the spanwise pressure distribution as previously described, but also affects the velocity distribution over the blades. Figure 2.10 shows the isentropic Mach number distribution over the geometries of the optimized stator and rotor blades from the successive row optimization as well as compared to these same optimized geometries run in a multi-row flow analysis. The solid line depicts the individual blade row CFD analysis with the exit properties of the stator used as the inlet properties of the rotor and the dotted line depicts the stator and rotor of the successive optimization as run in the multi-row CFD analysis. From the figure it is evident that although the rotor blade optimized individually appeared to yield an acceptable flow distribution over the blade, when run with the optimized stator in the multi-row analysis, the flow yields an undesirable bump in the velocity distribution on the

suction side. This undesirable velocity distribution on the rotor blade may be a reason why the isentropic efficiency of the optimized individual stage blade rows actually decreased from the initial isentropic stage efficiency when run in the multi-row CFD analysis. This differential in results between the successive row and multi-row analysis is due to the characteristic boundary conditions applied at the blade row interface as described earlier. In addition, static pressure must be specified as an exit boundary condition. The user specified value for the stator as obtained from experimental data may differ from the value determined by the multi-row solver at the interface of the stator and rotor, resulting in different flow properties across the stage geometries for the two different methods. The multi-row solver negates the need for this specified static pressure at the blade row interfaces, allowing for a more accurate solution across the stage.

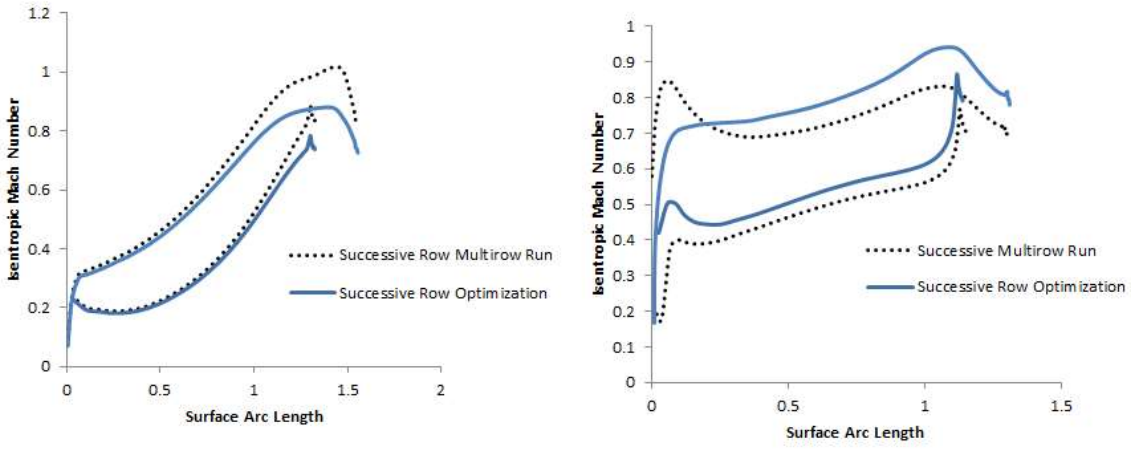

a) Stator **b) Rotor**

Figure 2.10. Velocity distribution of optimized successive row stage geometries run in a successive CFD analysis and multi-row CFD analysis

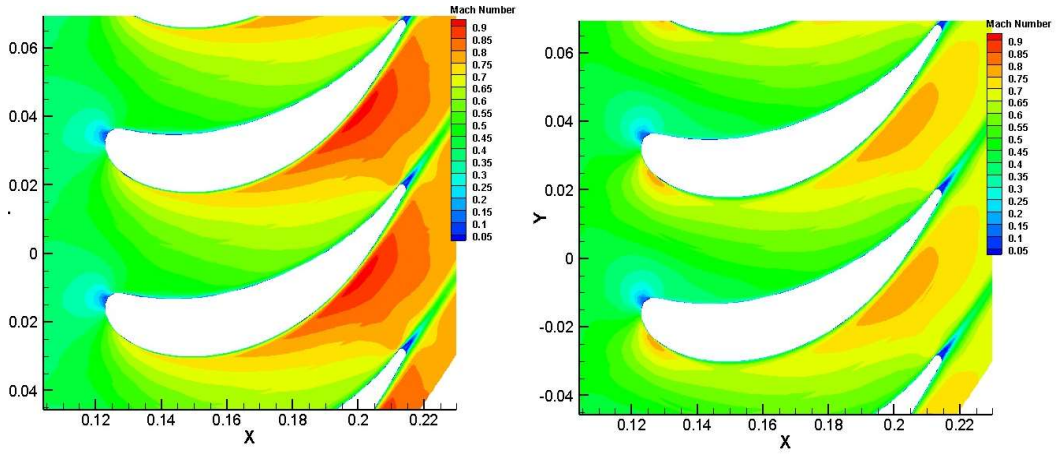

a) Successive row optimization **b) Successive row multi-row run**

Figure 2.11. Mach number contours of optimized successive row geometry

Figure 2.12 shows the comparison of the velocity blade distribution for the two optimizations. The throat location on the suction side is shown for reference. The successive row optimizations yield adequate results for the velocity distribution over the stator blade but not for the rotor blade. The negative gradient in the isentropic Mach number velocity distribution prior to the throat location may lead to negative performance results in the turbine stage and is not desirable.

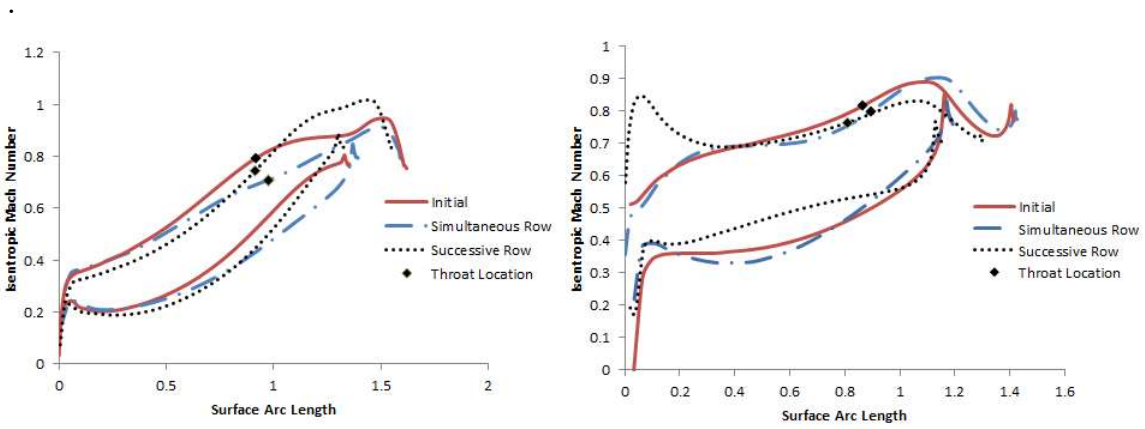

a) Stator **b) Rotor**

Figure 2.12. Velocity distributions for simultaneous and successive row optimizations

The rotor Mach number contours for the initial stage and the simultaneous row optimization are shown in Fig. 2.13. A monotonically increasing Mach number is maintained for the optimized geometry, with a slight increase in the maximum Mach number. Results indicate the simultaneous row optimization proved superior to the successive row optimization.

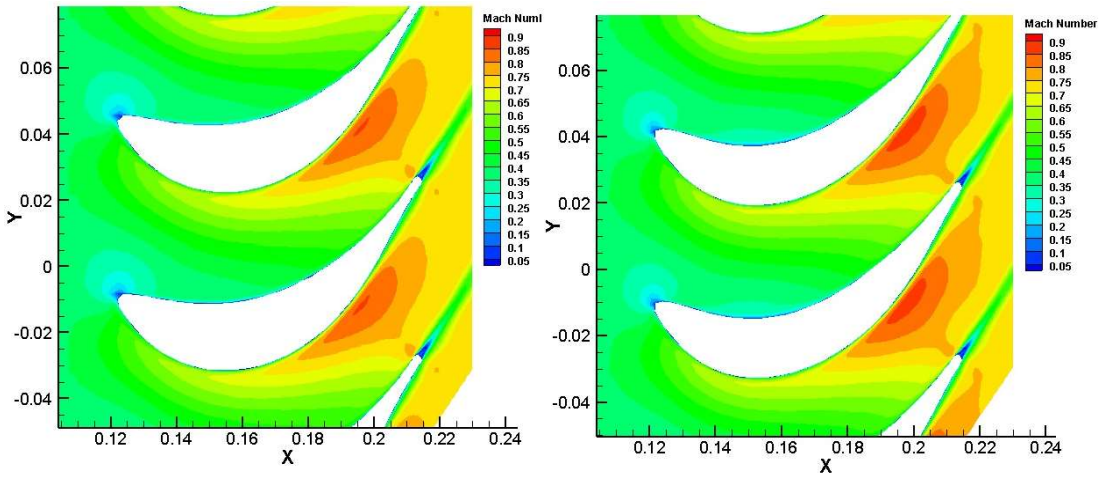

a) Initial simultaneous row **b) Optimized simultaneous row**

Figure 2.13. Rotor Mach number contours

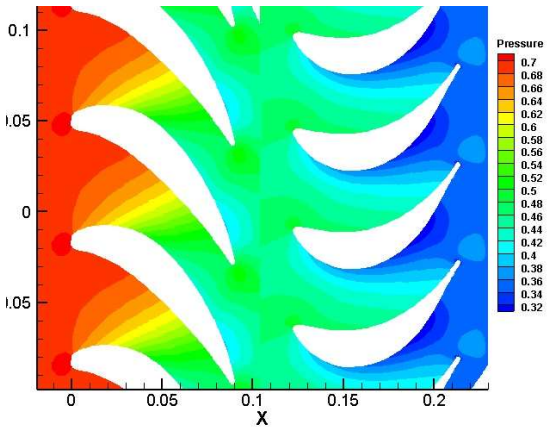

a) Initial

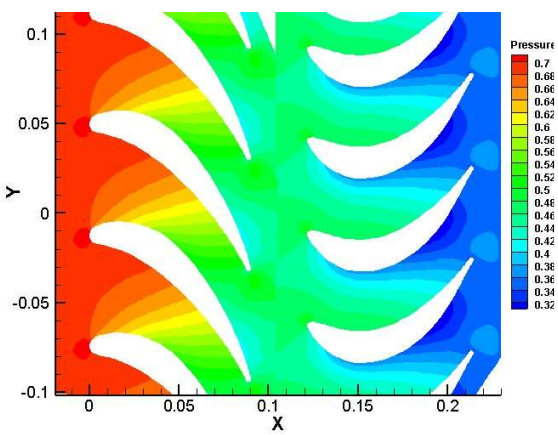

b) Simultaneous row

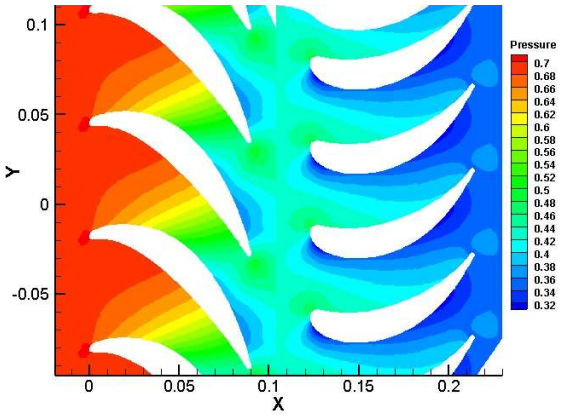

c) Successive row

Figure 2.14. Stage pressure contours

2.4.2 Aerothermal Optimization

The successive row optimization and multi-row optimization methods in the aerothermal optimization displayed trends similar to that of the aerodynamic optimization. The isentropic efficiency increased 0.45% for the simultaneous run while increasing the allowable total inlet temperature and thus the theoretical shaft work. The successive row optimization was successful in increasing the theoretical shaft work approximately 2.5 times that of the simultaneous row optimization, however, the stage isentropic efficiency decreased for both the successive row run

and the optimized multi-row analysis. It is evident that the solo optimization of the stator resulted in a higher allowable turbine inlet temperature than that of the stage optimization; however, the resulting stator shape had a negative effect on the stage isentropic efficiency, resulting in a lower value than the initial efficiency. The simultaneous row optimization served to increase the theoretical shaft work while also increasing efficiency which is more desirable than a decrease in stage efficiency at the expense of a higher shaft work output.

Table 2.3. Aerothermal Optimization Results

	Isentropic Efficiency				Work
Run	Initial		Optimized		increase
Simultaneous Row		0.907		0.911	2.60%
Successive Row	Successive	0.9138	Successive	0.906	6.80%
	Multirow	0.907	Multirow	0.887	4.90%

As seen from Fig. 2.15, the optimized stator and rotor geometries have a slightly larger leading edge radius than the initial geometries. These blunter leading edges serve to lessen the effects of heat transfer in this region. The resulting leading edge of the stator and rotor for the simultaneous row optimization closely mirrors that of the initial leading edges, an expected result as the initial stage was designed for a high temperature engine application. The successive row optimization resulted in blunter leading edges and thinner blades, especially for the stator. The resulting geometries of the stator and rotor for the successive row optimization result in a higher theoretical shaft work, but at the expense of a less efficient stage.

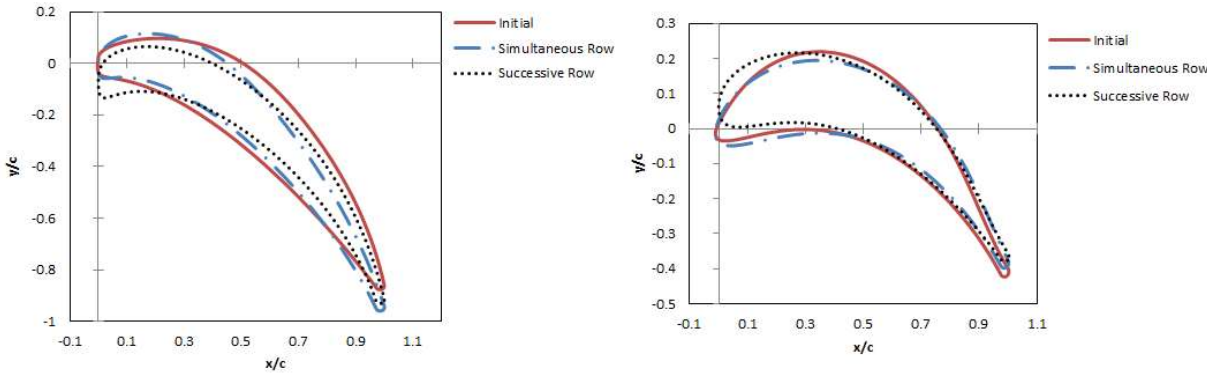

a) Stator **b) Rotor**

Figure 2.15. Blade geometries aerothermal optimization

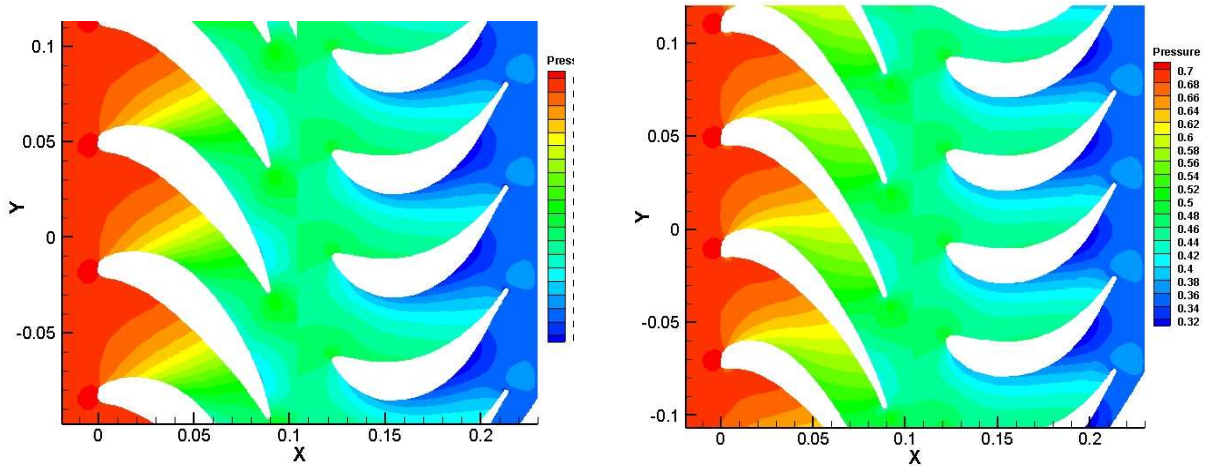

a) Initial **b) Optimized simultaneous row**

Figure 2.16. Stage pressure contours

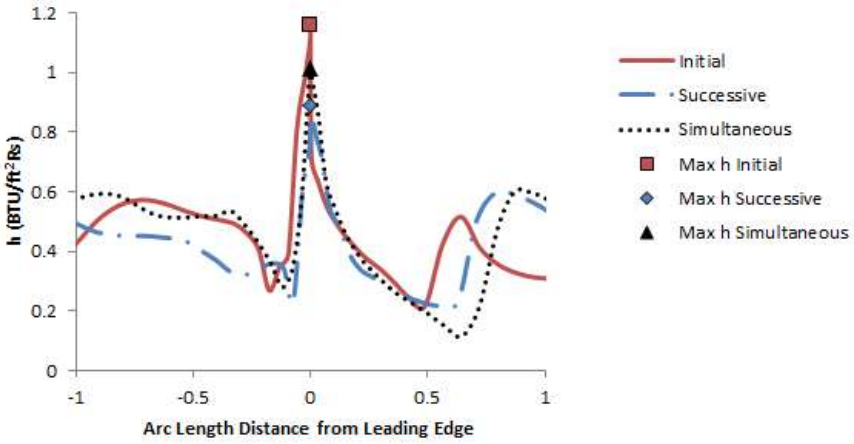

Figure 2.17. Heat transfer coefficient distribution across stator blade surface from pressure side to suction side

The heat transfer distribution along the surface of the blade for the resulting stator geometry from the two aerothermal optimization methods is compared to the initial distribution in Fig. 2.17. The successive optimization method lowers the maximum heat transfer coefficient by 23.5% from the original blade geometry at the leading edge. The simultaneous method lowers

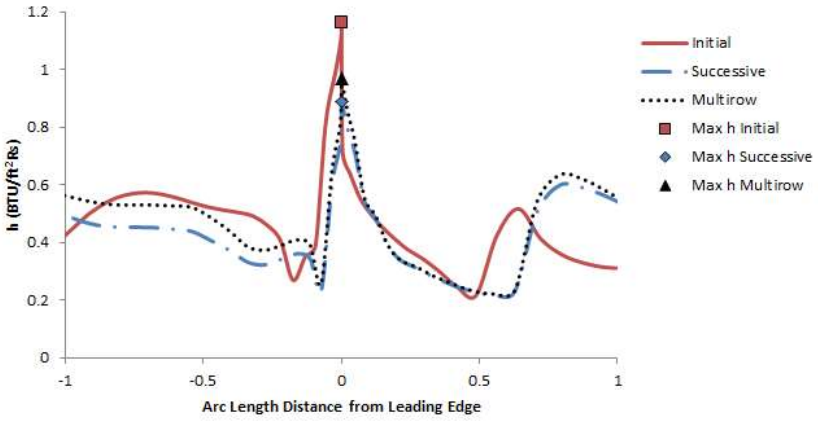

Figure 2.18. Heat transfer coefficient distribution for stator in successive row and multi-row stage analysis

the coefficient by 12.7%. The successive blade row optimization method also decreased the coefficient by a considerable margin on the pressure side as compared to the simultaneous optimization method. The heat transfer coefficient distribution of the optimized successive row

stator geometry run as an individual analysis and stage analysis is shown in Fig. 2.18. The individual analysis seems to overpredict the coefficient distribution on the pressure side, but is very similar to the multi-row stage analysis on the suction side. The maximum coefficient of the two methods differs by 8.5% with a lower heat transfer coefficient calculated by the individual stator analysis.

The velocity distribution over the stator and rotor blades for the optimized aerothermal geometries followed the same trend as the aerodynamic optimization results. The successive blade row optimization method appeared to provide adequate isentropic Mach number distributions over both the stator and rotor blades, however, when the blade geometries from the successive blade optimization where run in a multi-row analysis, an undesirable velocity gradient appeared in the rotor solution, just as in the aerodynamic optimization. Figure 2.19 shows the comparison of the velocity distribution over the blades for the two optimization methods. Again, the simultaneous optimization method provides a desirable monatomically increasing Mach number flow distribution over the rotor blade in contrast to the negative velocity gradient on the suction surface of the rotor blade for the successive row optimization geometry.

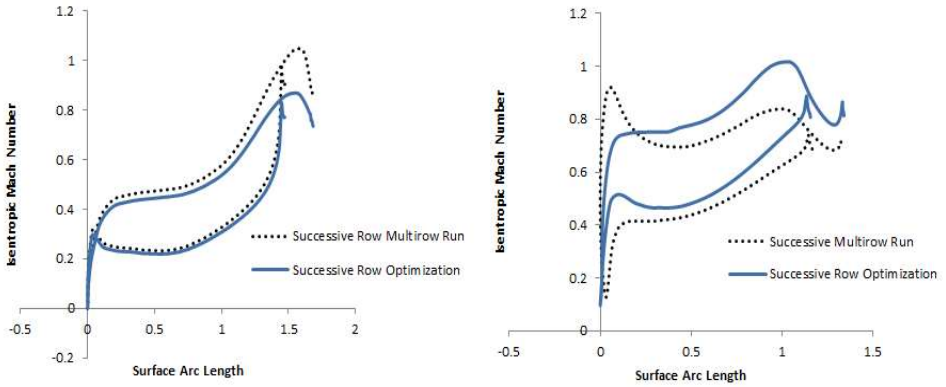

a) Stator **b) Rotor**

Figure 2.19. Velocity distribution of successive row stage optimization geometries run in a successive CFD analysis and multi-row analysis

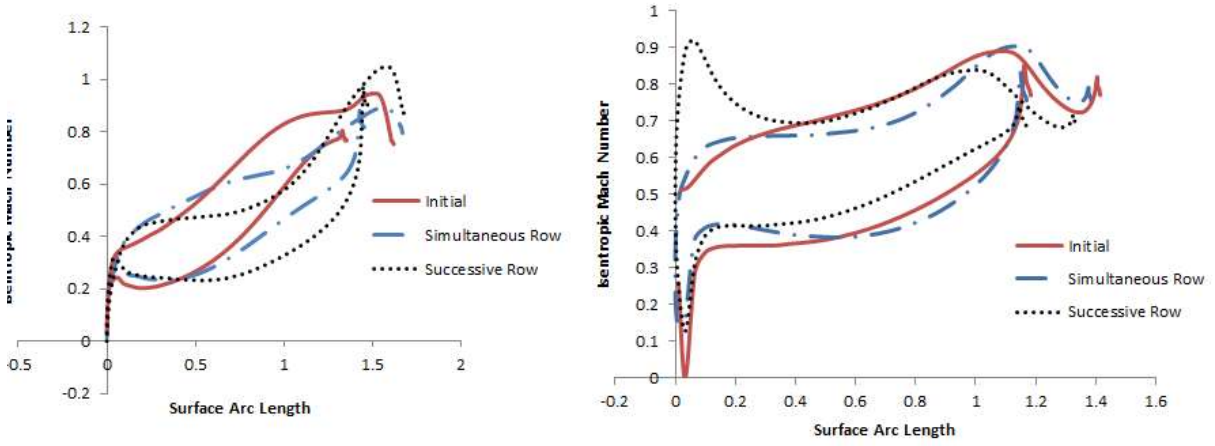

a) Stator **b) Rotor**

Figure 2.20. Velocity distributions for simultaneous and successive row optimizations

2.4.3 Comparative Analysis

The isentropic efficiencies of the optimized stage geometries for the two optimization methods presented are summarized in Table 2.4 for comparison purposes. The aerodynamic simultaneous row optimization increased the stage isentropic efficiency by 0.53% and the aerothermal simultaneous row optimization increased it by 0.45% while increasing the theoretical shaft work for a high temperature engine by 2.6%. The successive row optimization method for both the aerodynamic and aerothermal optimizations resulted in a decrease in the isentropic efficiency from the original stage. The successive row method was successful in increasing the theoretical shaft work more than that of the simultaneous row method.

Table 2.4. Results Aerodynamic and Aerothermal Optimizations

Optimization	Run	Initial Isentropic Efficiency	Optimized Isentropic Efficiency	Work Increase
Aerodynamic	Simultaneous Row	0.907	0.912	--
	Successive Row	0.907	0.899	--
Aerothermal	Simultaneous Row	0.907	0.911	2.60%
	Successive Row	0.907	0.887	4.90%

The optimized blade geometries for simultaneous optimization method are presented in Fig. 2.21 for the aerodynamic and aerothermal optimizations. Both optimizations closely resemble the original blade shape, with the aerothermal optimization more closely resembling the leading edge geometry of the initial blades which is expected due to the stage's initial design for a high temperature engine. The resulting geometries for the successive optimization method are presented in Fig. 2.22. The stator leading edge geometry for the aerodynamic optimization is much smaller than the original blade and aerothermal optimization. This could be a contributing factor for the reason why the stage isentropic efficiency decreased for the optimized geometry. In addition, the increase in camber of the stator for the aerothermal optimization geometry may also have been detrimental to the total stage efficiency. Both the aerodynamic and aerothermal optimizations yielded very similar rotor blade shapes with almost identical leading edges. These leading edges are much bigger than both the original blade shape and the simultaneous method optimized geometries. It is worth noting that the optimizations for the simultaneous blade runs more closely represent the original blade shape and produce the best results.

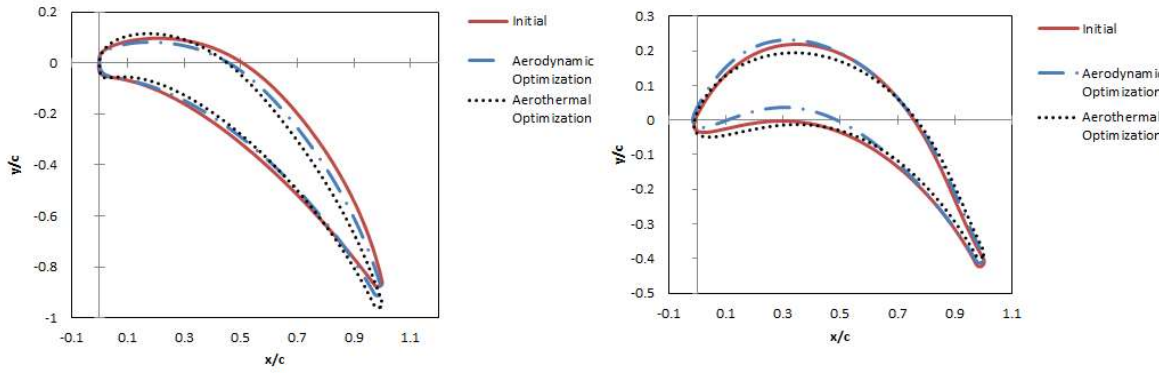

a) Stator **b) Rotor**

Figure 2.21. Optimized blade geometry comparison for simultaneous optimization method for aerodynamic and aerothermal optimizations

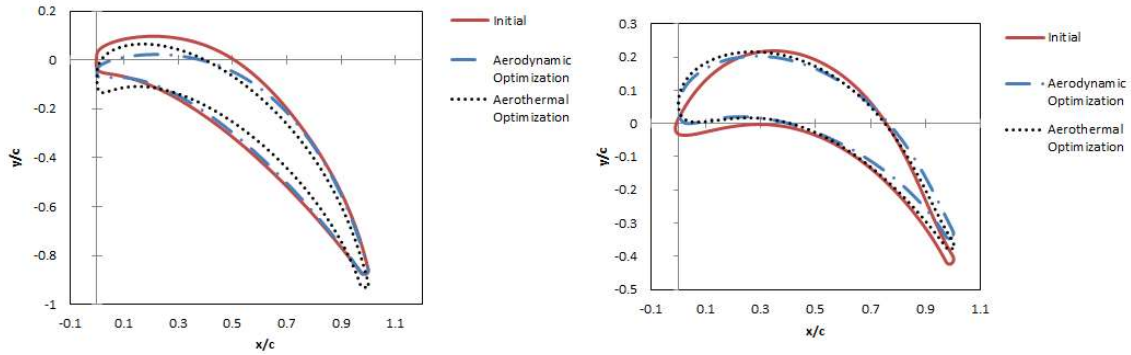

a) Stator **b) Rotor**

Figure 2.22. Optimized blade geometry comparison for successive optimization method for aerodynamic and aerothermal optimizations

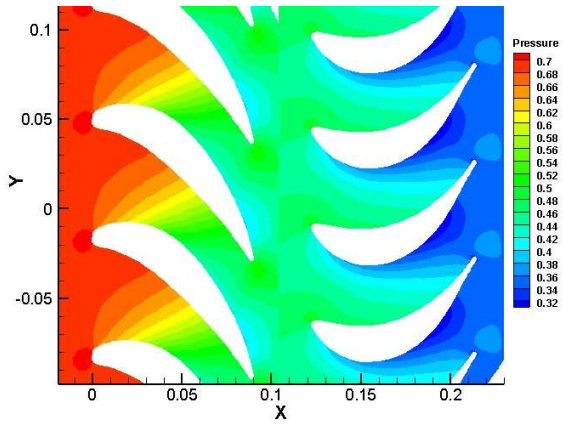

a) Initial

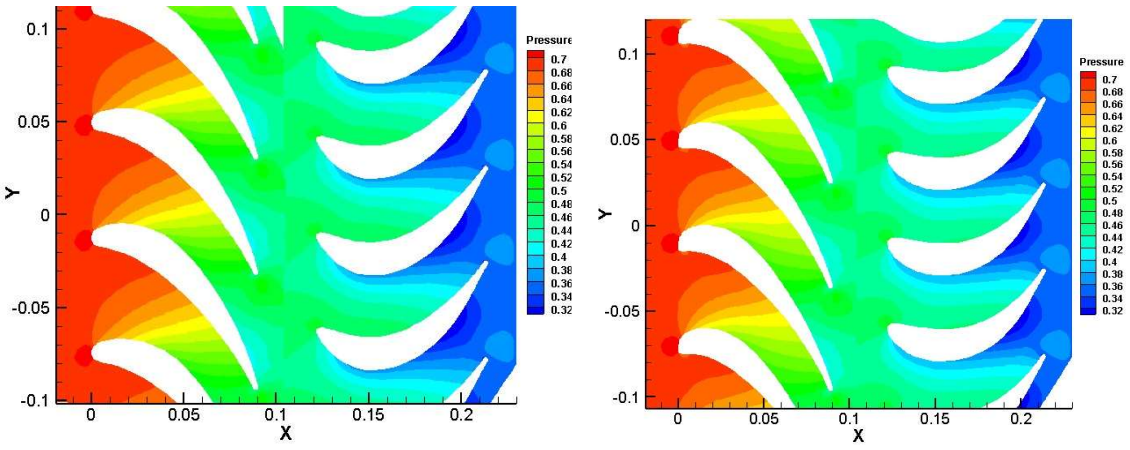

b) Aerodynamic **(c) Aerothermal**

Figure 2.23. Stage pressure contours

The heat transfer coefficient distribution over the stator blade surface for both optimization methods is shown in Fig. 2.24. The aerodynamic optimization decreased the maximum heat transfer coefficient by 4.8% although this was not an optimization objective. As expected, the maximum heat transfer coefficient for the aerothermal optimization decreased considerably, 12.7%, from the initial value while maintaining a similar distribution on the pressure side.

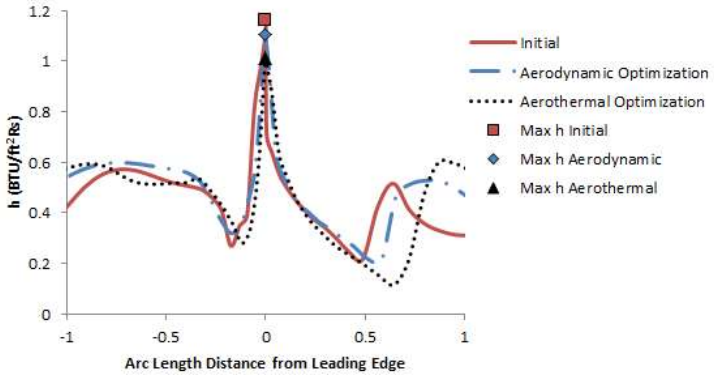

Figure 2.24. Heat transfer coefficient distribution on stator blade surface for simultaneous blade method

2.5 Multi-row Optimization Summary

In order to meet the demand for a high performing turbine engine, an optimization technique that produces reliable and optimal stage results within a reasonable time period is critical. An efficient evolution strategies genetic algorithm was paired with a Navier-Stokes CFD code to optimize a turbine stage utilizing a simultaneous and successive row optimization method. Results indicate that the optimizer was successful in finding an improved solution for the aerodynamic and aerothermal optimizations in a significantly reduced time frame than other optimizers utilizing Navier-Stokes flow solvers. In addition, the simultaneous optimization method proved superior to the successive row method.

Due to the nature of the Navier-Stokes equations, optimizations utilizing this type of flow solver often entail lengthy computation times. By utilizing a 64 processor computer cluster and an efficient evolution strategies optimizer, an optimized turbine stage solution utilizing the simultaneous row method was achieved within 26 hours for the aerothermal optimization and under 20 hours for the aerodynamic optimization. Repeat runs resulted in similar convergence times, within all three runs aerodynamic optimizations converging within three generations.

In addition, a comparison between a successive row optimization method and a simultaneous row optimization method was performed. The successive row optimization in which the stator was first optimized, followed by the rotor, resulted in poor results for both the aerodynamic and aerothermal optimization. By optimizing the stator geometry individually, interactions between the stator and rotor could not be accounted for, therefore resulted in a less than optimal stage performance. In addition, it was found that utilizing the average flow properties from the exit of the stator as the inlet properties to the rotor resulted in different flow properties across the stage geometries than that of a simultaneous row analysis. This is due to the characteristic boundary conditions applied at the stator-rotor interface of the multi-row solver in addition to differences in the specified static pressure at the exit of the stator as compared to the value found by the multi-row solver at the blade row interface. These differences resulted in a decrease in stage efficiency for both optimizations from the initial stage value.

The optimizer performed well utilizing the simultaneous stage optimization method, resulting in a 0.53% increase in stage isentropic efficiency for the aerodynamic optimization and a 0.45% increase for the aerothermal optimization. In addition, the aerothermal optimization yielded a 2.6% theoretical shaft work increase due to an increase in the maximum allowable total inlet temperature. Repeat runs verified the robustness of the optimizer, yielding efficiency results

within 0.1% of each other. The evolution strategies turbine stage optimizer paired with a Navier-Stokes flow code yielded good results in a relatively short computation time, and with 97% of computation time spent on the flow solver, this solver offers promise for an accurate and efficient three-dimensional turbine stage simultaneous optimization for thermal and aerodynamic applications.

Chapter 3

Three-Dimensional Turbine Stage Optimization

Although an airfoil optimization in the two-dimensional plane is simple and usually relatively quick, the optimal stage solution can never be achieved as three-dimensional affects such as boundary, secondary flow, and tip leakage are not accounted for in the blade geometry optimization. It is the goal of this work to arrive at an optimal three-dimensional stage solution in an acceptable time frame. In addition, care is taken to ensure the entire geometry is accounted for in the optimization routine, to include the airfoil cross section and as well lean, sweep, and twist stacking lines. Many works that claim a three-dimensional optimization solution fail to incorporate one or more of these features, thus not truly optimizing the blade or stage geometry. Structural and other undesirable flow characteristic constraints are accounted for in the stage optimization routine.

3.1 Geometry Definition

Due to the challenging nature of turbine blade shapes, accurate geometry definition of a turbine stage is vital to achieving an optimal design. In this work, the blade shape is submitted to the flow solver as a series of two-dimensional airfoils stacked from hub to tip, with the stacking line being the center of the trailing edge for the stator and the airfoil centroid for the rotor. The airfoils are defined as a set of coordinate pairs starting from the trailing edge of the pressure side and ending at the trailing edge of the suction side. To accurately define the blade geometry, a set of control points are used to define the complete three-dimensional turbine blade shape as shown in Fig. 3.1. The optimizer uses twelve control points to define two Bezier curves which make up

a turbine blade airfoil's upper and lower surface shown in Fig. 3.2. Bezier curves were chosen to represent the two-dimensional blade geometry due to its ability to represent almost any curve, ease of use, and small number of variables.

Location	Control Point	Upper Surface		Lower Surface		Sweep		Lean		Twist
		x	y	x	y	x	y	x	y	Degree
Midspan	1	0	0.0241	0	0.0241	0	0	0	0	-1
	2	0.0114	0.1293	-0.0184	-0.1459	0	0.5	0	0.5	0
	3	0.6198	0.2008	0.0337	0.0327	0	1	0	1	1
	4	0.4968	-0.1059	0.3145	-0.0497					
	5	0.8661	-0.2022	0.7067	-0.4748					
	6	1	-0.8585	0.97286	-0.8699					
Hub	1	0	-0.006	0	-0.006					
	2	-0.008	0.22258	0.00548	-0.1621					
	3	0.52264	0.29513	0.15489	-0.0278					
	4	0.62236	-0.0595	0.4312	-0.1688					
	5	0.83119	-0.2742	0.67083	-0.4173					
	6	1	-0.8828	0.97287	-0.8948					
Tip	1	0	-0.0361	0	-0.0361					
	2	-0.0774	0.12053	0.04458	-0.1263					
	3	0.43327	0.37915	0.20609	-0.1562					
	4	0.73746	-0.0361	0.42877	-0.0468					
	5	0.73413	-0.3376	0.74502	-0.5662					
	6	1	-0.8251	0.97532	-0.8419					

Figure 3.1. Sample blade control points for geometry definition

Bezier curves were chosen to represent the two-dimensional blade geometry due to their ability to represent almost any curve, ease of use, and small number of variables. The two-dimensional blade profile is defined at the hub, midspan, and tip, for a total of 36 control points. To represent the complete three-dimensional blade shape, the use of non-uniform rational basis spline or NURBS curves was chosen. NURBS curves are widely used in geometric representations and are used to accurately represent any curve or surface. A quadratic rational Bezier curve (QRBC) was chosen to represent the stacking line of lean and sweep to capture three-dimensional deformations. A QRBC is a second degree NURBS curve with three control points. It represents exactly any conic line such as a circle, parabola, ellipse or hyperbola, and is expressed parametrically in terms of $u \in [0,1]$ as:

$$\vec{C}(u) = \frac{(1-u)^2 w_0 \vec{P}_0 + 2u(1-u)\vec{P}_1 + u^2 w_2 \vec{P}_2}{(1-u)^2 w_0 + 2u(1-u)w_1 + u^2 w_2} \tag{3.1}$$

where P is a coordinate, w is a weight and C(u) gives the coordinates on any point on the curve in terms of u. Since weights of control point play a less important role than the control points themselves, the weights are set equal to one and Eq. (1) reduces to:

$$\vec{C}(u) = (1-u)^2 \vec{P}_0 + 2u(1-u)\vec{P}_1 + u^2 \vec{P}_2 \tag{3.2}$$

This second order curve was selected over a higher order curve with more control points as the smooth nature of the curve prevents inflection points, thus ensuring all resulting curves are feasible and negating the need for a feasibility check of this nature in the optimizer. As most turbine blades feature a fairly linear twist from hub to tip, the twist of the blade was simply represented as a line with twist linearly interpolated from a defined angle of twist at the hub and tip.

To ensure a well-defined blade geometry, airfoil profiles between the hub and midsection and between the midsection and tip are interpolated to form a total of 19 airfoils stacked from hub to tip. A NURBS skinning technique[34] is applied to apply a stacking line to account for the lean, sweep, and twist of the blade. Translation is applied to the airfoils to account for the lean and sweep along the stacking line in the circumferential and axial directions respectively, and rotation is applied to account for the twist along the blade height. Rotation is applied through a simple rotation matrix, Eq. (3.3), in 2-D Euclidian space which rotates points counter-clockwise through an angle θ.

$$R = \begin{pmatrix} \cos\theta & -\sin\theta \\ \sin\theta & \cos\theta \end{pmatrix} \tag{3.3}$$

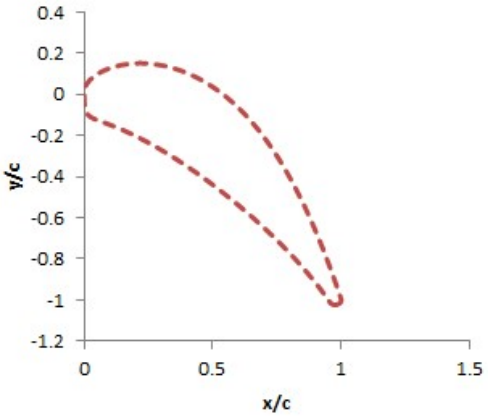

(a) Two-dimensional airfoil represented by Bezier curves

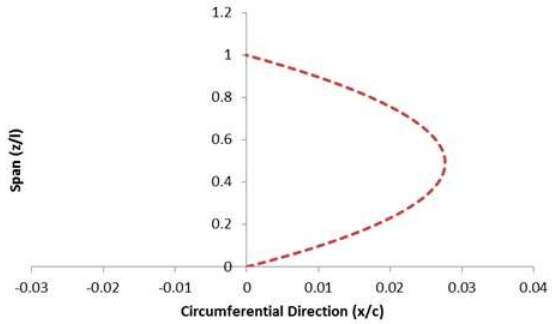

b) Lean represented by NURBS curve

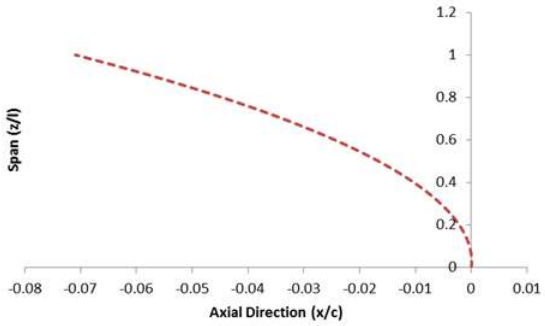

(c) Sweep represented by NURBS curve

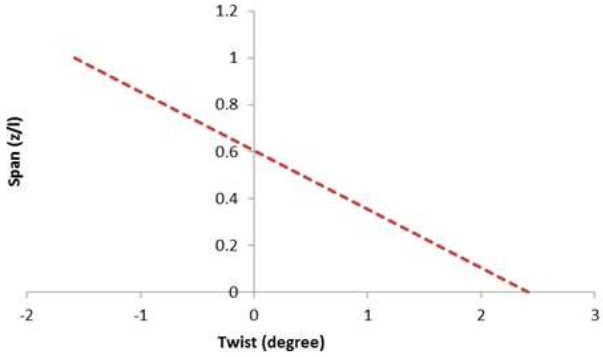

(d) Twist represented by two-dimensional line

Figure 3.2. Turbine blade profile represented by Bezier and NURBS curves

The points are rotated about the center of the trailing edge circle for the stator and the airfoil centroid for the rotor. The Cartesian coordinates are then converted to cylindrical coordinates and sent to the flow solver for grid generation and CFD analysis. Three-dimensional modeling adds an additional 14 design variables to the optimization. The complete geometric blade parameterization is shown in Fig. 3.3.

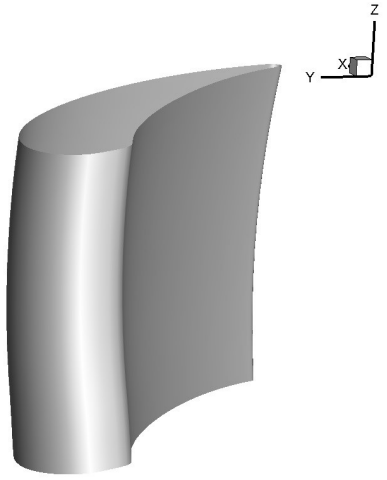

Figure 3.3. Blade geometry

The flow solver used is identical to the one used in the two-dimensional optimization. Grids were generated for each blade row separately using the TCGRID turbomachinery grid code.[35] An inlet H-grid upstream of the stator is generated using transfinite interpolation in addition to C-type blade-to-blade grids at 19 spanwise locations using an elliptic grid generator. O-grids were generated algebraically in the tip clearance region over the rotors. Individual grids were then combined such that each grid overlapped its neighbor by one cell. Grid size is 301,644 for the stator and 385,434 for the rotor.

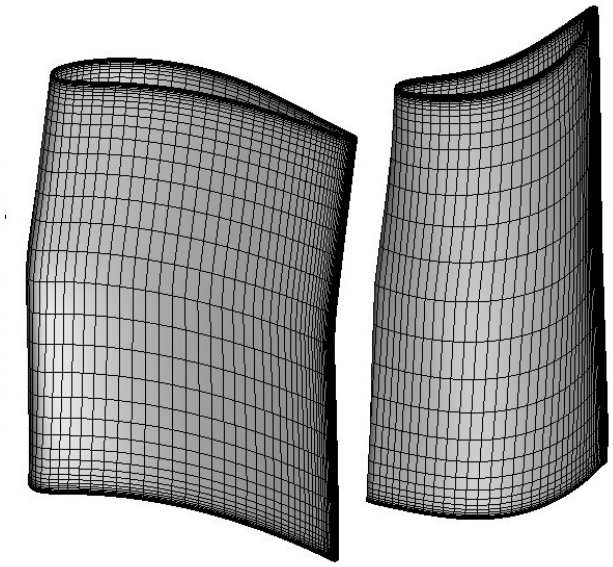

Figure 3.4. Grid for NASA stage

3.2 Algorithm Definition

The Evolution Strategies algorithm used in the two-dimensional optimization was initially applied to the three-dimensional stage problem. After a few initial trials, it was apparent that the optimizer was not working as well for the 3-D optimization. Due to the exponential increase in the number of design variable when going from a 2-D optimization to a 3-D one, it was apparent that only eight offspring was not enough to fully investigate the search space within a reasonable timeframe.

Due to the success and popularity of genetic algorithms used for three-dimensional turbine blade optimization problems with many design variables, a hybrid real coded adaptive range algorithm and evolution strategy algorithm was adopted for the three-dimensional stage optimization. The variables for the evolutionary algorithm were chosen to be real coded rather than binary coded as the design variables are real parameters. The algorithm is shown in Fig. 3.5.

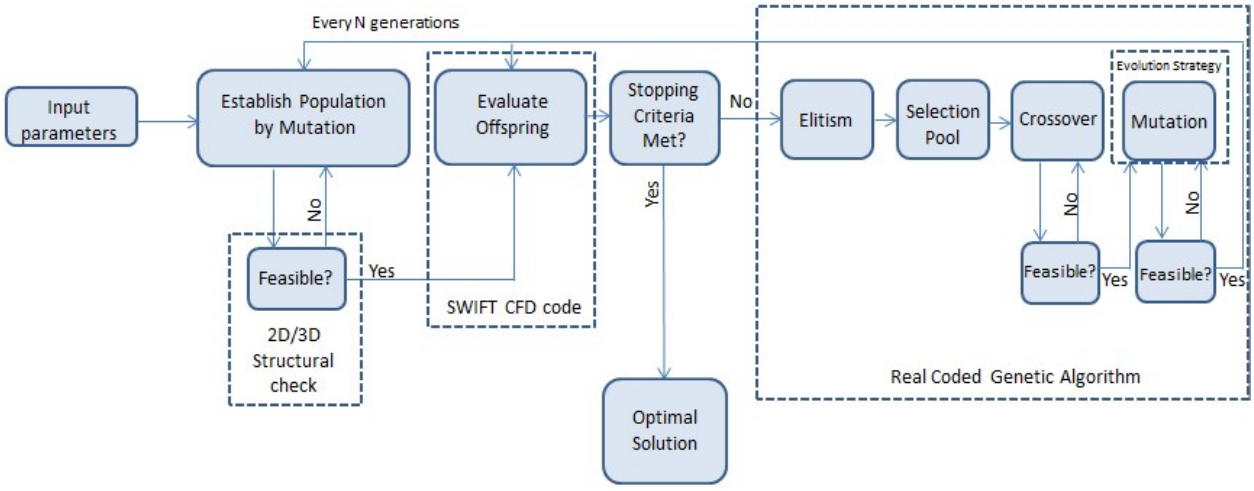

Figure 3.5. **Evolutionary algorithm flow chart**

Selection, elitism, crossover, and mutation make up the core of the optimization algorithm. First a population size is selected and an initial parent turbine blade or turbine stage geometry is mutated 100% to establish an initial selection pool. The mutated offspring are evaluated through a flow solver and assigned an objective function value. To establish the next generation of off spring, the best few performers from the pool are selected to identically pass down to the next generation, ensuring that the most fit chromosomes survive. This process is known as elitism[36] and is typically applied to the best two offspring in this work. Next a selection pool is created from which the remaining next generation offspring will be produced. A tournament selection or roulette wheel method is generally used. For this work a roulette wheel method[37] is employed in which an individual is assigned a portion of the wheel in proportion to its fitness level. Individuals are then selected at random to comprise of the selection pool, and it is through this way that the fitter individuals have a better chance of being selected. After the selection pool is chosen, the next generation of offspring are generated through crossover and mutation. Crossover utilizes the idea that the best characteristics from both parents can be combined to create a child offspring more fit than either parent. A blended crossover (BLX-

0.5)[38] is used for recombination in which two children are formed from two parent offspring. For a given gene i and $\text{parent1}_i < \text{parent2}_i$, the two children offspring are formed from Eq. (3.4).

$$child = rand((parent1 - 0.5(parent2 - parent1), (parent2 + 0.5(parent2 - parent1) \quad (3.4)$$

A random mutation is applied to the best individual in the previous generation to complete the next generation offspring pool. The mutation rate for this work is 20%. The evolution strategies one-fifth rule[39] is applied to one-half of the mutation population. A modified adapative range technique[40] is implemented every 25 generations in which the next generation population is generated from 100% mutation of the previous generation's best offspring. Population size is 60 and 100 generations were run.

3.3 Computation Requirements

When using a computational fluid dynamics flow solver in a turbine blade optimization, the main area of concern is the required computational effort. To achieve an optimal solution in a reasonable timeframe, parallel computer processing is essential, and is becoming increasingly available, accessible, and affordable. An evolutionary algorithm is well suited for use with parallel processing as each of the offspring in a generation may be evaluated by the flow solver at the same time. As over 99% of the optimization time is spent on the flow solver when running the optimization on a single processor, the use of a computer cluster is vital in reducing computation time. The Virtual Symmetric Multiprocessing High Performance Computing Cluster (HPCC) at Auburn University is used for this work. This cluster composes of 512 processors, allowing for all offspring to be evaluated by the flow solver simultaneously, thus reducing computation time by over 98% from that of a single processor. Grid generation and the optimization routine are performed in serial whereas the evaluation of the offspring by the flow

solver is performed in parallel. Using parallel processing, the flow solver comprises of 71% of total computation time and grid generation comprises of 27% for a stage optimization.

3.4 Design Optimization Problem

Three validation cases were run for this work. The first validation case was a well-known annular stator vane[41] comprised of 36 blades of constant profile from hub to tip with no lean, twist, or sweep. It was chosen as it had been used in a SWIFT validation case[42,43] and its shape allowed for a simple optimization for lean, sweep, and twist in the spanwise direction and for a single airfoil shape in the blade-to-blade direction. A total of 27 variables were optimized for this case. The second validation case was the rotor of the uncooled NASA axial turbine stage used in the two-dimensional stage optimization. Lean, sweep, and twist were optimized as well as the two-dimensional airfoil sections at the hub, midsection, and tip. A total of 71 variables were optimized for case II. The uncooled NASA axial turbine that was optimized two-dimensionally in the previous section was chosen for the three-dimensional stage optimization for validation case III. This work was selected as it offers well documented experimental one stage and two stage gas turbine data. Lean, sweep, and twist as well as the hub, midsection, and tip airfoil sections of both the stator and rotor were optimized simultaneously, yielding 65 design variables for the stator, and 71 for the rotor for a total of 136 design variables for the stage optimization.

The aerodynamic objective function used for the individual stator and rotor optimizations was the total pressure loss across the stator and the total to total efficiency across the rotor. The stage isentropic efficiency was again used as the objective function for the stage optimization. For each case, the mass flow rate was constrained to not less than the original rate and the same penalty functions of the monatomically increasing Mach number and uncovered turning angle were applied.

3.5 Structural Considerations

The same two-dimensional structural considerations were implemented as in the two-dimensional optimization. An additional structural analysis was implemented to account for the three-dimensional effect of the centrifugal forces on the rotor blades. The centrifugal forces are approximately 100 times greater than the pressure forces in this research, thus the centrifugal forces are the only three-dimensional forces considered in the structural analysis. Due to the nature of the optimization routine, the stacking line of the airfoil sections is not radial, resulting in centrifugal forces generating a moment around the center of gravity of the hub profile. This results in a bending and tensile stress at the hub of the rotor blade. The centrifugal force generated from along the rotor blade is calculated from Eq. (3.5)

$$F_c = \int_{r_h}^{r_t} \rho \omega^2 A r dr \tag{3.5}$$

The mass and radius from the hub of each of the 19 airfoil sections can be calculated, simplifying Eq. (3.5) to Eq. (3.6):

$$\vec{F_c} = \sum_{i}^{n} F_i \hat{e_i} = \sum_{i}^{n} m_i r_i \omega^2 \hat{e_i} \tag{3.6}$$

where n is the number of airfoil sections. The moment of each force around the center of gravity of the hub is then calculated:

$$\vec{M} = \sum_{i}^{n} \vec{l}_i x \vec{F_i} \tag{3.7}$$

From Eq. (3.7), the moments in the x, y, and z directions can be calculated. It is observed that the moment that generates torsion in the z-direction is two orders of magnitude less than that in the

x- and y-directions, and thus can be neglected in the stress calculation. The axial and tangential moment components are then used to calculate the bending stress at the hub:

$$\sigma_{bending} = -\frac{M_y I_x + M_x I_{xy}}{I_x I_y - I_{xy}^2} x + \frac{M_x I_y + M_y I_{xy}}{I_x I_y - I_{xy}^2} y \tag{3.8}$$

Finally, the total stress at the rotor hub is found by combining the bending stress and tensile stress:

$$\sigma_{hub} = -\sigma_{bending} + \frac{F_s}{A_h} \tag{3.9}$$

According to preliminary studies, the maximum stress on the two-dimensional blade profile occurs near the location of maximum thickness on the suction side and near the trailing edge. Points were selected at these locations for a rudimentary analysis to determine maximum stress for the rotor blade. Preliminary studies indicate all solution candidates experience a maximum stress far below that of the yield stress of nickel-based steel alloy, which is 1035 MPa. With maximum stress occurring at the root of the blade, all possible solution candidates are well within the structural bending stress requirement. While not intending to constitute a thorough structural analysis, this simple check was completed as part of the feasibility routine shown in the optimizer flow chart, and ensured a feasible solution.

3.6 Results

3.6.1 Case I

The annular stator was optimized for lean, sweep, and twist in the spanwise direction and for a single two-dimensional profile shape in the blade-to-blade direction. The blade geometry

generated by the optimizer agreed well with experimental and reference data as shown in Fig. 3.6. An optimized solution was reached in 18.4 hours and increased the total pressure ratio across the blade 0.3%, from 0.9773 to 0.9803. The total pressure loss in the spanwise direction is shown in Fig. 3.6. The optimized solution decreased total pressure loss from the hub up to 80% span. Stacking line and two-dimensional airfoil shape for the initial and optimized solutions are shown in Fig. 3.7. The optimized solution yielded a bowed shape lean, with a maximum lean of 2.8% at the midspan. In addition, the optimized solution also yielded a maximum sweep angle of -7.1% at the tip of the blade and a blade twist of 2.4° at the hub and -1.6° at the tip. The three-dimensional blade shape comparison of the initial and optimized solution is shown in Fig. 3.8. Pressure and Mach number contours at the blade midspan are shown in Figs. 3.9 and 3.10. The annular stator row was optimized under the constraint of a positive suction surface velocity gradient before the throat location at the blade midspan and is shown in Fig. 3.11.

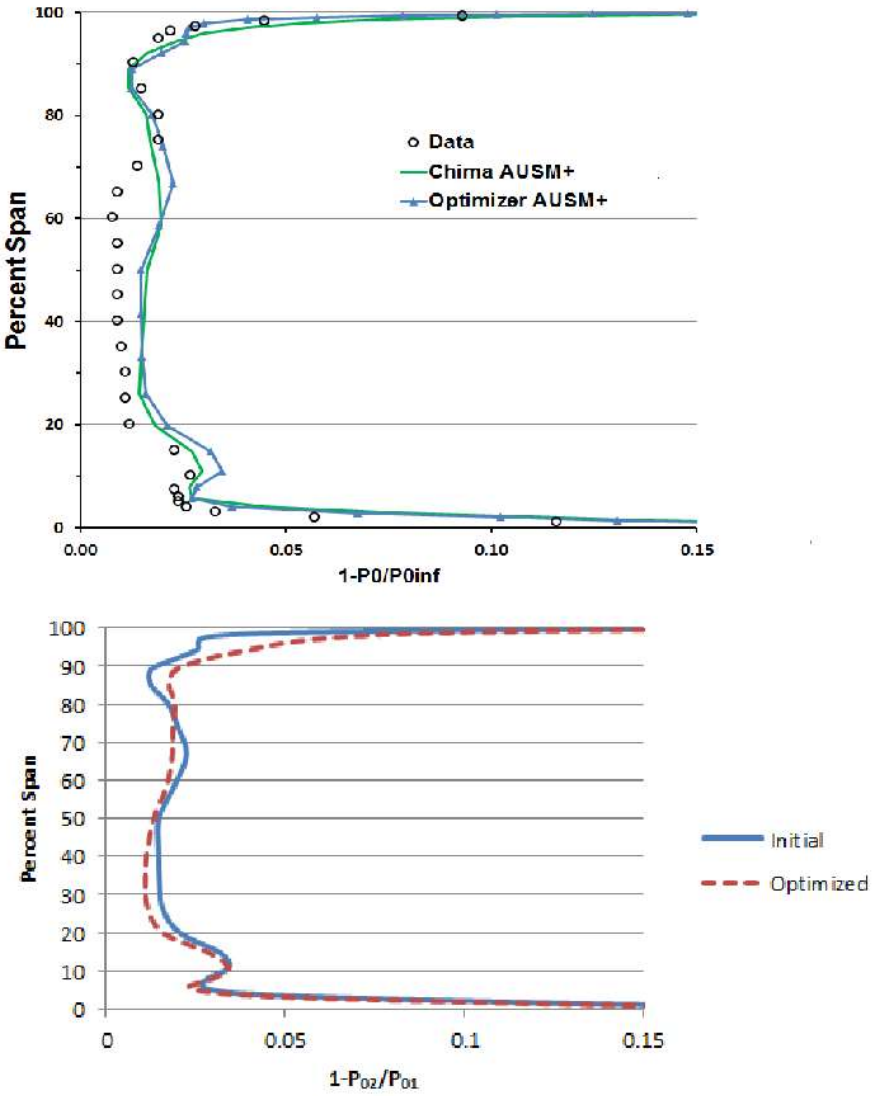

Figure 3.6. Spanwise distribution of stator total pressure, initial validation (top) and optimized solution (bottom)

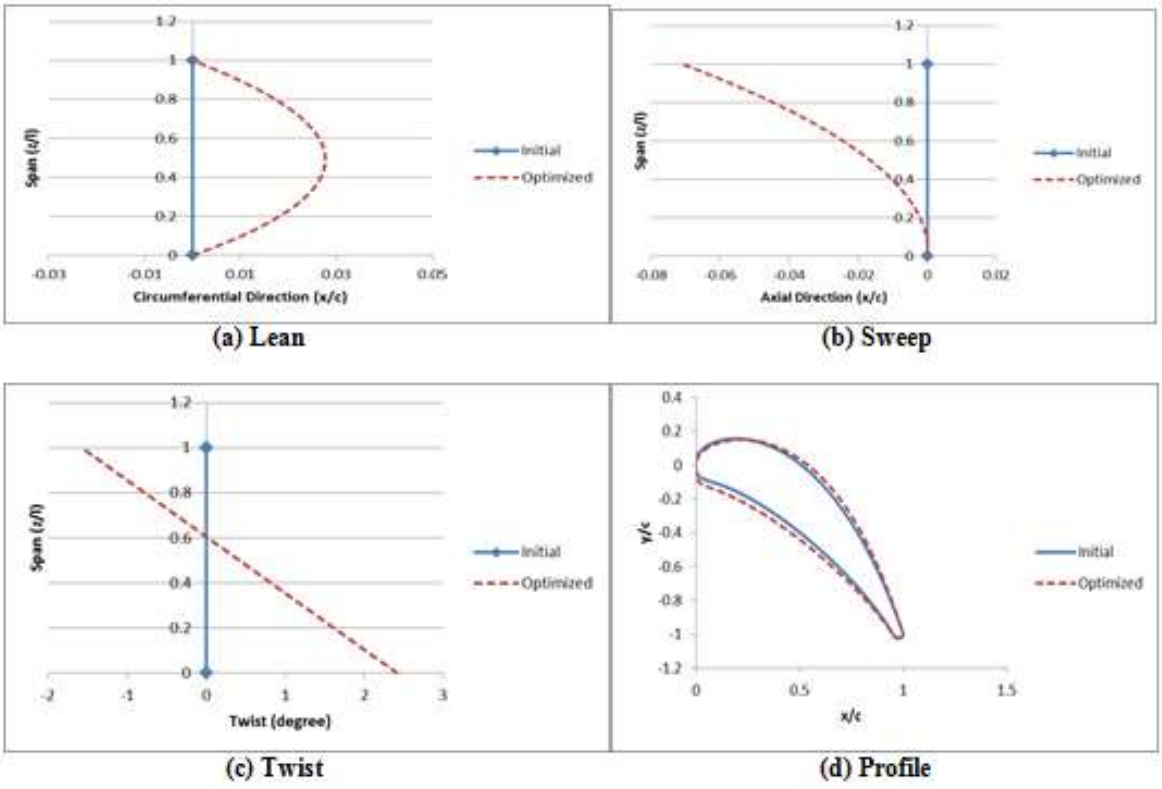

Figure 3.7. Stacking line profiles (a-c) and two-dimensional airfoil profile (d)

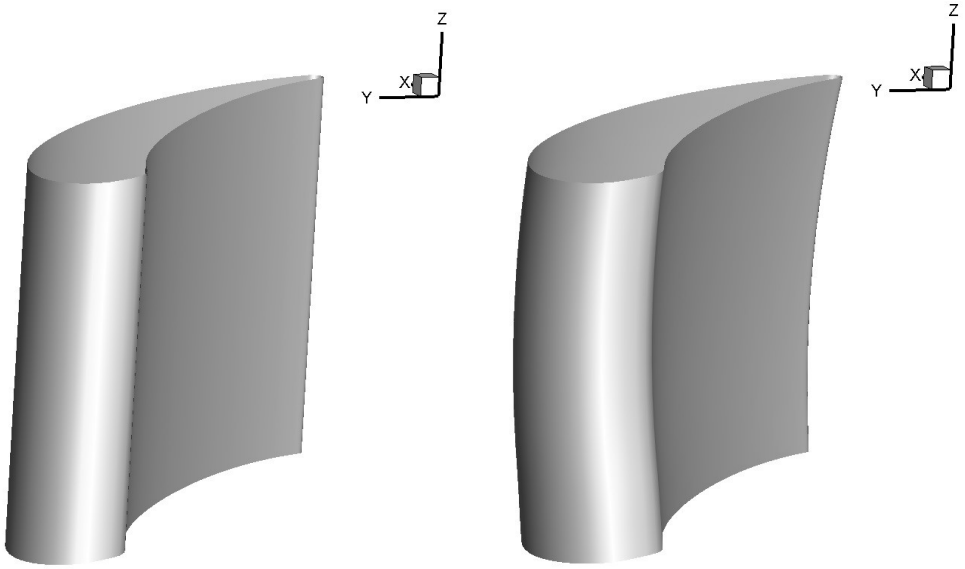

(a) Initial **(b) Optimized**

Figure 3.8. Blade shape comparison

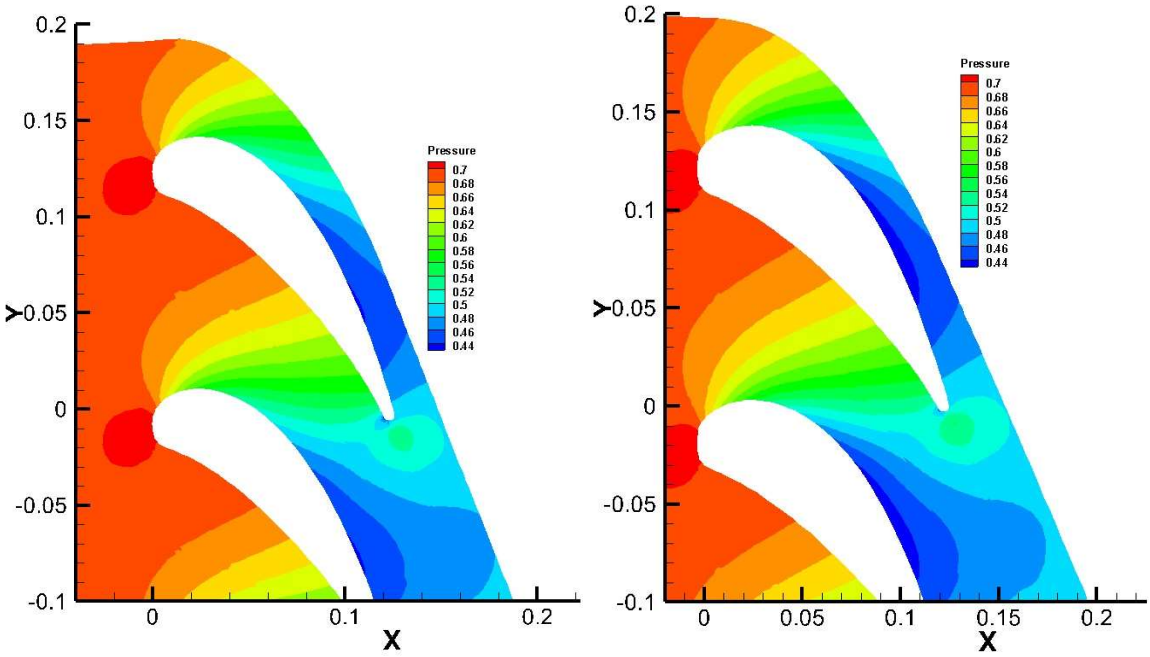

(a) Initial **(b) Optimized**

Figure 3.9. Pressure contours at midspan

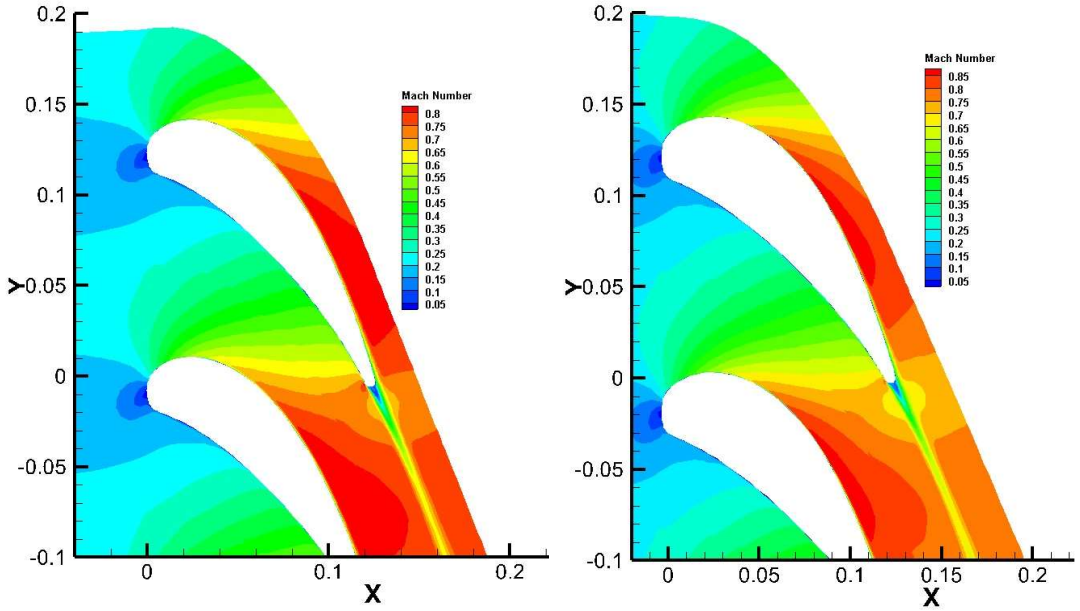

(a) Initial **(b) Optimized**

Figure 3.10. Mach number contours at midspan

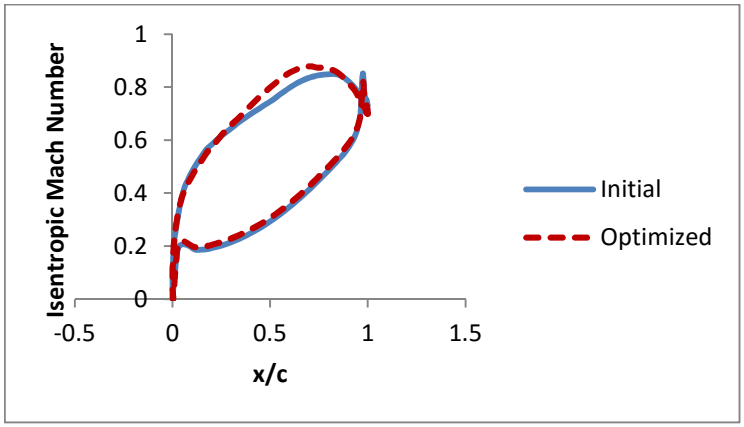

Figure 3.11. Velocity distibution on blade surface

3.6.2 Case II

The second validation case performed was the individual annular rotor from the uncooled NASA stage. The rotor comprised of 61 blades and was optimized for lean, sweep, and twist in

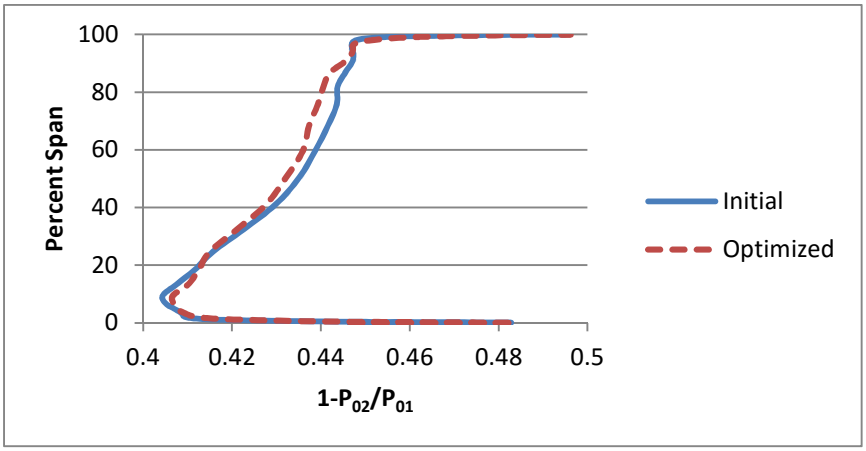

Figure 3.12. Pressure loss along rotor span

the spanwise direction as well as for the two-dimensional airfoil profiles in the blade-to-blade direction at the hub, midspan, and tip. An optimized solution was achieved in 19.8 hours and resulted in a 0.71% increase in isentropic efficiency from its initial value of 0.9265 to its optimized value of 0.9336. The pressure loss along the span of the blade is shown in Fig. 3.12. The optimized solution decreased total pressure loss along most of the blade span with the

exception of the hub area. For both the initial and optimized solution, the total pressure loss increases steadily from hub to tip. This is due to the constant spanwise inlet properties to the rotor as the rotor is being optimized individually and not with the stator. A stage optimization

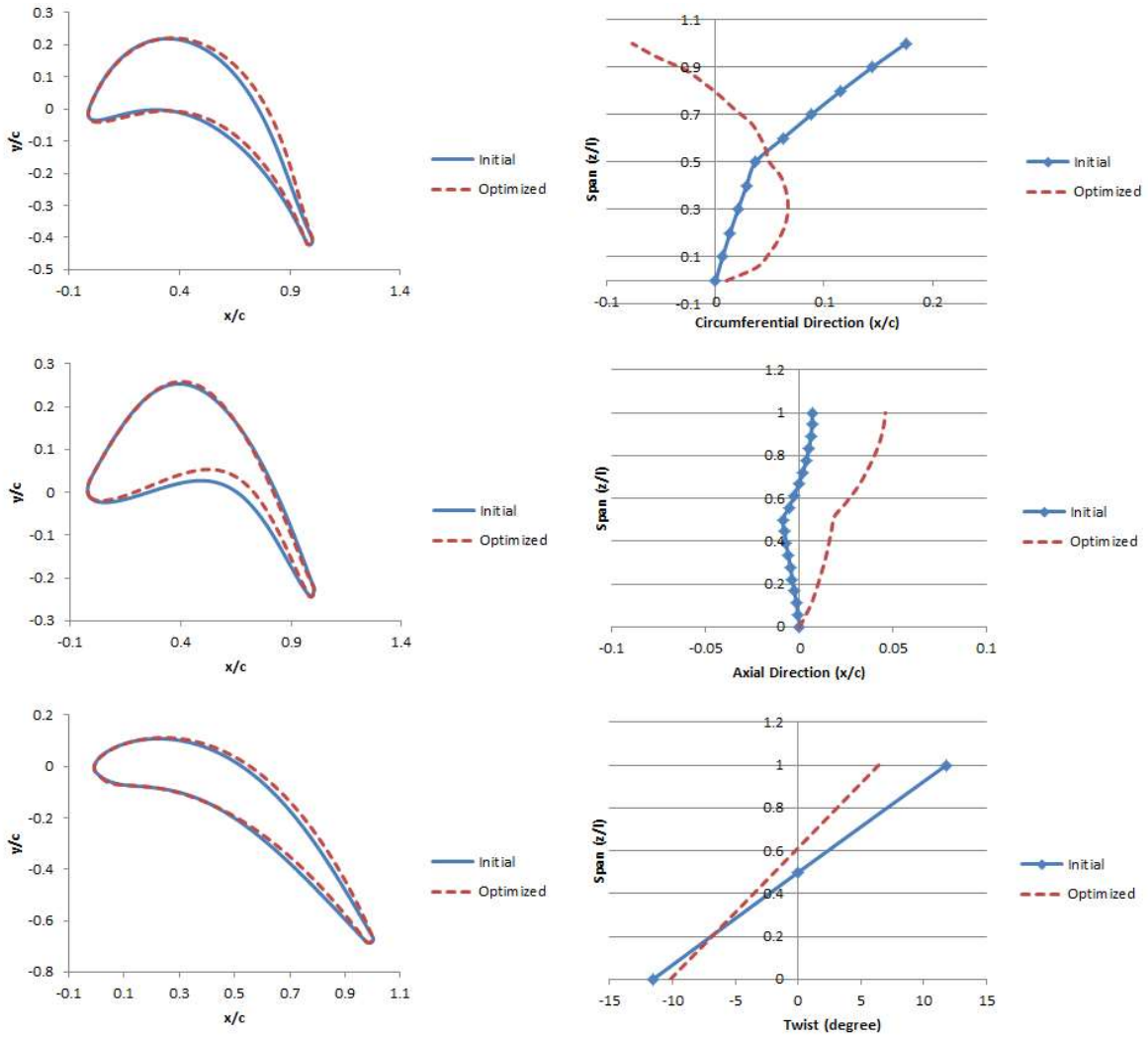

Figure 3.13. Two-dimensional profile sections (left) midspan, hub, tip (top to bottom). Stacking line spanwise direction (right)

results in a more even pressure loss distribution as expected and are presented in Case III.

The stacking line in the spanwise direction and the two-dimensional airfoil sections at the hub, midspan, and tip are shown in Fig. 3.13. Again, the optimized lean, sweep, and twist

solutions vary widely from the initial stacking lines as input spanwise properties are constant and do not vary as they would in a stage with the spanwise exit flow properties of the stator equaling the spanwise inlet flow properties of the rotor.

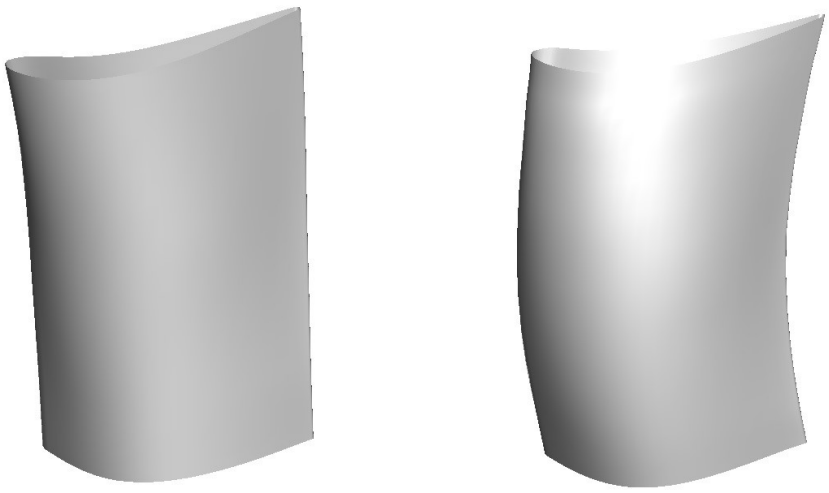

(a) Initial **(b) Optimized**

Figure 3.14. Blade shape comparison

Pressure and Mach number contours are shown at the hub, midspan, and tip profiles in Figs. 3.15 and 3.16 respectively. The optimized solution was constrained to a positive suction surface velocity gradient before the throat location and proved to be a very limiting constraint on the solution space as just a slight change in the initial blade shape had the tendency to result in a negative suction surface velocity gradient. The isentropic Mach number along the chord length is shown in Fig. 3.17.

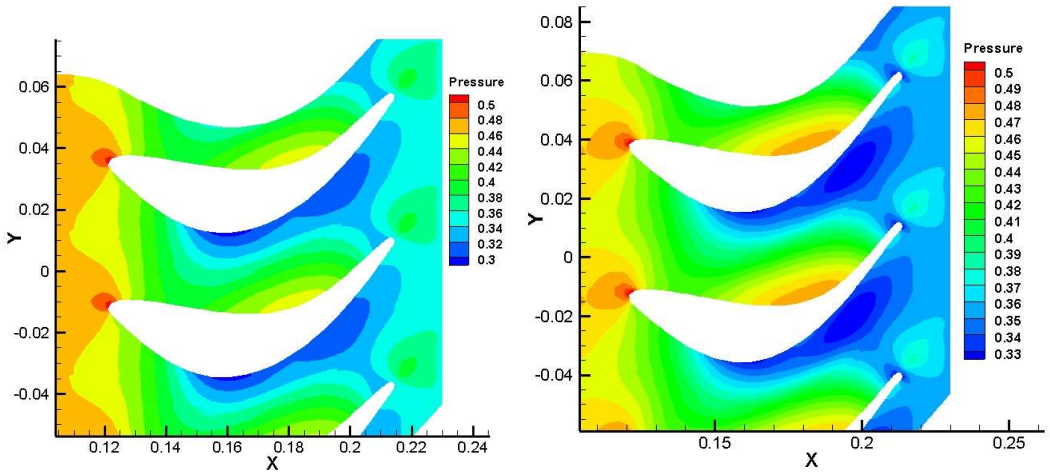

(a) Initial hub **(b) Optimized hub**

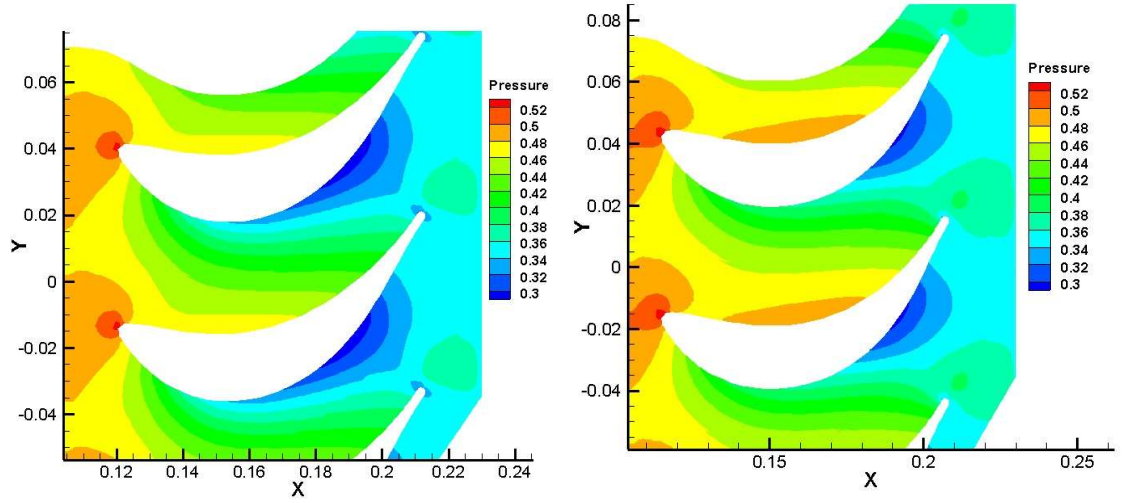

(c) Initial midspan **(d) Optimized midspan**

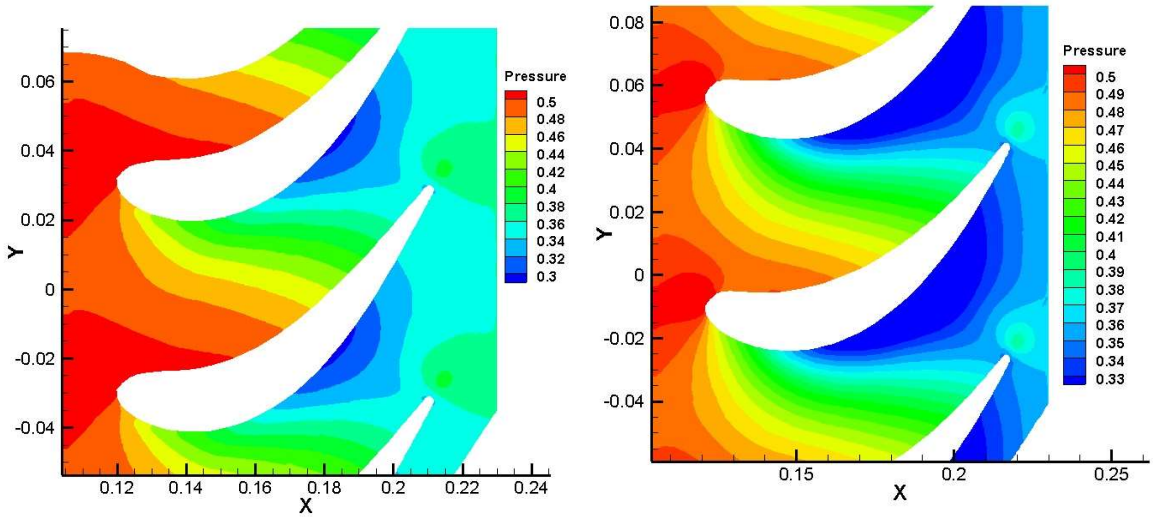

(e) Initial tip **(f) Optimized tip**

Figure 3.15. Pressure contours

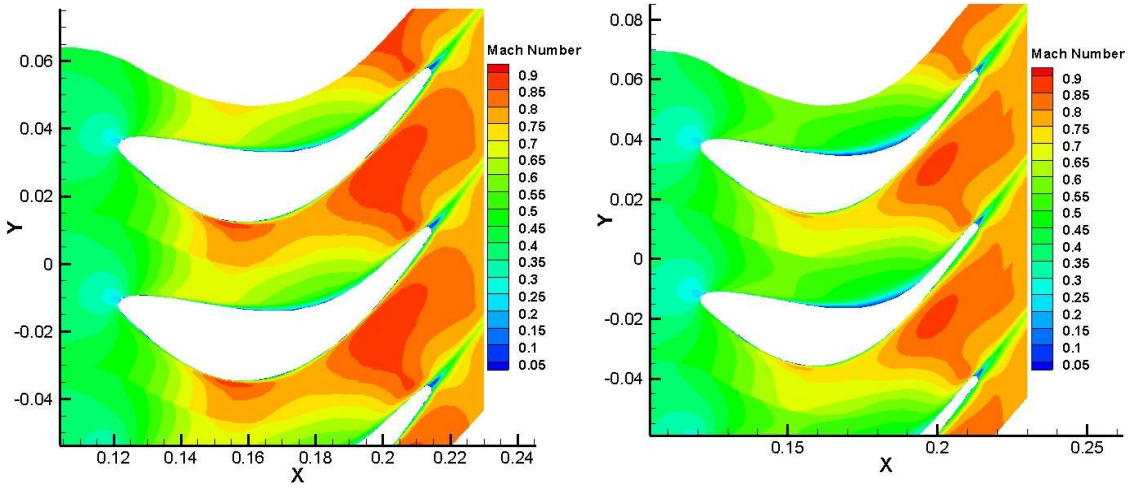

(a) Initial hub **(b) Optimized hub**

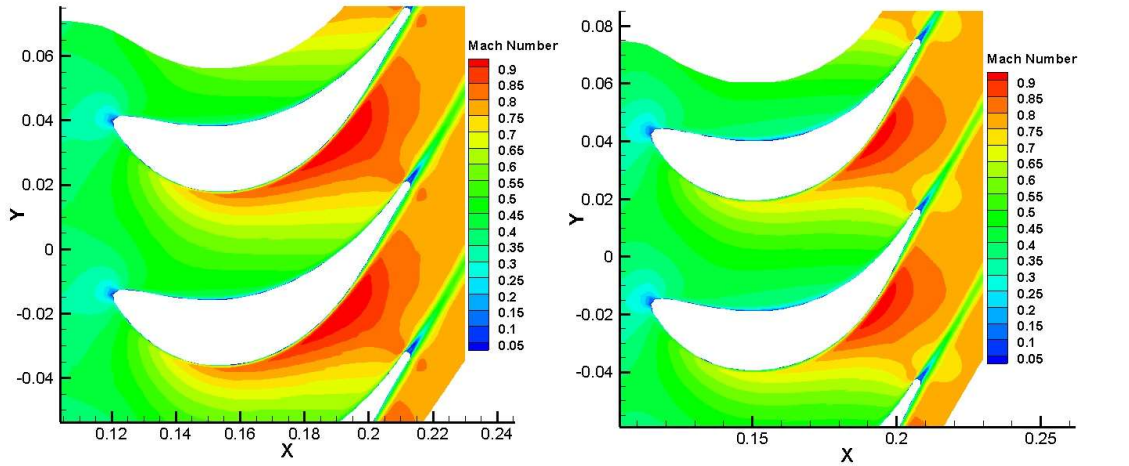

(c) Initial midspan **(d) Optimized midspan**

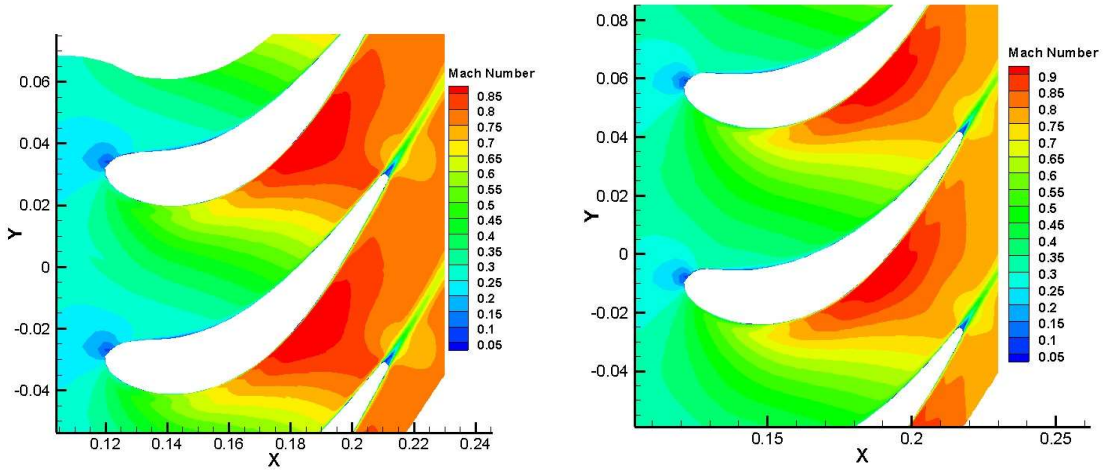

(e) Initial tip **(f) Optimized tip**

Figure 3.16. Mach number contours

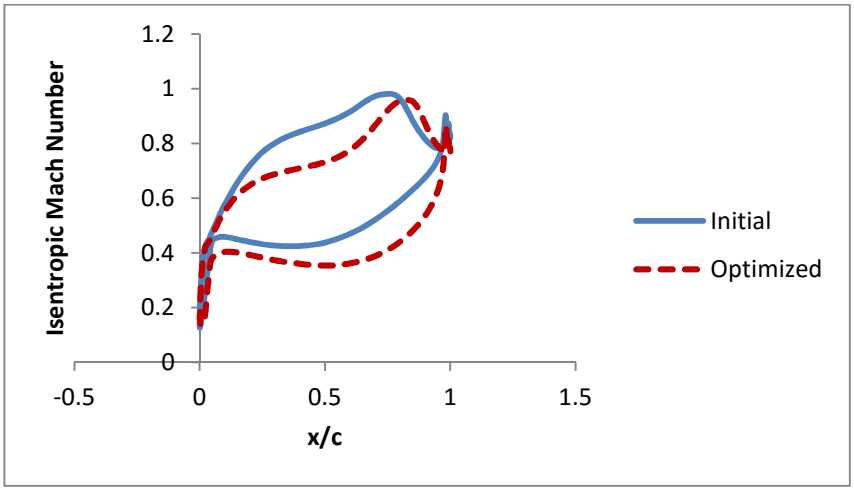

Figure 3.17. Isentropic Mach number along chord length

3.6.3 Case III

3.6.3.1 Aerodynamic Optimization

The final validation case and primary motivation for this research was a complete simultaneous stage optimization. The annular uncooled NASA stage consisted of 50 stator blades and 61 rotor blades. The optimization involved 136 design variables to perform a complete optimization for the lean, sweep, and twist of each blade as well as the hub, midspan, and tip airfoil profiles for the stator and rotor. The initial geometry generated by the optimizer agreed well with experimental data, matching the stage design isentropic efficiency to within 0.4%. An optimized solution was achieved in 34.3 hours, resulting in a 3.25% increase in isentropic efficiency from 0.8814 to 0.9139. Fig. 3.18 shows the total pressure loss distribution for the stator and rotor. The optimized solution decreased the total pressure loss significantly throughout the entire span for both the stator and rotor. The optimal stator geometry resulted in the most gain in efficiency at the hub while the rotor reflected significant gains at both the hub and tip.

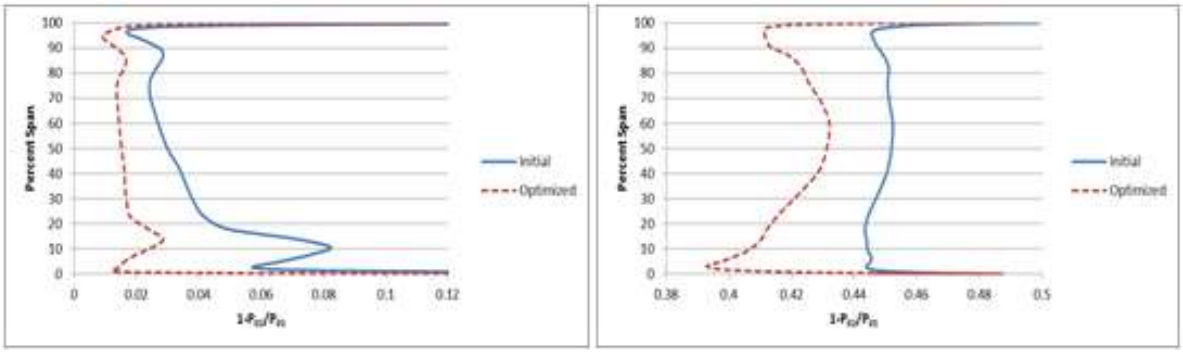

Figure 3.18. Total pressure loss spanwise direction for stator and rotor

Fig. 3.20 reflects the spanwise stacking line for both the initial and optimized stator and rotor. The stator optimal geometry reflects the most significant changes in spanwise geometry specifically for lean and sweep while the rotor optimal stacking line more closely resembles the initial. The airfoil profile geometries are shown in Fig. 3.21 with the pressure and Mach number contours for the stage shown in Figs. 3.22 and 3.23 respectively.

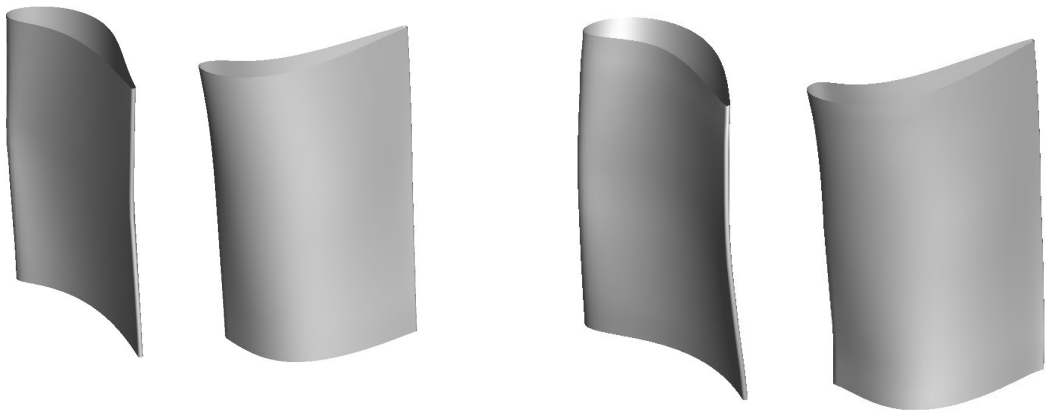

(a) Initial **(b) Optimized**

Figure 3.19. Stage comparison

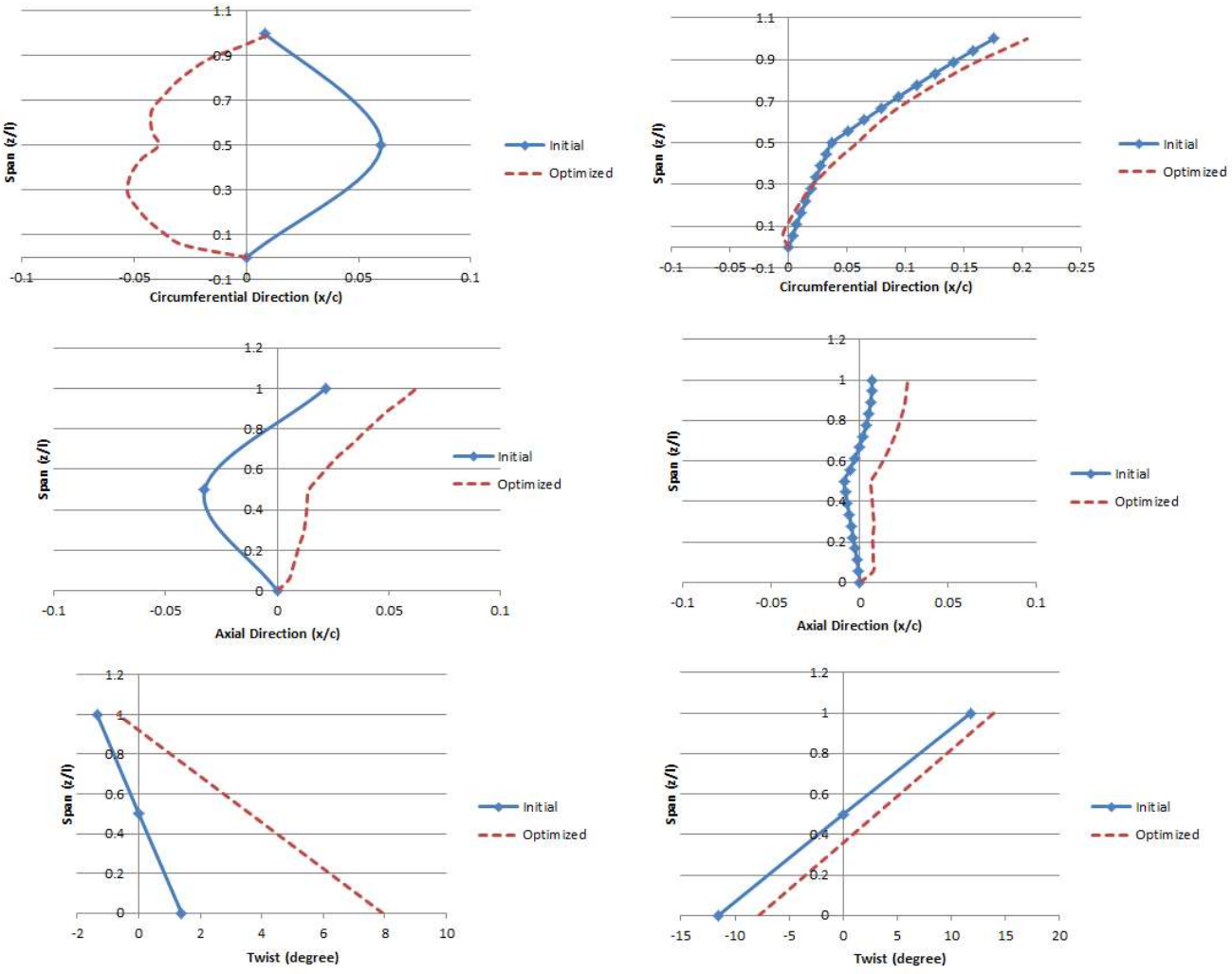

Figure 3.20. Stacking line spanwise direction. Stator (left) lean, sweep, twist (top to bottom). Rotor (right) lean, sweep, and twist (top to bottom).

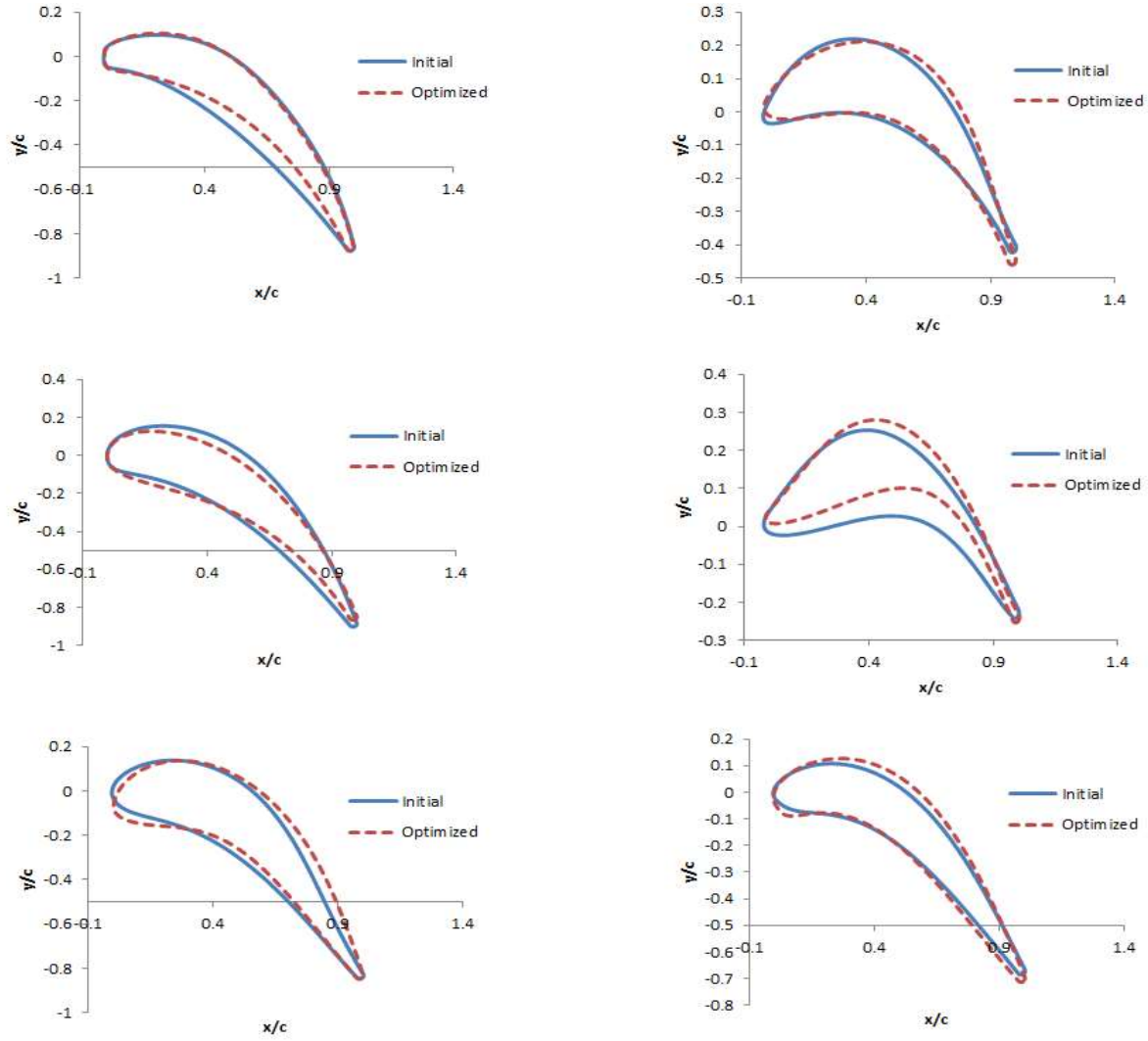

Figure 3.21. Airfoil profile sections. Stator (left) midspan, hub, tip (top to bottom). Rotor (right) midspan, hub, tip (top to bottom).

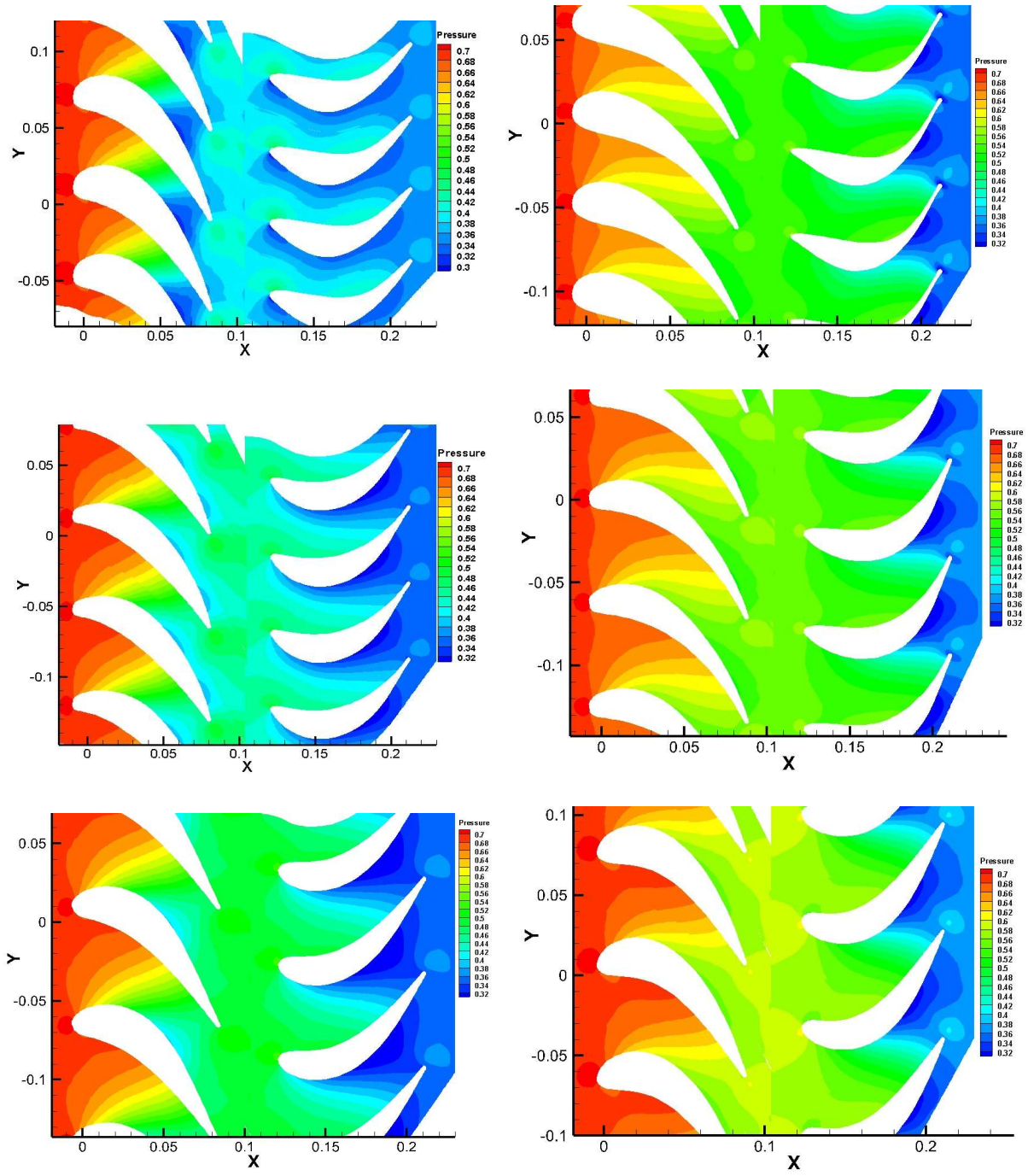

Figure 3.22. Pressure contours. Initial (left) hub, midspan, and tip (top to bottom). Optimized (right) hub, midspan, tip (top to bottom).

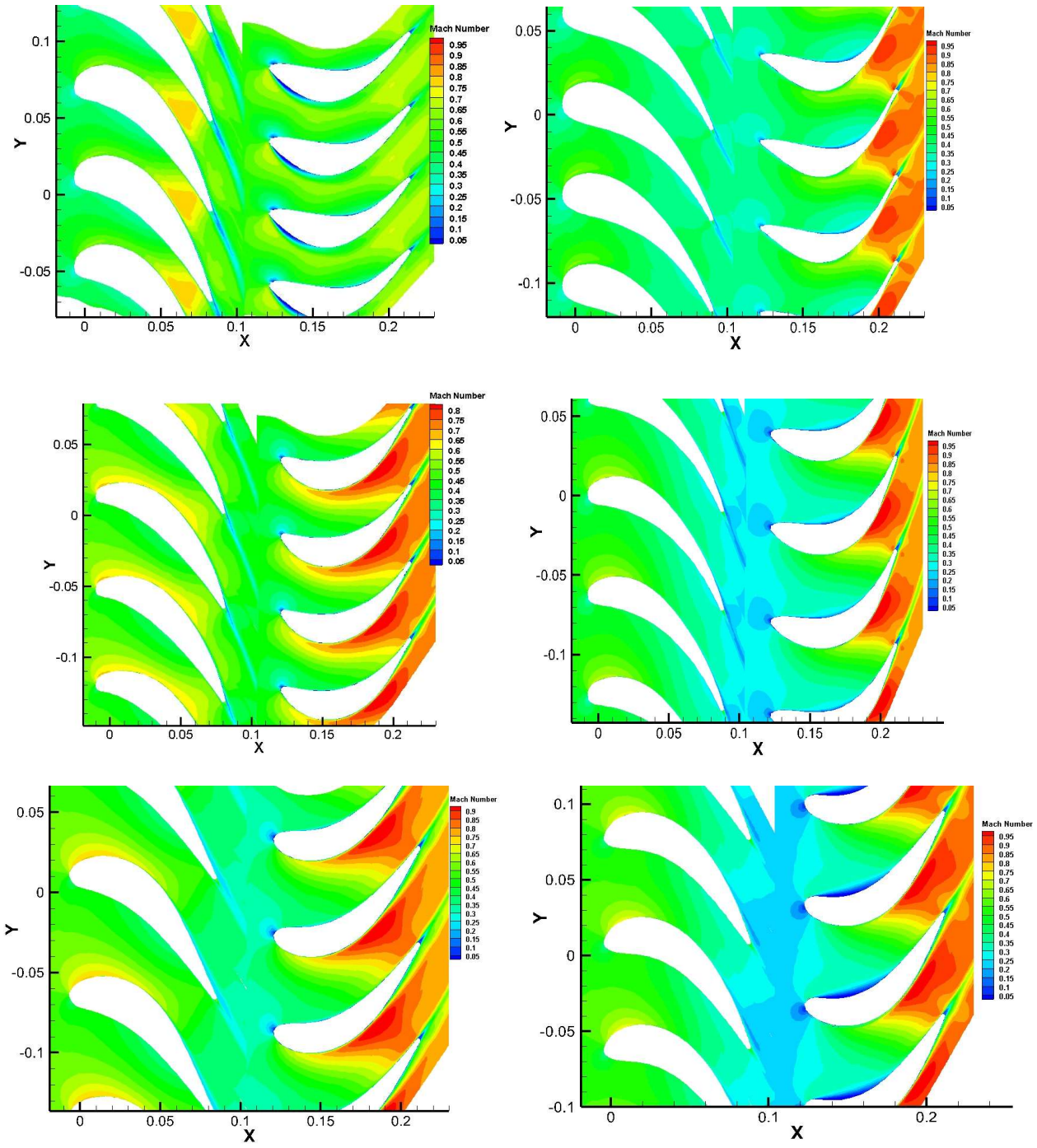

Figure 3.23. Mach number contours. Initial (left) hub, midspan, tip (top to bottom). Optimized (right) hub, midspan, tip (top to bottom).

3.6.3.2 Aerothermal Optimization

An aerothermal optimization was performed on the uncooled NASA turbine stage. The objective function for the evaluation included the stage isentropic efficiency and the heat transfer objective function discussed in section 2.3. Modest gains in both the isentropic efficiency and work output resulted from the optimization. The optimization was performed in 34.8 hours. The optimized stage increased isentropic efficiency by 0.73% from 0.8814 to 0.8878 and increased power output by 0.83%. The optimized solution resulted in a decrease in the total pressure loss for both the stator and rotor as shown in Fig. 3.24. The stacking line in the spanwise direction is shown in Fig. 3.25. The most significant change from the initial stacking line is stator sweep. The airfoil profile sections are shown in Fig. 3.26. The geometries are very similar to the initial airfoil geometries, most likely attributed to the high temperature design of the original stage. The optimized stage solution is show in Fig. 3.27 with the pressure and Mach number contours shown in Figs. 3.28 and 3.29 respectively

.

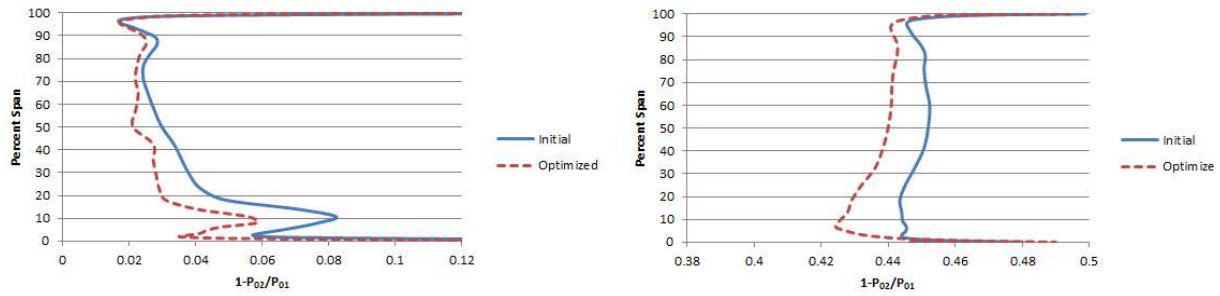

Figure 3.24. Total pressure loss spanwise direction for stator and rotor

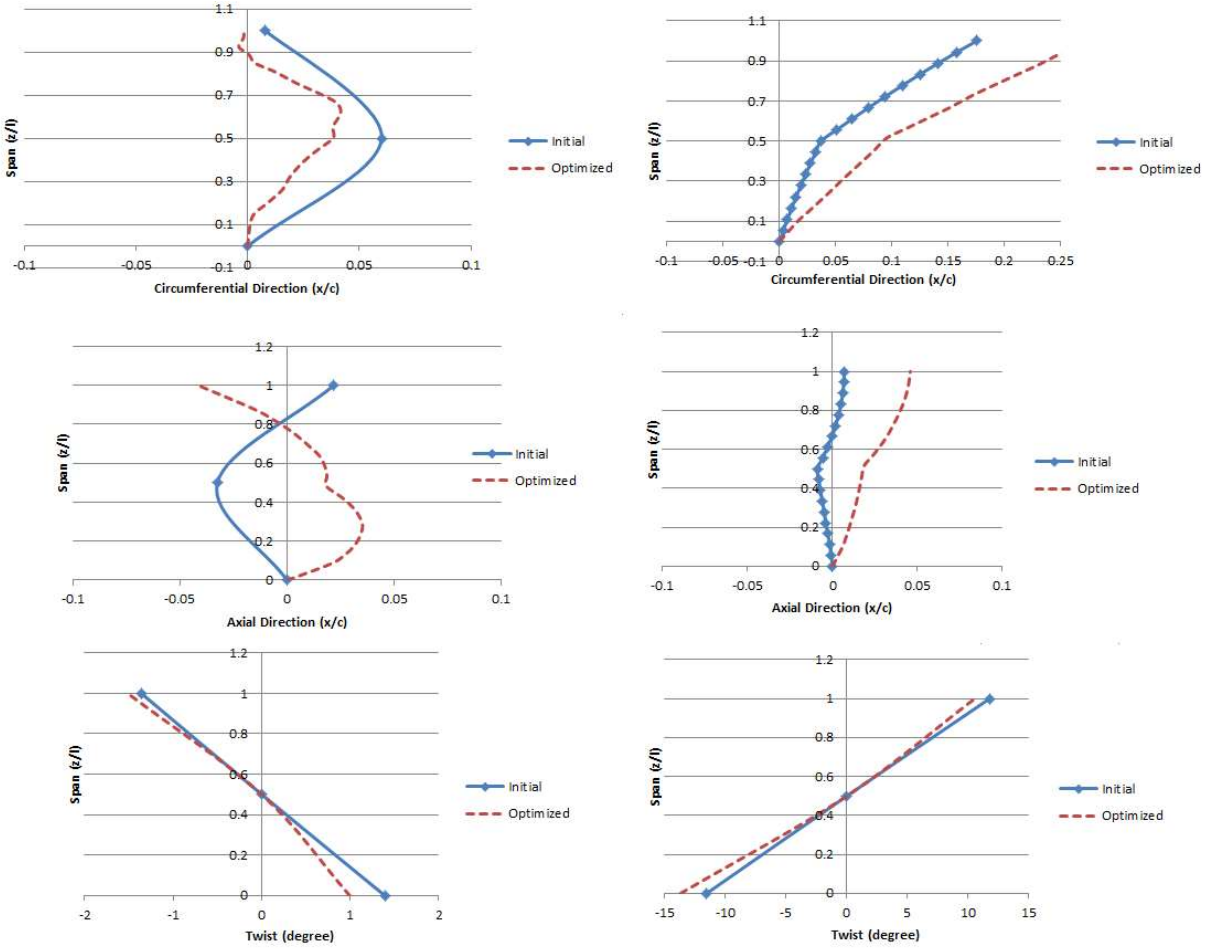

Figure 3.25. Stacking line spanwise direction. Stator (left) lean, sweep, twist (top to bottom). Rotor (right) lean, sweep, and twist (top to bottom).

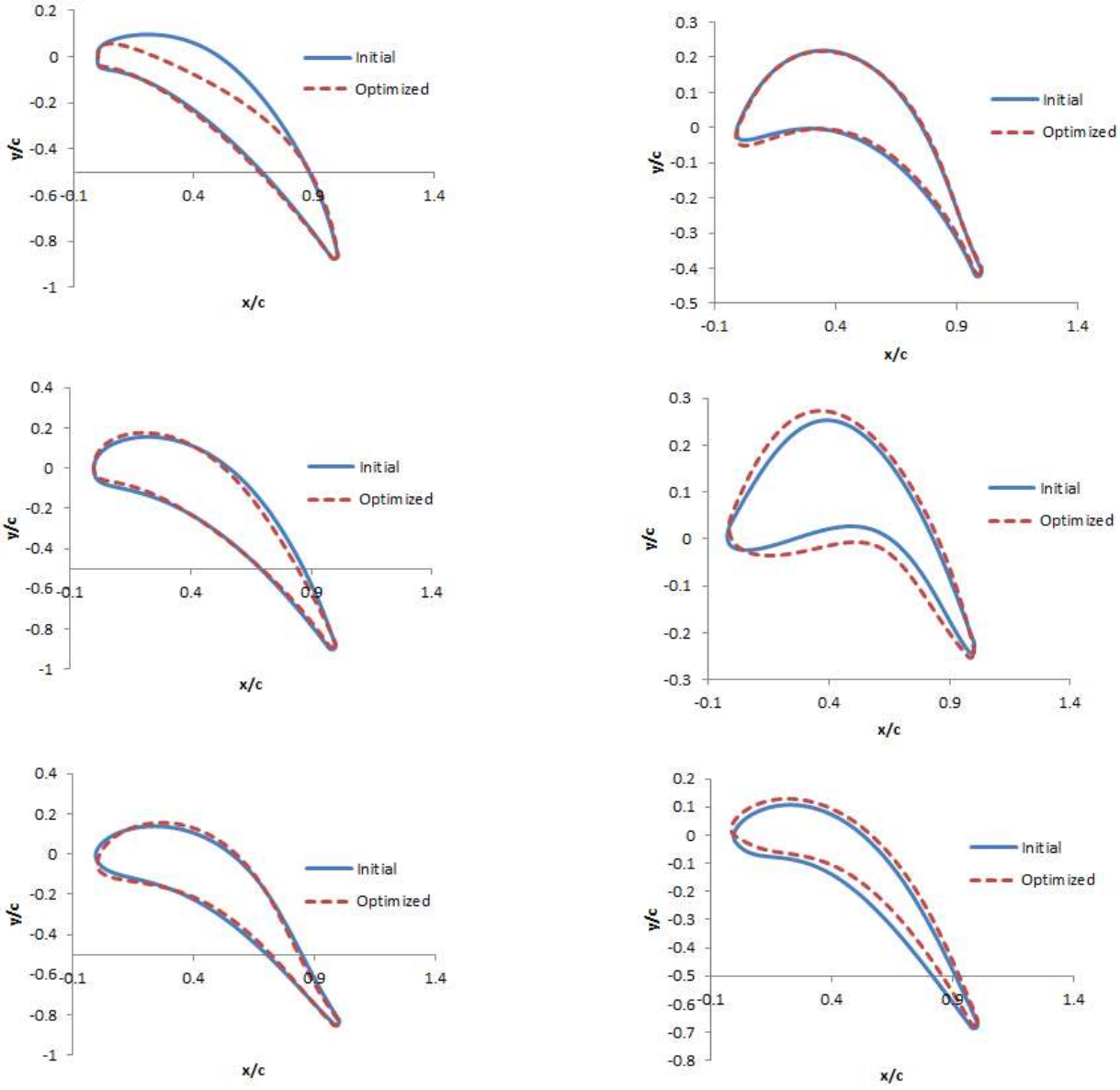

Figure 3.26. Airfoil profile sections. Stator (left) midspan, hub, tip (top to bottom). Rotor (right) midspan, hub, tip (top to bottom).

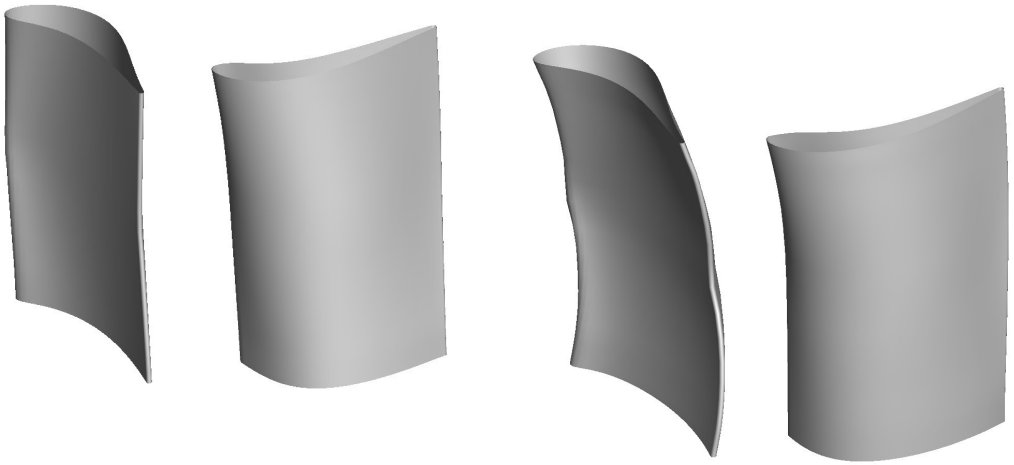

(a) Initial **(b) Optimized**

Figure 3.27. Stage comparison

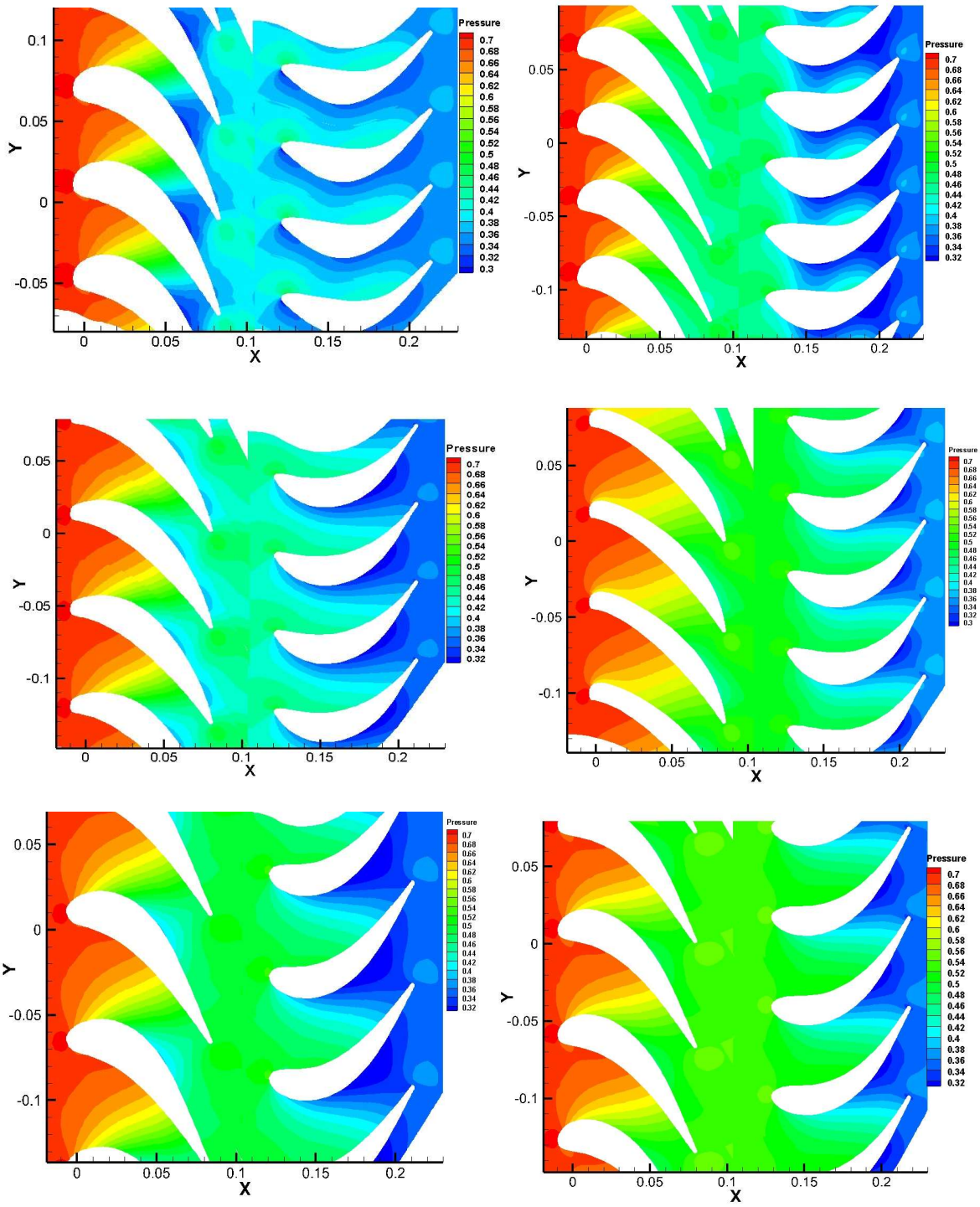

Figure 3.28. Pressure contours. Initial (left) hub, midspan, and tip (top to bottom). Optimized (right) hub, midspan, tip (top to bottom).

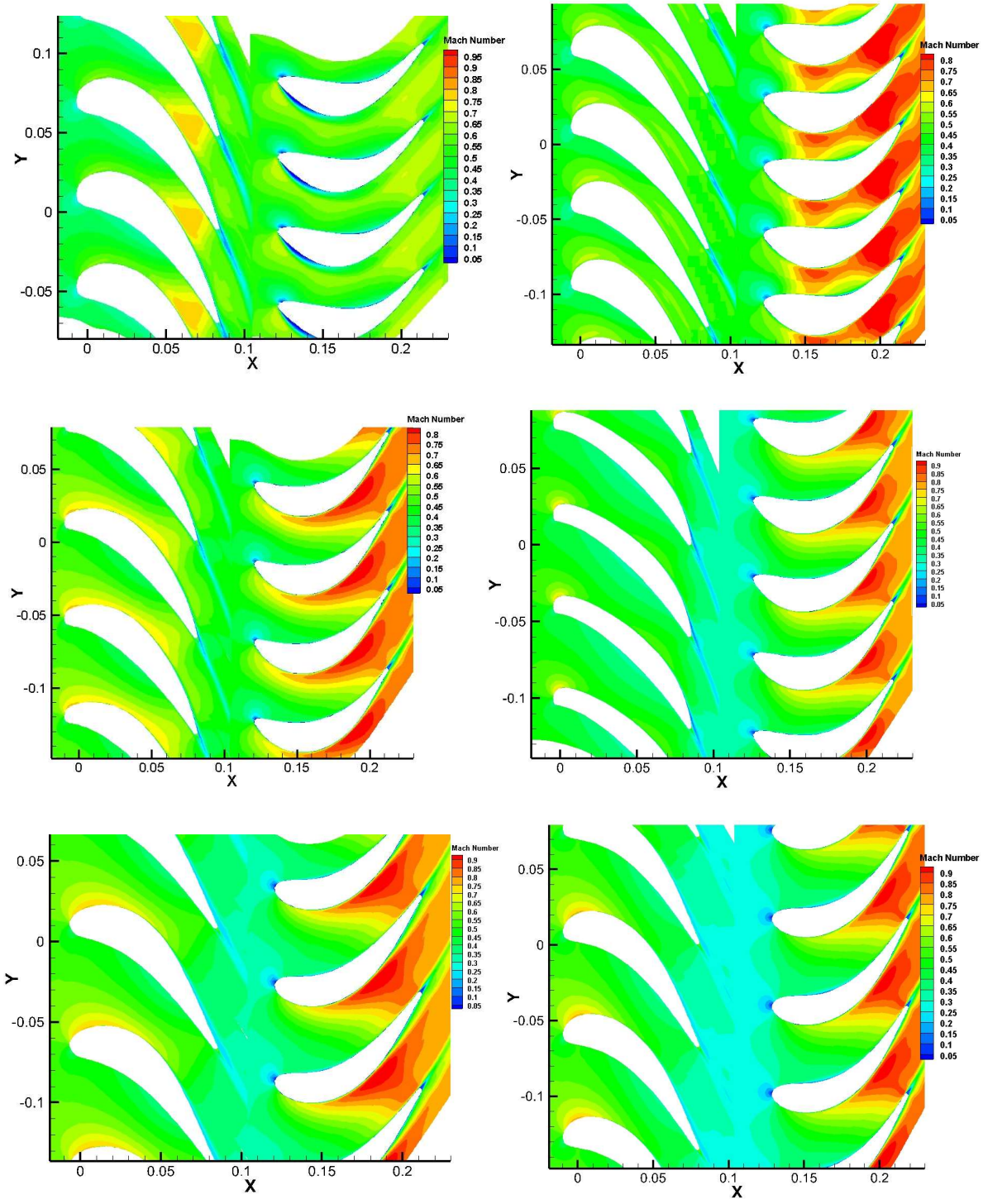

Figure 3.29. Mach number contours. Initial (left) hub, midspan, tip (top to bottom). Optimized (right) hub, midspan, tip (top to bottom).

3.6.3.3 Comparative Aerodynamic and Aerothermal Optimized Stage Results

A final comparison between the optimized aerodynamic and aerothermal solutions are shown in this section. The isentropic efficiency results are shown in Table 3.1. The aerothermal optimization resulted in a 0.73% increase in isentropic efficiency versus a 3.25% increase for the aerodynamic solution; however, the aerothermal solution produced a 0.85% work increase as a result of the increase in the heat transfer coefficient. These results indicate the trade-off between a stage solution with optimal efficiency and one that is both more efficient than the initial stage as well as capable of producing more work.

Table 3.1. Results Aerodynamic and Aerothermal Optimizations

	Isentropic Efficiency		Work increase
Run	Initial	Optimized	
Aerodynamic	0.8814	0.9139	--
Aerothermal	0.8814	0.8878	0.85%

The spanwise pressure distribution comparison for the aerothermal and aerodynamic solutions is shown in Fig. 3.30. As expected, the aerodynamic solution resulted in the largest decrease in spanwise total pressure loss from the initial stage.

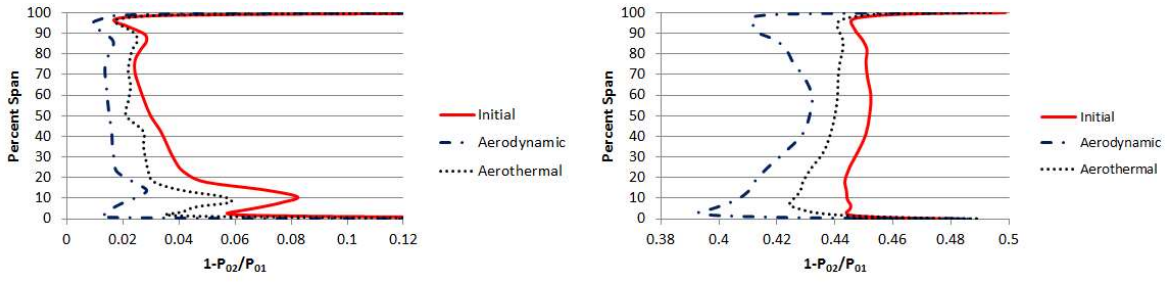

Figure 3.30. Total pressure loss spanwise direction for stator and rotor

The spanwise stacking line and airfoil profile section comparison is shown in Figs. 3.31 and 3.32 respectively. The stator is observed to change the most in the spanwise direction from the initial geometry as compared to the rotor.

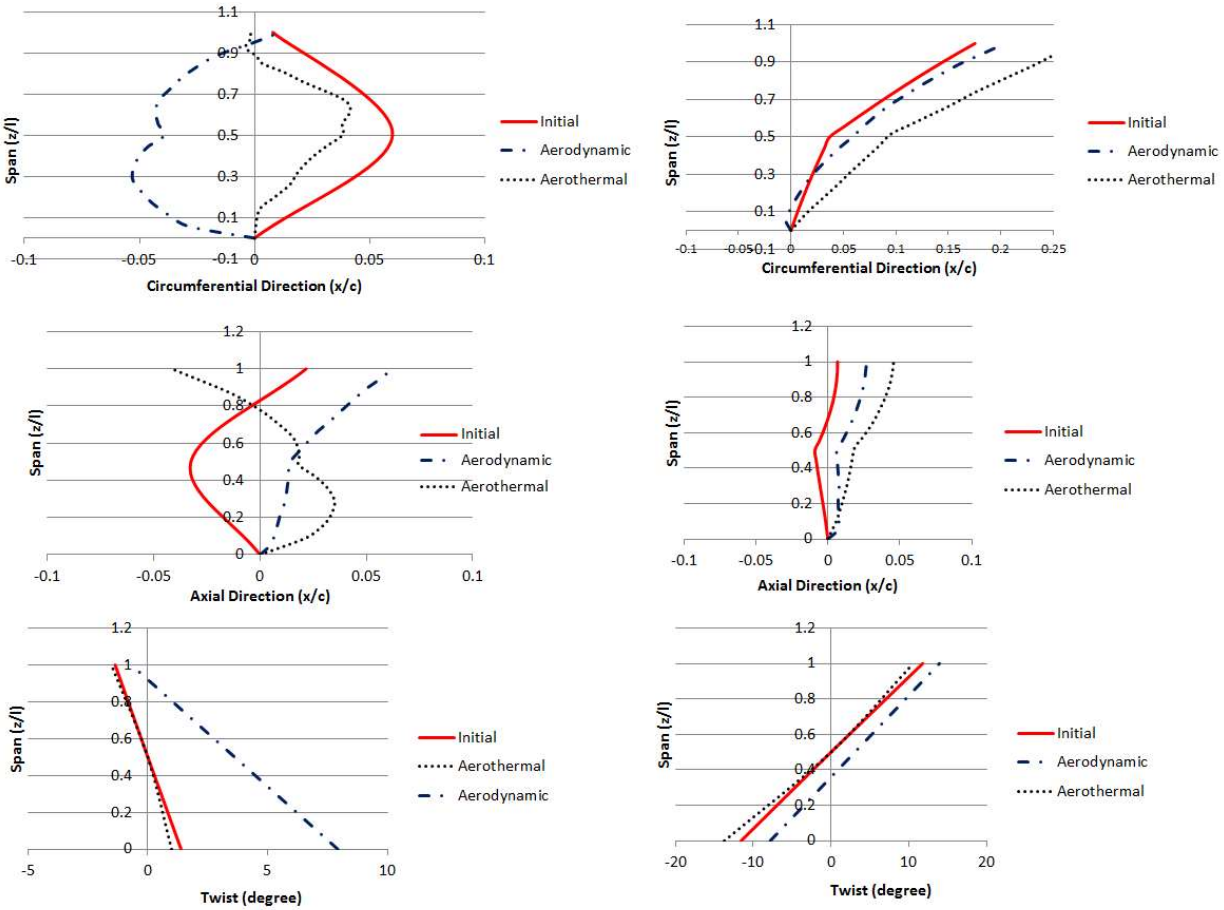

Figure 3.31. Stacking line spanwise direction. Stator (left) lean, sweep, twist (top to bottom). Rotor (right) lean, sweep, and twist (top to bottom).

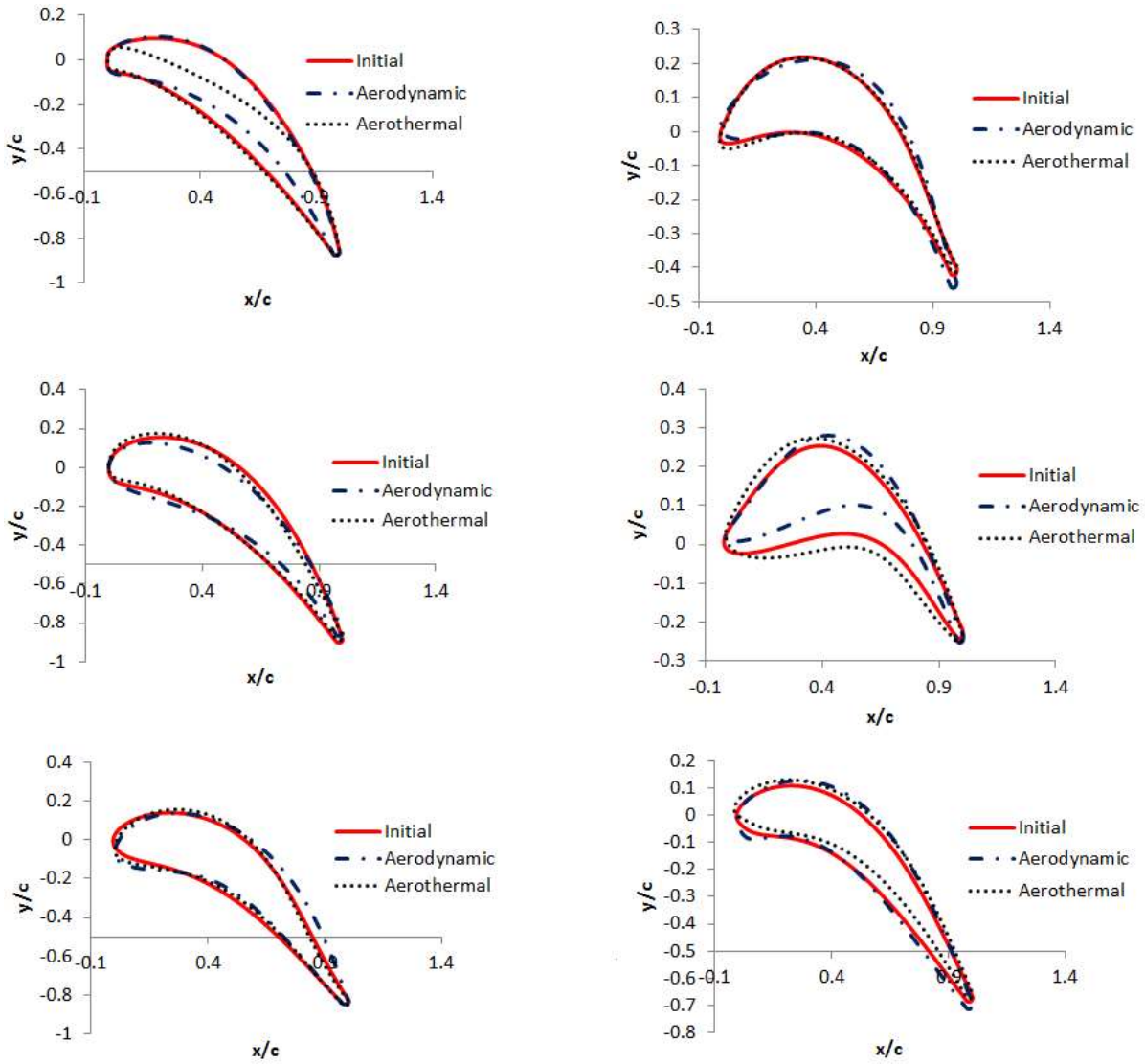

Figure 3.32. Airfoil profile geometry. Stator (left) midspan, hub, tip (top to bottom). Rotor (right) midspan, hub, tip (top to bottom).

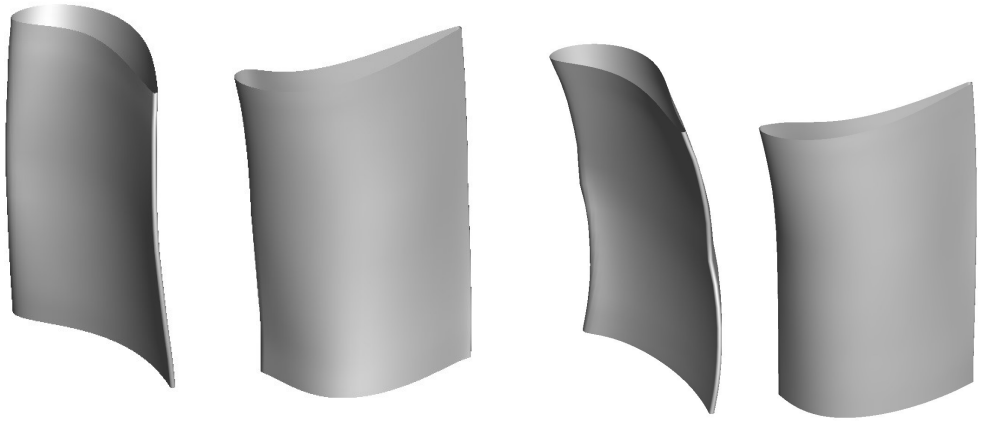

(a) Aerodynamic **(b) Aerothermal**

Figure 3.33. Stage comparison optimized solutions

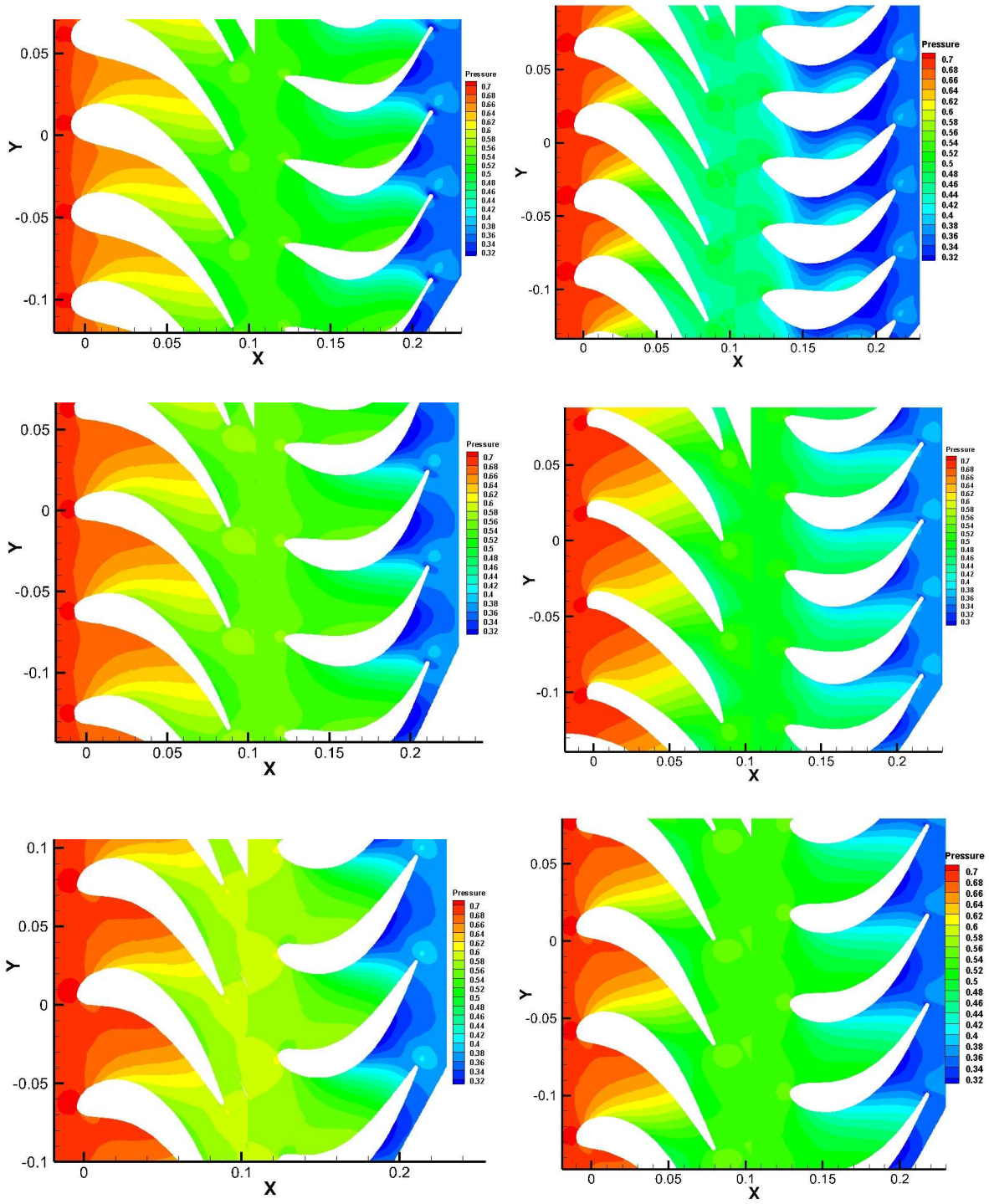

Figure 3.34. Pressure contours. Aerodynamic solution (left) hub, midspan, and tip (top to bottom). Aerothermal solution (right) hub, midspan, tip (top to bottom).

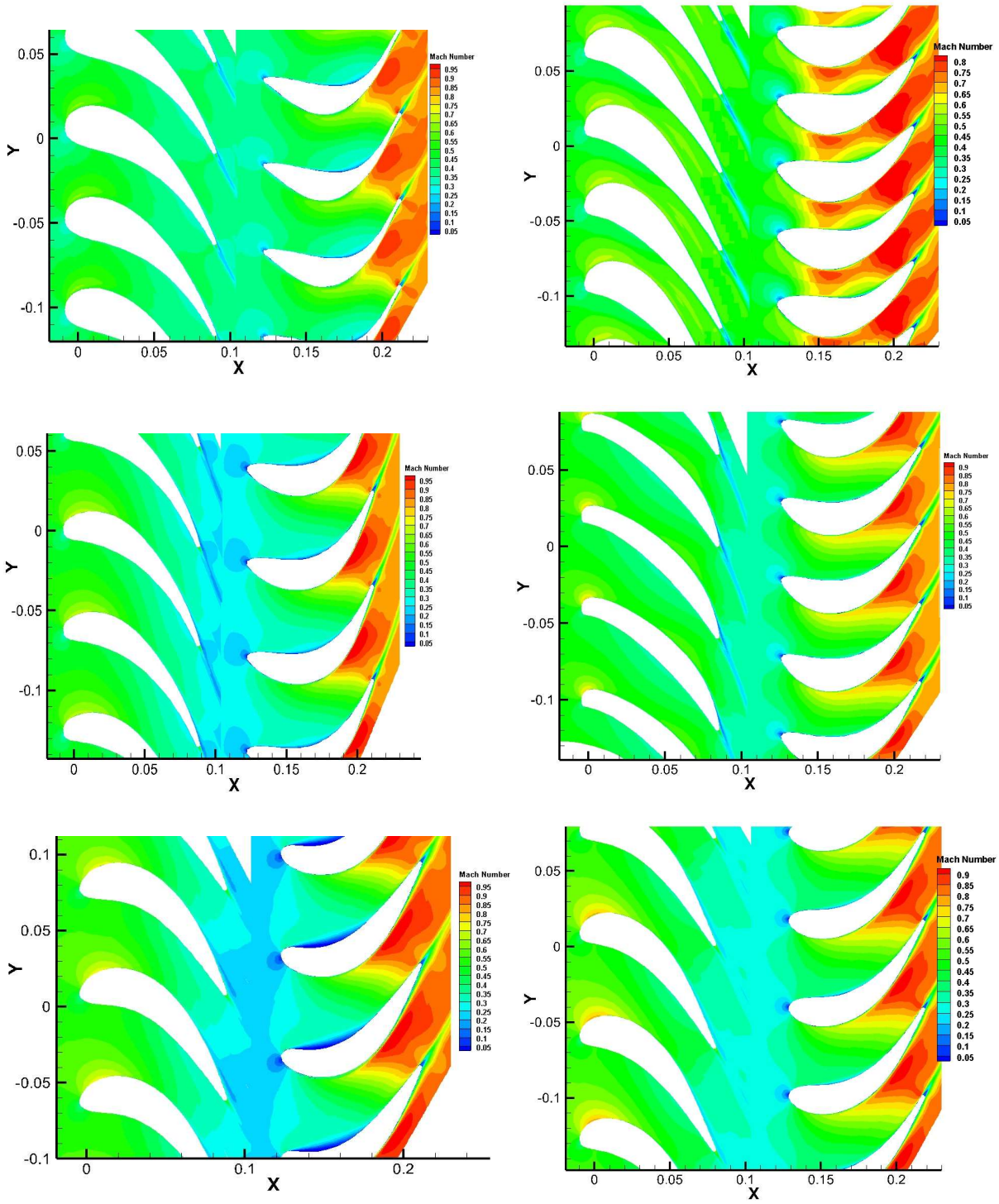

Figure 3.35. Mach number contours. Aerodynamic solution (left) hub, midspan, and tip (top to bottom). Aerothermal solution (right) hub, midspan, tip (top to bottom).

3.7 Three-Dimensional Optimization Summary

In order to meet the demand for a high performing turbine engine, an optimization technique that produces reliable and optimal stage results within a reasonable time period is critical. Many three-dimensional optimizers exist, but currently fall short of producing an optimal solution as they fail to provide a complete optimization by only optimizing in the blade-to-blade direction,[14] or only in the spanwise direction,[10] or failing to take into account structural consideration as well as failing to converge in an acceptable time frame. An efficient evolutionary genetic algorithm was paired with a Navier-Stokes CFD code and a 64 processor computer cluster to optimize a turbine stage in well less than two days. Results indicate that the optimizer was successful in improving the isentropic efficiency by 3.25% for the aerodynamic optimization in a significantly reduced time frame than other optimizers utilizing Navier-Stokes flow solvers. The solution was achieved while maintaining 2-D and 3-D structural requirements as well as a monatomically increasing Mach number across the suction surface of the blade and ensuring an adequate uncovered turning angle. An aerothermal optimization also resulted in modest gains for both the stage isentropic efficiency with a 0.75% increase and work output with a 0.85% increase. These results suggest a strong potential for use of this optimizer in an engine simulation program in which the aerodynamic or aerothermal optimization of a turbine stage is expected to result in an increase in engine performance.

Chapter 4

NPSS Model and Optimizer Validation

An important part of this research involves the model used to complete the turboramjet optimization. Since data and performance specifications are very limited in regards to turboramjet engines, it is not possible to validate such as engine with confidence in a simulation program. For this reason, it was decided that a low bypass turbofan engine, the F100-PW229, would be used for model validation in the simulation program in addition to validating the optimization sequence. This engine was chosen as most of the engine performance specifications are readily and publicly available, thus enabling the model to be adequately validated. In addition, the current design of the SR-72 entails integrating a COTS turbine engine into the turbine based combined cycle to save on design and development costs. This engine has the performance capability to reach a Mach number in which transition to a ramjet cycle is feasible and thus may be a suitable candidate for integration into the TBCC for the SR-72.

The baseline F100 engine will first be modeled and validated in Numerical Propulsion System Simulation (NPSS). NPSS was chosen as the simulation code for this research as it is increasingly becoming the industry standard in propulsion simulation and is currently used in commercial and government enterprises. The code allows for maximum modeling flexibility and is easily integrated into the optimization algorithm. Following the baseline engine validation, an ITB will be inserted between the HPT and LPT. The performance of the engine with the ITB will be presented. The final step of the model validation includes integrating the optimization

algorithm into the high pressure and low pressure turbine stages, defining an engine performance objective function, and running the complete hot section optimization.

4.1 Baseline F100-PW229 Engine Model

The F100-PW229 engine is a low bypass two spool turbofan engine used in the F-15 and F-16 fighter aircrafts. The cross section of the engine is shown in Fig. 4.1.

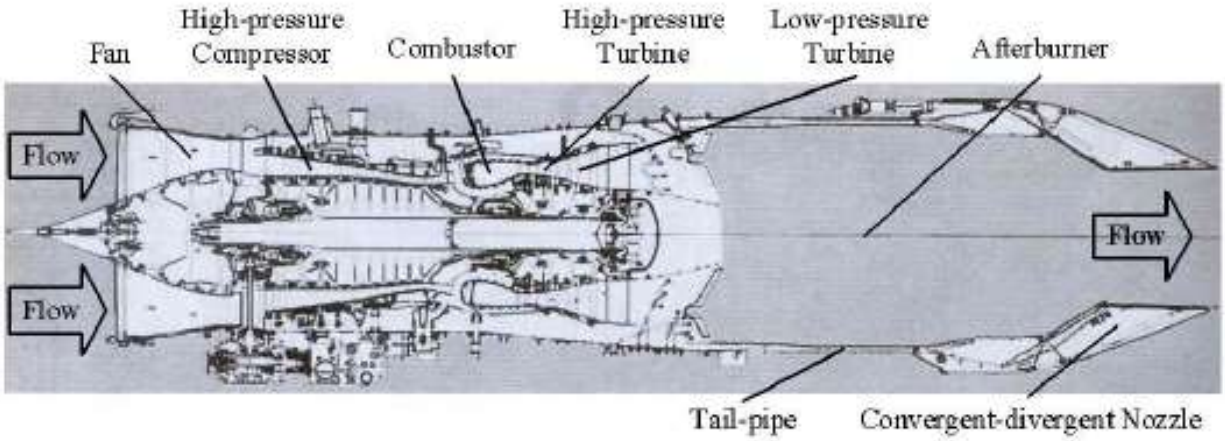

Figure 4.1 F100 cross section

Due to the dearth of complete publicly available data on the F100-PW229 engine or any military engine for that matter, an equivalent engine was modeled in which the engine's thrust and fuel consumption rates for mil and max power agree to within 2%. Data from publicly available literature was used to model the engine's characteristics and its components' characteristics. Generic data and engineering judgement was used where specific data for the F100 engine was not available with the objective of modeling an equivalent F100-PW229 engine in which the performance is very close to that of an actual F100-PW229 engine.

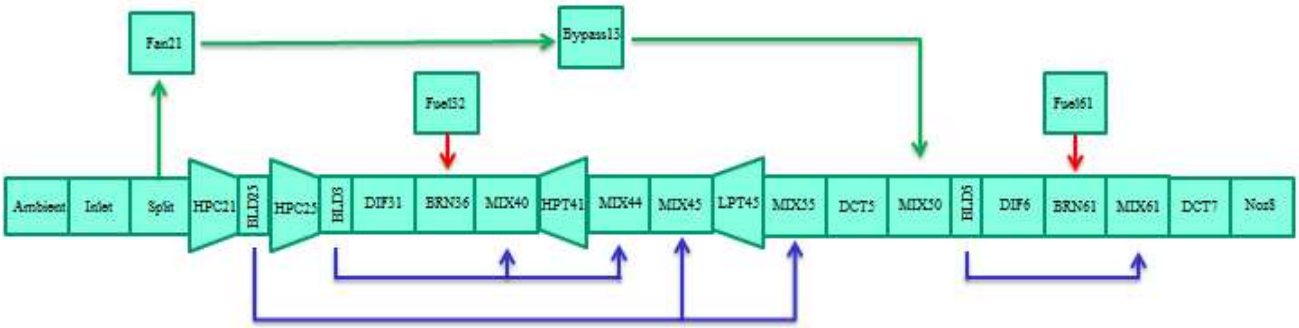

Figure 4.2. F100 equivalent engine schematic modeled in NPSS

The schematic of the F100 engine modeled in NPSS is shown in Fig. 4.2. After flow enters the inlet, it is split at a bypass and enters a 3 stage fan and 11 stage high pressure compressor (HPC). Bleed air is taken from mid-stage of the HPC to cool the low pressure turbine (LPT). For this reason the compressor is split into HPC21 and HPC25 for modeling purposes. Cooling flow is drawn from the exit of the HPC to cool the high pressure turbine (HPT). Mixers are introduced before and after the LPT and HPT to mix the cooling air with flow through the engine. Additional bleed air is taken from the core air after the bypass air is mixed back in and used for afterburner liner cooling.

The characteristic and component performance parameters used for the engine model are shown in Tables 4.1 and 4.2. These parameters were fined tuned to yield a thrust and TSFC at max and mil power that were very close to published values for the F100-PW229 engine.

Table 4.1. F100 Engine Performance Parameters

Parameter	Mattingly/Engine Handbook	P&W	NPSS
$\dot{m}$ (lbm/s)	248	---	248
OPR	32	32.4	32.4
FPR	3.8	---	3.8
BPR	0.4	0.36	0.36
Tt4 (R)	3160	---	3160

Table 4.2. F100 Parameter Comparison

Parameter	Mattingly		NPSS
	1965-1985	1985-2005	
e_c	0.84	0.88	0.84
e_f	0.82	0.86	0.83
η_b	0.94	0.99	0.99
π_b	0.92	0.94	0.95
e_t	0.83	0.87	0.86
η_{AB}	0.91	0.96	0.91
π_{AB}	0.92	0.94	0.95
π_n	0.93	0.95	0.97
Tt7 (R)	3000	3600	4133

Particular care was taken in the modeling of the cooling air for the HPT and LPT as initial runs indicated that TSFC could vary considerably for the same thrust levels depending on the cooling air percentage.

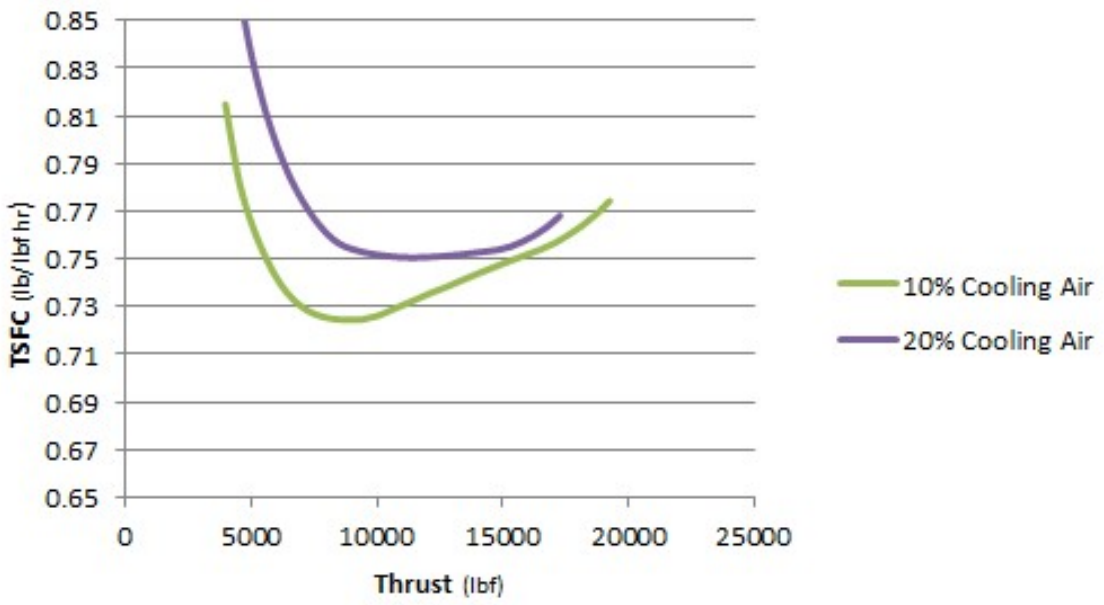

Figure 4.3. Cooling air comparison

The methodology of Young et al[44] was chosen to model the turbine cooling requirement for this work due to its flexibility and applicability to future studies. The cooling flow is first estimated and input into the engine model. Upon running the engine model, Eqs. (4.1)-(4.4) are used to calculate the actual cooling flow required for the high pressure and low pressure turbines. If the difference between the initial and calculated cooling flow is below the specified tolerance, the initial cooling flow is replaced by the calculated value and the model is run again until the tolerance is met. Although an iterative and somewhat tedious process, it does provide for an accurate cooling method solution.

$$\varepsilon_0 = \frac{T_{t_{gas}} - T_{metal}}{T_{t_{gas}} - T_{t_{cl}}} \tag{4.1}$$

$$Bi_{total} = Bi_{tbc} - Bi_{metal}\frac{\varepsilon_0 - \varepsilon_{film}}{1-\varepsilon_0} \tag{4.2}$$

$$\varsigma = \frac{\varepsilon_0 - \varepsilon_{film}[1 - \eta_{\text{int}}(1 - \varepsilon_0)]}{\eta_{\text{int}}(1 - \varepsilon_0)} \tag{4.3}$$

$$\phi_{cl} = \frac{\dot{m}_{cl}}{\dot{m}_{gas}} = \frac{K_{cool}\varsigma}{1 + Bi_{total}} \tag{4.4}$$

The accuracy of the cooling flow rate depends on the values in the above equations. These values are obtained by experiments and depend heavily on cooling technologies and turbine design. The values in Table 4.3 summarize those from Reference 45 and those chosen for this engine. The values used for this current work assume that the F100 technology is two generations behind the current technology in 2005.

Table 4.3 Cooling Air Performance Parameters

	Kcool	η_{int}	ε_{film}	Bimetal	Bitbc
F100-EQ Engine	0.045	0.6	0.3	0.15	0.1
Current technology	0.045	0.7	0.4	0.15	0.3
Advanced technology	0.045	0.75	0.45	0.15	0.4
Super advanced technology	0.045	0.8	0.5	0.15	0.5

The baseline F100-PW229 engine modeled in NPSS was run at max and mil power and thrust TSFC performance values were compared to published values. All values agreed to within 2%, thus validating the NPSS baseline model as shown in Table 4.4. The complete NPSS code for the F100 equivalent engine is shown in Appendix B.

Table 4.4. F100 Engine Performance Comparison

	Parameter	Mattingly/Engine Handbook	P&W	NPSS
Mil Power	Thrust (lbf)	17,800	17,800	17963
	TSFC (lbm/lbf hr)	0.74	0.76	0.7696
Max Power	Thrust (lbf)	29,000	29,160	28,505
	TSFC (lbm/lbf hr)	2.05	2.06	2.05

4.2 F100-PW229 Engine Model with an Interstage Turbine Burner

Following the validation of the baseline F100 engine model in NPSS, a burner was inserted between the high pressure and low pressure turbines. Both the conventional F100 engine model and the two combustor model were run at design point of sea level static. In addition, the conventional model was run with full afterburner at design point.

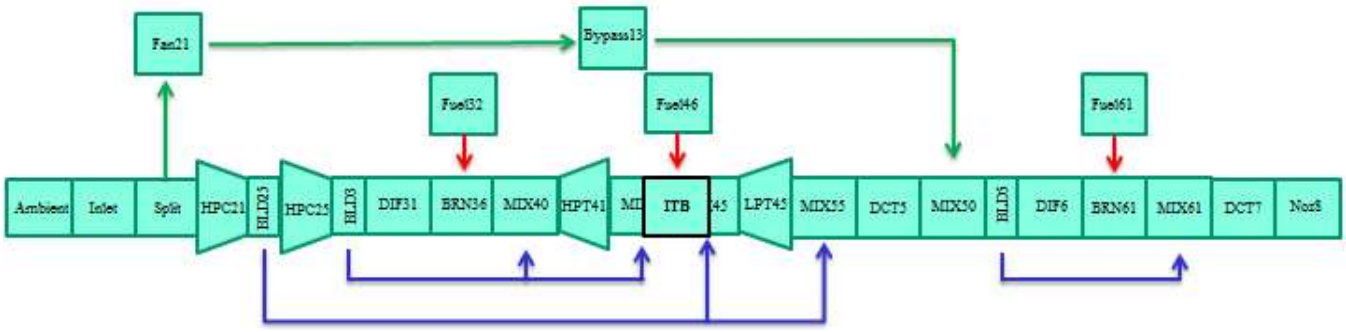

Figure 4.4. F100 equivalent engine with ITB schematic modeled in NPSS

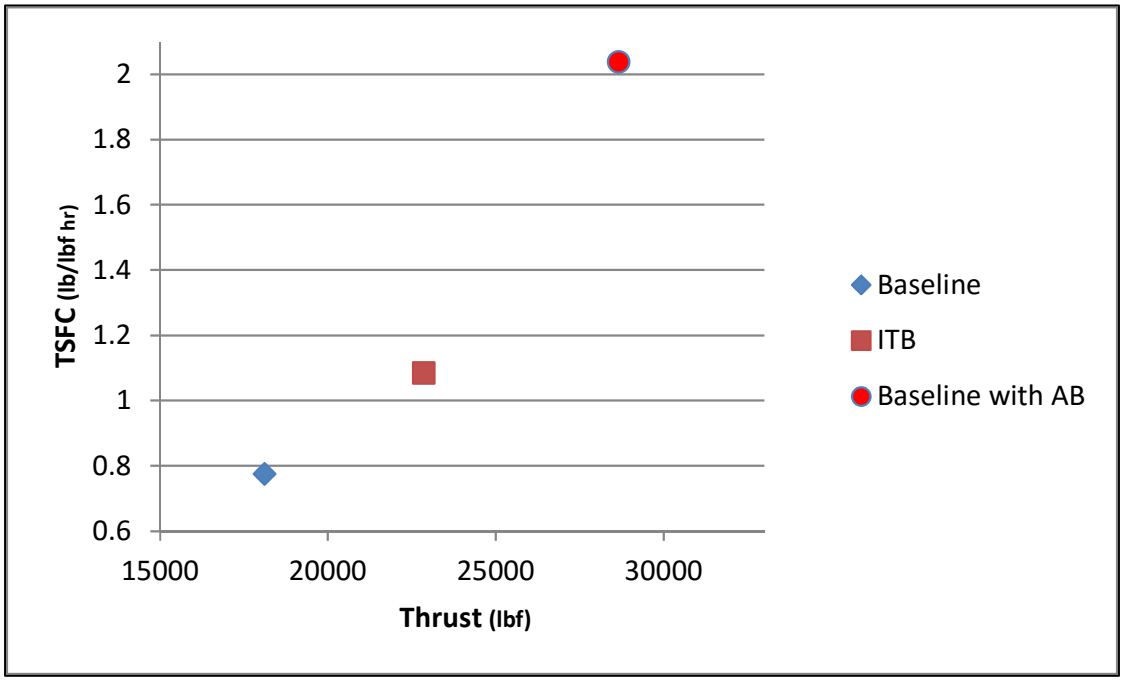

Figure 4.5. Performance of conventional and two combustor engine at sea level static

As seen from Fig. 4.5, the performance of the engine with the interstage turbine burner at design point lies between that of the baseline F100 engine model without afterburning and that of the baseline model with afterburning as expected. In order to compare the efficiency of the three configurations, the baseline engine and ITB engine were run off-design from Mach 0.2 to 0.8 at 20,000 ft. The baseline engine with the afterburner throttled back to match the thrust of the ITB engine was also run at the same off-design conditions. The results are shown in Fig. 4.6.

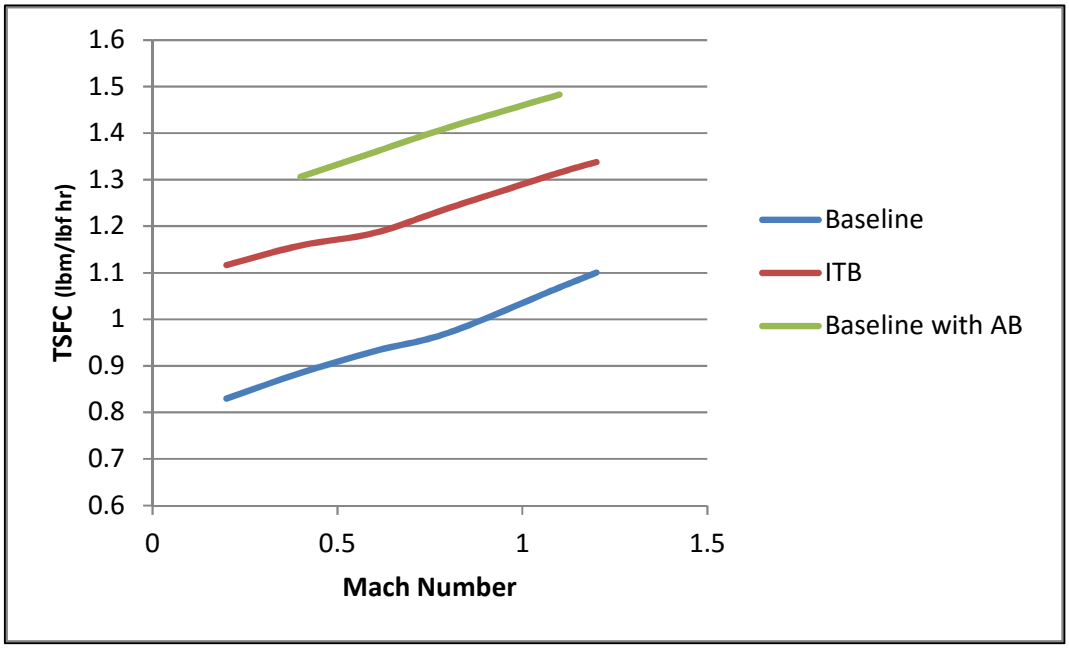

Figure 4.6. Off-design performance at 20,000 ft. Baseline engine with afterburning throttled back to produce thrust equal to ITB engine configuration

From Fig. 4.6, the engine configuration with an interstage turbine burner is an average of 14% more efficient than the F100 with the afterburner producing the same thrust at 20,000 feet over the Mach number range of 0.2 to 0.8.

The above results indicate that the thrust of an engine with an interstage turbine is greater than that of a conventional one combustor engine, but less than that of a conventional engine with an afterburner. The ITB engine configuration is also more efficient that the conventional engine with afterburning at the same thrust level. The conclusions can be drawn that an interstage turbine burner is advantageous when additional thrust augmentation is needed for a conventional one combustor engine running at full afterburner. The thrust augmentation from the ITB will allow for additional thrust, but more efficiently than a traditional afterburner. For this

reason an ITB would be advantageous to use at the transition point of the turbine based combined cycle in which additional thrust is needed via the most efficient means possible.

4.3 F100 Model and Hot Section Optimization

The vast majority of turbine optimization research involves solely optimizing the turbine independently for one or more objective functions. This optimization is performed under the assumption that optimal results for an engine such as maximizing thrust and minimizing TSFC will be realized once the optimized turbine is incorporated into the engine. This is not necessarily a valid assumption as a turbine optimized for a particular objective may not necessarily lead to optimal engine results. To mitigate this, the next part of this research involves coupling the F100 model with the optimizer and optimizing the hot section for maximum thrust and minimum TFSC. Optimized results are then compared to the baseline model with and without an interstage turbine burner. It is expected that the addition of an ITB will allow for an increased maximum Mach number for the engine. In addition, an optimized HPT and LPT should allow for a decrease in TSFC of the engine cycle. Results similar to those achieved in this validation case are expected for the turboramjet hot section optimization.

4.3.1 F100 Model and Optimization Routine

The genetic algorithm optimization routine to optimize the high and low pressure turbines was incorporated into the F100 model with and without an ITB as shown in Fig. 4.7. A typical optimization begins with the NPSS model in which case the model runs and records the inlet properties to the high pressure turbine. The offspring high pressure turbine geometries are then generated through the optimizer and the exit properties of the HPTs are calculated using the CFD results and inlet properties to the turbine. The model then uses the exit properties of the offspring

turbines to run the NPSS model through the cooling mixers and interstage turbine burner if one exits. The offspring low pressure turbine geometries are then generated through the optimizer and the exit properties of the LPTs are then calculated using the CFD results and the inlet properties to the turbine. The model then inputs the exit properties of the LPTs to the inlet of MIX55 and runs the NPSS model through the end to the nozzle. Finally the objective function of TSFC and thrust of all the offspring models are calculated and the best model/turbines are selected as the parent model. The next generation then begins and the process repeats itself until an optimized hot section is found.

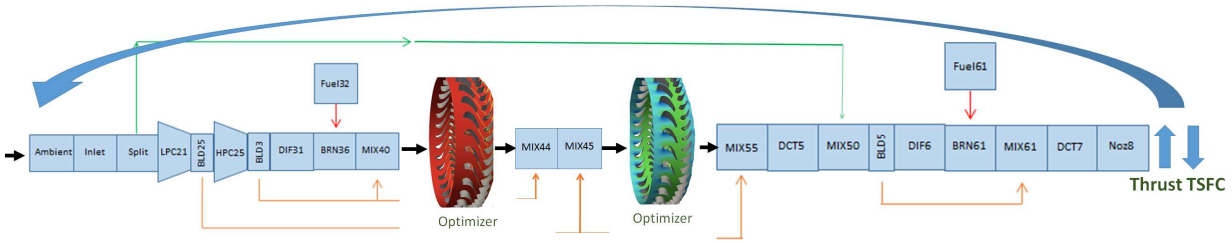

(a)

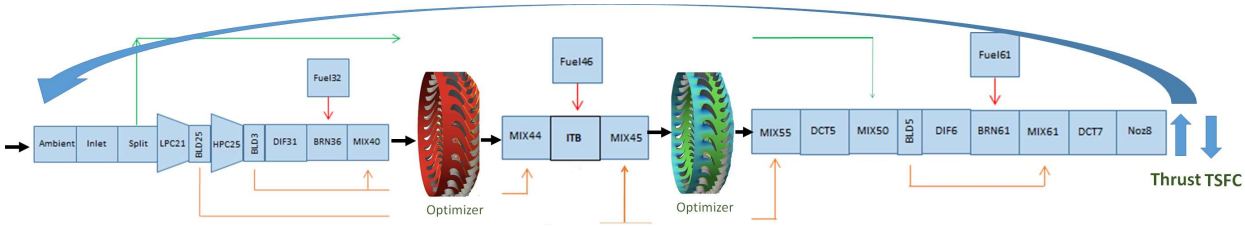

(b)

Figure 4.7. F100 model with turbine optimizer (a) without an ITB (b) with at ITB

An aerothermal optimization was performed while maintaining a monatomically increasing Mach number over the suction side and ensuring a small uncovered turning angle. In order to perform an accurate aerothermal optimization within the F100 engine model, a slight

variation to the above sequence of the model optimization was implemented. Rather than run the NPSS model first to find the inlet properties to the HPT, the offspring of the HPTs were found first using the genetic algorithm optimizer. The theoretical turbine inlet temperature was then calculated according to Eq. 2.6 and the NPSS model was then run with this new Tt4 as the burner exit condition. The same process was applied to the LPTs when the model was run with an interstage turbine burner. This process ensured that the new turbine inlet temperatures that the offspring turbines allowed for were incorporated into the NPSS model.

4.3.2 F100 Hot Section Optimization Results

An aerothermal optimization of the high and low pressure turbine blade geometries was performed on the F100 baseline model and the F100 model with an interstage turbine burner at sea level static conditions. Thrust and TSFC for the engine comprised of the objective function. In addition, to ensure an optimal turbine blade design, constraints were implemented to allow for a monatomically increasing Mach number on the suction side and a small uncovered turning angle. The performance of the optimized F100 with an interstage turbine burner was compared to the performance of the optimized F100 model without an ITB. In additional, the performance of both optimized models was compared to the performance of the respective model with the turbines optimized individually outside of the model as in Chapter 3.

4.3.2.1 F100 Baseline Model Optimization

An aerothermal optimization for the high and low pressure turbine blades was performed for the baseline F100 model at sea level static conditions. Optimization time for the model more than doubled from that of the stage optimization due to the addition of an additional stage optimization (LPT) within the model as well as the model computation time for each offspring.

The CFD solutions for each turbine offspring was still performed in parallel, however, due to limitations with the computer cluster used for this research, the model runs in NPSS for each

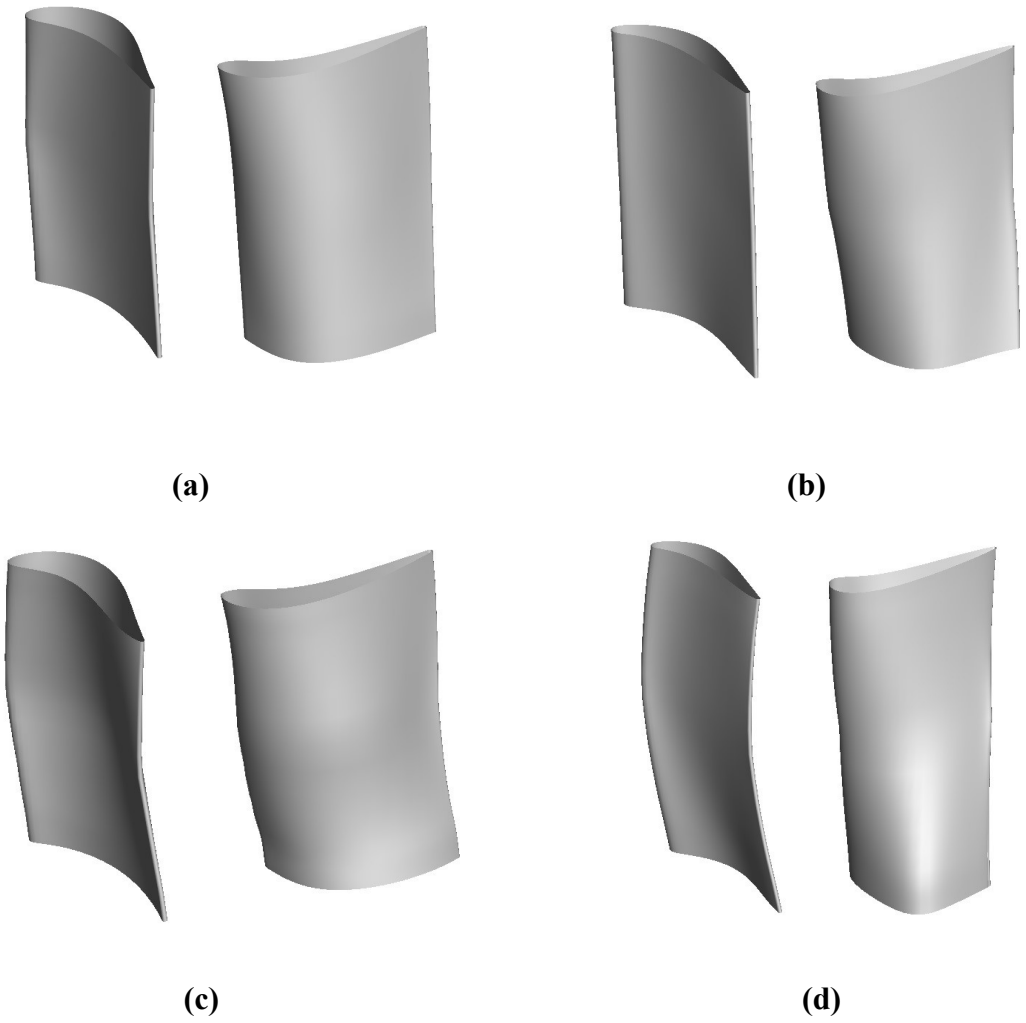

Figure 4.8. (a) Initial high pressure turbine, (b) initial low pressure turbine, (c) optimized high pressure turbine, (d) optimized low pressure turbine

offspring were performed in serial rather than parallel, thus increasing computation time by approximately 80%. Despite this, computation time was still reasonable with convergence occurring within 100 generation in 5.5 days. The initial and final stage solution geometries for the HPT and LPT are shown in Fig. 4.8 with thrust and TSFC results shown in Table 4.5. Results

indicate a 1.4% increase in thrust with a 1.5% decrease in TSFC. Pressure and Mach number contours at the midspan for the high and low pressure turbine stages are shown in Figs. 4.9 and 4.10 respectively.

Table 4.5. F100 Hot Section Optimization Results

	Model	Thrust (lbf)	TSFC (lbm/hr lbf)
F100 Baseline	Initial	28,505.1	2.054
	Optimized Model	28,909.0	2.023

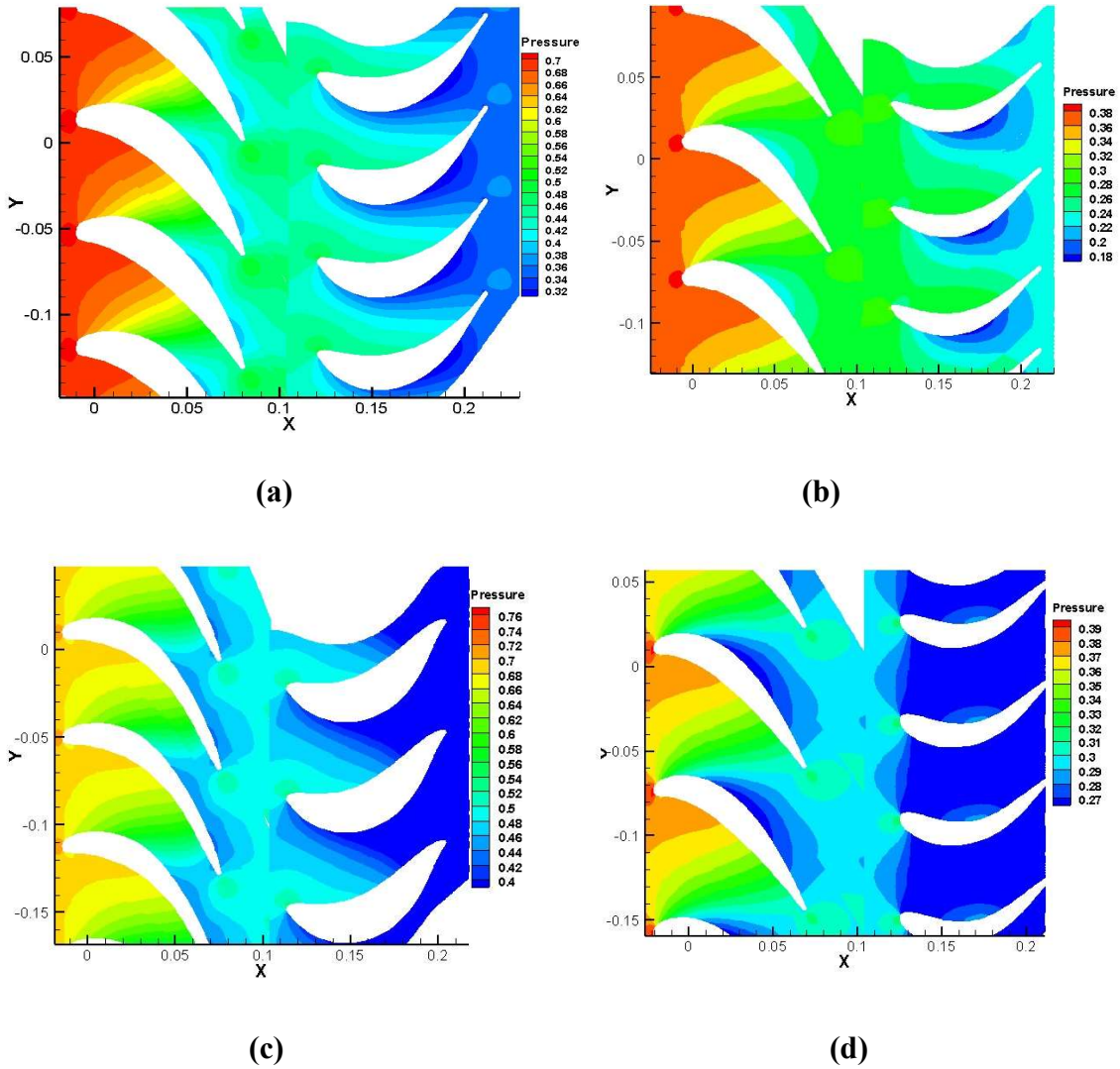

Figure 4.9. Pressure contours at midspan (a) Initial high pressure turbine, (b) initial low pressure turbine, (c) optimized high pressure turbine, (d) optimized low pressure turbine

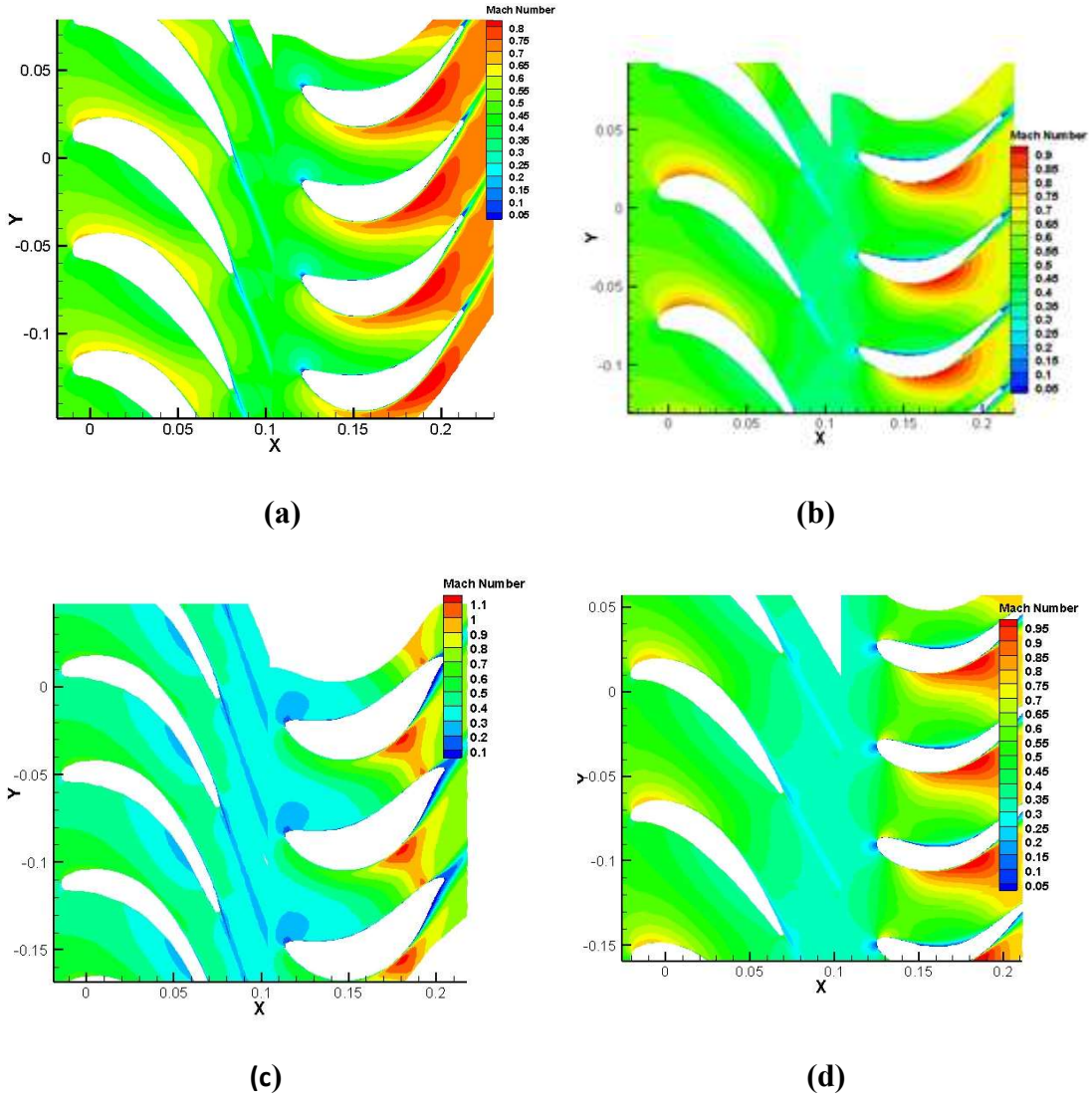

Figure 4.10. Mach number contours at midspan (a) Initial high pressure turbine, (b) initial low pressure turbine, (c) optimized high pressure turbine, (d) optimized low pressure turbine

4.3.2.2 F100 Model with Interstage Turbine Burner Optimization

An aerothermal optimization for the high and low pressure turbine blades was performed for the F100 model with an interstage turbine burner at sea level static conditions. Results indicate a 5.2% increase in thrust from the baseline F100 and a 3.8% increase in thrust from the optimized F100 baseline model. Additionally, the optimization of the F100 with an ITB resulted in a 8.7% decrease in TSFC from the baseline F100 and a 7.3% decrease in TSFC from the optimized F100 baseline model. Results are tabulated in Table 4.6.

Table 4.6 F100 with ITB Hot Section Optimization Results

	Model	Thrust (lbf)	TSFC (lbm/hr lbf)
F100 Baseline	Initial	28,505.1	2.054
	Optimized Model	28,909.0	2.023
F100 with ITB	Optimized Model	29,993.1	1.876

Results indicate the optimized F100 model with an interstage turbine burner outperformed that of the optimized baseline F100 model without an interstage turbine burner. The optimized stage geometry as compared to the initial geometry is shown in Fig. 4.11 with the pressure and Mach number contours of the stage at the midspan shown in Figs. 4.12 and 4.13 respectively.

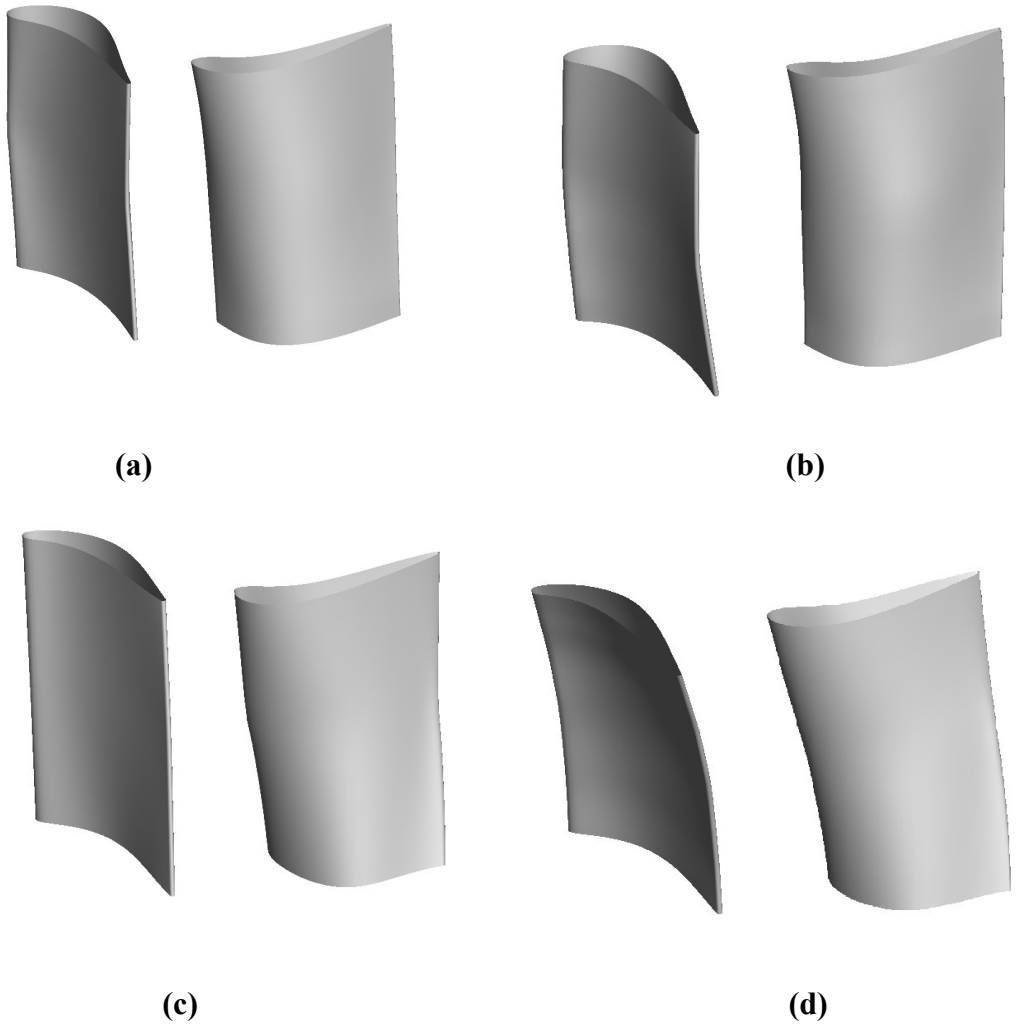

Figure 4.11. (a) Initial high pressure turbine, (b) initial low pressure turbine, (c) optimized high pressure turbine, (d) optimized low pressure turbine

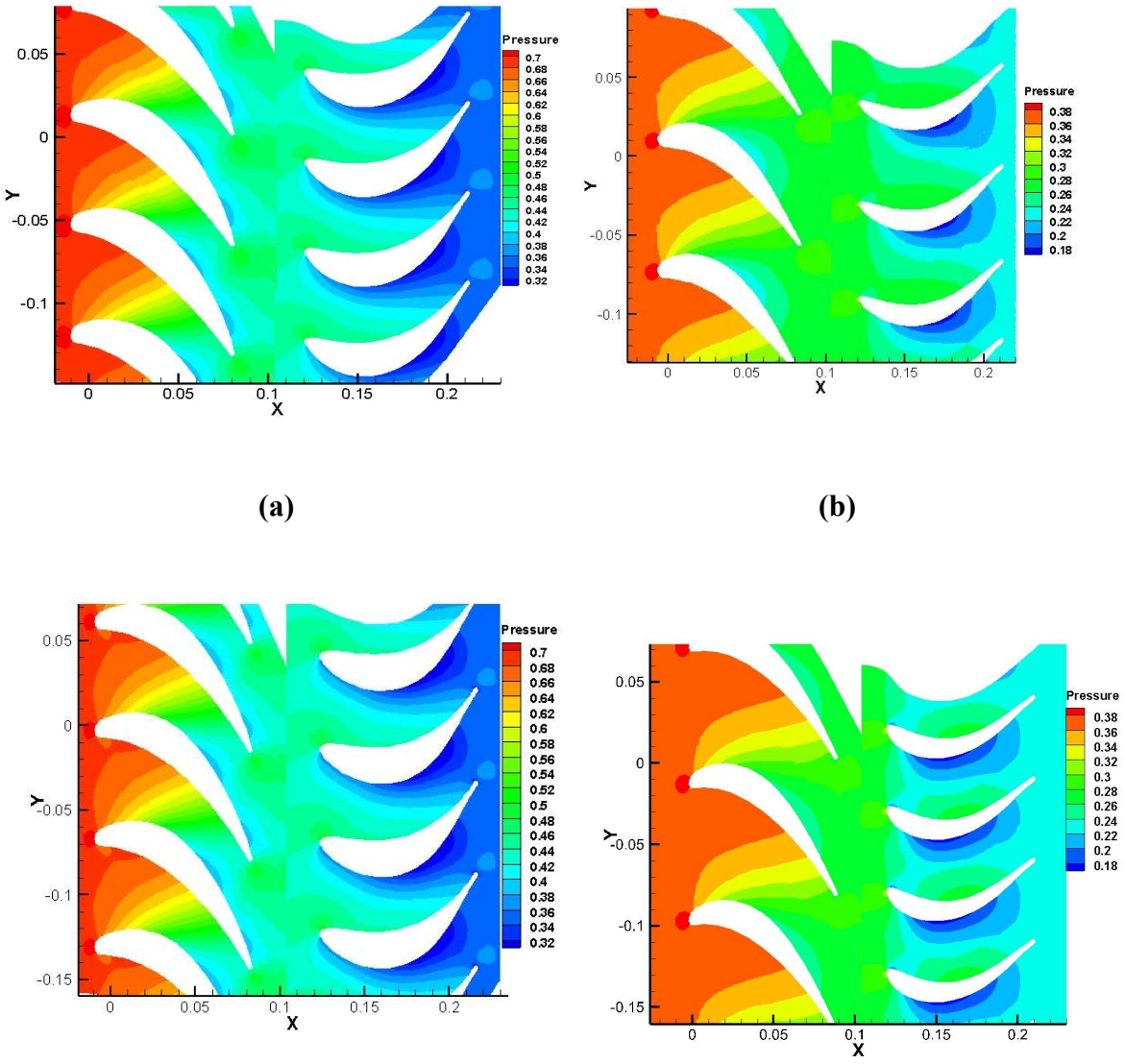

Figure 4.12. Pressure contours at midspan (a) Initial high pressure turbine, (b) initial low pressure turbine, (c) optimized high pressure turbine, (d) optimized low pressure turbine

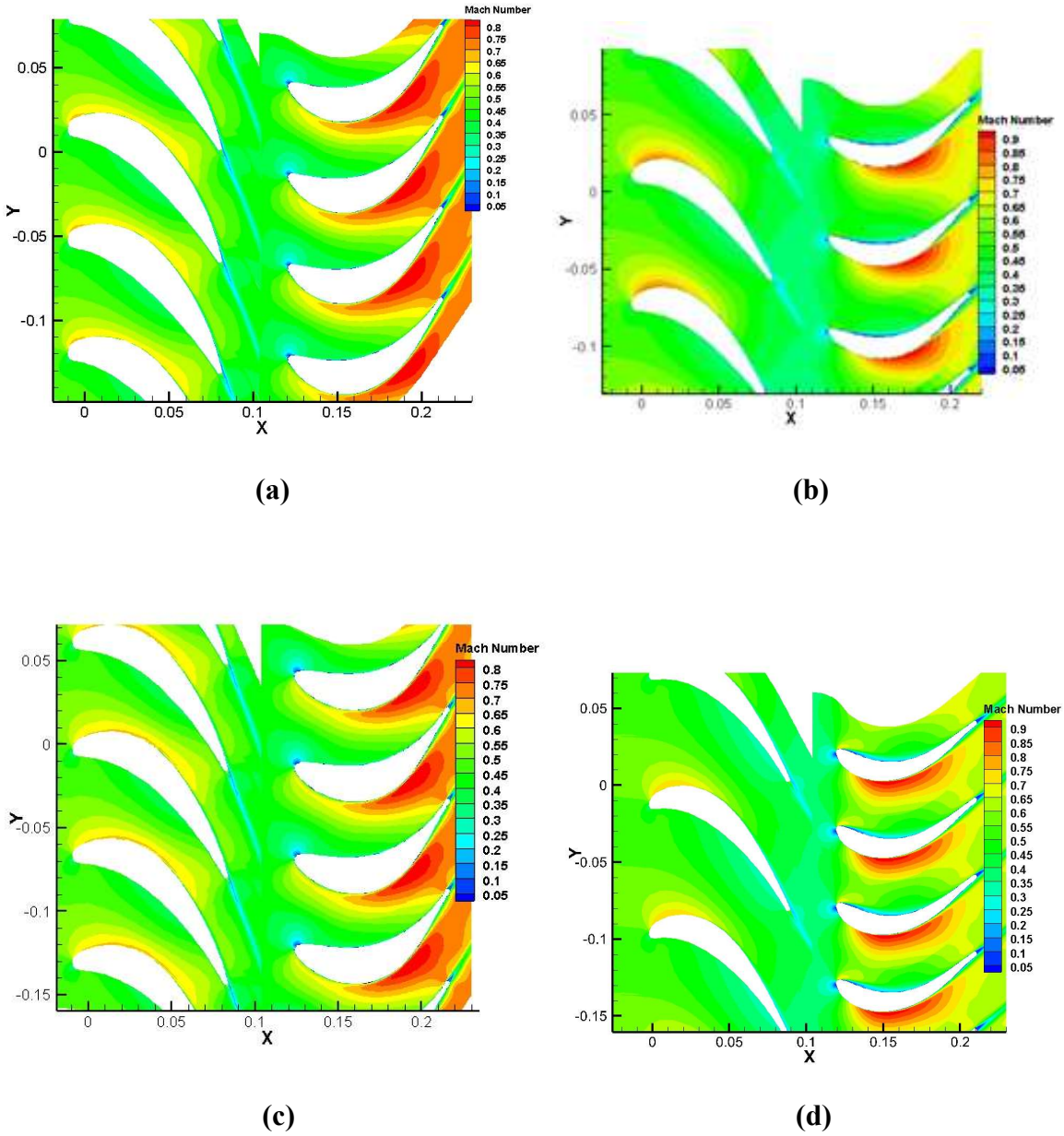

Figure 4.13. Mach number contours at midspan (a) Initial high pressure turbine, (b) initial low pressure turbine, (c) optimized high pressure turbine, (d) optimized low pressure turbine

4.3.2.3 Optimized Turbine Results within F100 Models

The vast majority of turbine optimization research aims to optimize individual turbine blades or stages for a specific objective function with the assumption that inserting this turbine into an engine will result in the optimal turbine performance for the engine and thus an optimal improvement in engine performance. This part of the research compares the performance of the engine of the optimized engine models to the performance of the engine of the optimized turbines within the engine models.

The high and low pressure turbines were first optimized individually and then placed in the F100 Baseline engine model. The resulting thrust and TSFC were then compared to the thrust and TSFC of the optimized F100 Baseline engine model. These results are shown in Table 4.7.

Table 4.7. Engine performance comparison of model with optimized turbines and model optimized with turbines

	Model	Thrust (lbf)	TSFC (lbm/hr lbf)
F100 Baseline	Initial	28,505.1	2.054
	Optimized Model	28,909.0	2.023
	Optimized Turbines	26,583.0	1.795

As show in Table 4.7, the model performance with the optimized turbines resulted in a 6.7% decrease in thrust and a 12.6% decrease in TSFC. While the considerable decrease in TSFC is desirable, the decrease in the thrust of the engine is not a desirable optimization objective. The reason for the aforementioned results is due to the afterburner performance. The flow properties entering the afterburner forced the component to converge at a lower temperature than specified, resulting in a lower TSFC and a thus a low thrust produced by the engine.

It is desirable to optimize the high and low pressure turbines individually to save approximately 89% computation time in this particular computational setup, or 3% computation time if the entire engine model optimization is performed in parallel. However, results indicate the model optimization provides superior engine performance results to the individual turbine stage optimizations as these optimizations do not account for impacts to other engine components as a result of the optimized turbine stage. The results presented in this section indicate that the high and low pressure turbines should be optimized within the engine model for optimal engine performance results. An interstage turbine burner allows for an increased thrust and TSFC for the engine over that of the baseline. Only one trial was performed for the F100 model optimization as the optimizer has proven robust through the individual turbine stage optimizations as shown in the previous section. In addition, the objective of proving the effectiveness of the optimization of the turbine stages within the model has been shown. Redundant runs will be performed for the turboramjet hot section optimization in the next section as this is the primary objective for this work.

Chapter 5

Turbine Based Combined Cycle Model and Optimization

The heart of this research involves modeling a turboramjet engine with an interstage turbine burner and optimizing the high and low pressure turbine stages to increase the maximum Mach number of the turbine cycle and thus increase efficiency of the entire engine TBCC. An aerothermal optimization is performed for the HPT and LPT of the turboramjet with and without an ITB. Three different design points are optimized and an analysis of the optimizations are performed. It is expected that the turboramjet optimization with the ITB will yield a higher performing engine than that of the turboramjet without the ITB.

5.1 Turboramjet Model

Since the retirement of the SR-71 Blackbird in 1990, there has not been another operational turboramjet engine in military or civil aircraft inventory. In order to fill the void left by the SR-71 and meet the need for an unmanned supersonic reconnaissance vehicle, the design and development of the SR-72 turbine based combined cycle engine with an operating envelope of 0-6 Mach is currently underway. Originally envisioned as a completely new engine design, these efforts were scrapped in favor of utilizing a COTS turbojet to take the aircraft up to Mach 3, with a hypersonic ramjet/scramjet to power the vehicle up to Mach 6.[46] As this is the current design as of this writing, it was decided to model the turboramjet for this research utilizing an F100 engine for the turbine cycle augmented with a ramjet cycle at the transition point. In addition, since the F100 engine is easily validated in NPSS, augmenting this engine with a ramjet

is a satisfactory way to validate the turboramjet used for this research as there is currently no publicly available data for the SR-72 TBCC currently in design.

The turboramjet modeled for this research is shown in Fig. 5.1. The F100 turbofan parameters are equivalent to the ones validated in the previous chapter. A bypass has been added to the model in which the ramjet combustion occurs. This model is a representation of a

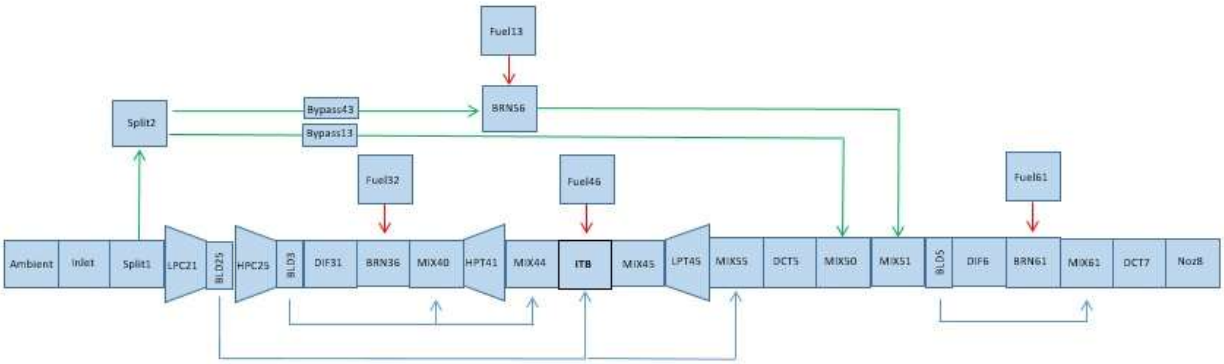

Figure 5.1. Turboramjet Model

turboramjet designed from a COTS F100 turbofan. With no existing validation data for a TBCC with a F100 turbofan engine, it is impossible to completely validate the NPSS model. However, as the F100 turbofan has been validated against publicly available data, a reasonable assumption can be made that augmenting the turbofan with a ramjet results in a realistic turbine based combined cycle engine for the purposes of optimizing the hot section in the research.

5.2 TBCC Optimization Cases

The scope of this research limits turbine based combined cycle optimization to the hot section of the engine at three different design cases. It was determined that three design cases are sufficient to prove the value of optimizing the high and low pressure turbine stages within the model versus independent of the model. The effect of optimizing the hot section with the

interstage turbine burner is also determined with the optimization cases. The aerothermal optimization cases run for the turboramjet hot section is listed in Table 5.1.

Table 5.1 TBCC Optimization Cases

	Mach Number	Altitude	ITB
Case 1	3.0	40,000 ft	no
Case 2	3.0	40,000 ft	yes
Case 3	3.0	60,000 ft	yes
Case 4	3.0	80,000 ft	yes

5.2.1 Turboramjet Optimization Case 1

The first aerothermal optimization of the turboramjet hot section was run at a Mach number of 3.0 and cruise altitude of 40,000 ft. This first optimization case was run without an interstage turbine burner to provide comparison to the subsequent optimization which is run at the same optimization cruise condition with an ITB. The objective function of the optimization were TSFC and thrust. A converged solution was achieved within 6 days. The optimized turboramjet model solution was then compared with the solution of the independently optimized high and low pressure turbines run in the turboramjet. A comparison of these results is shown in Table 5.2.

Table 5.2 Turboramjet Optimization Results M=3.0, Alt=40,000 ft, no ITB

	Model	Thrust (lbf)	TSFC (lbm/hr lbf)
Turboramjet Baseline	Initial	15,294.6	3.231
	Optimized Model	15,685.8	3.099
	Optimized Turbines	15,598.2	3.226

The aerothermal hot section optimization improved thrust by 2.6% and TSFC by 4.1%. When the independently optimized high and low pressure turbines were input into the model, thrust increased by 2.0% and TSFC improved by 0.15%. Although the individual isentropic efficiency of both the HPT and LPT stages were slightly greater for the individually optimized turbine stages than the stages optimized within the model, the stages optimized within the model still provided superior results over that of the individually optimized turbines inserted into the model. The main reason behind this is the thermal part of the optimization. As the turbine stage is optimized within the model, the turbine inlet temperature changes with the changing turbine blade shape. This allows for the model to account for the increase in allowable turbine inlet temperature and output the relevant TSFC and thrust. When optimizing the stage independent of the model, the final blade shape will reflect the highest turbine inlet temperature allowable, which may not necessarily yield the optimal TSFC and thrust when the stage in input into the model. For the model optimization, a final turbine inlet temperature of 3099R yielded the optimal results, a slight decrease from the 3160R initial value. The individually optimized turbines yielded a final turbine inlet temperature of 3334R, which increased the thrust from the initial model, but failed to decrease the TSFC. The initial and final stage model optimizations are shown in Fig. 5.1 with the pressure and Mach number midspan contours shown in Figs. 5.2 and 5.3 respectively.

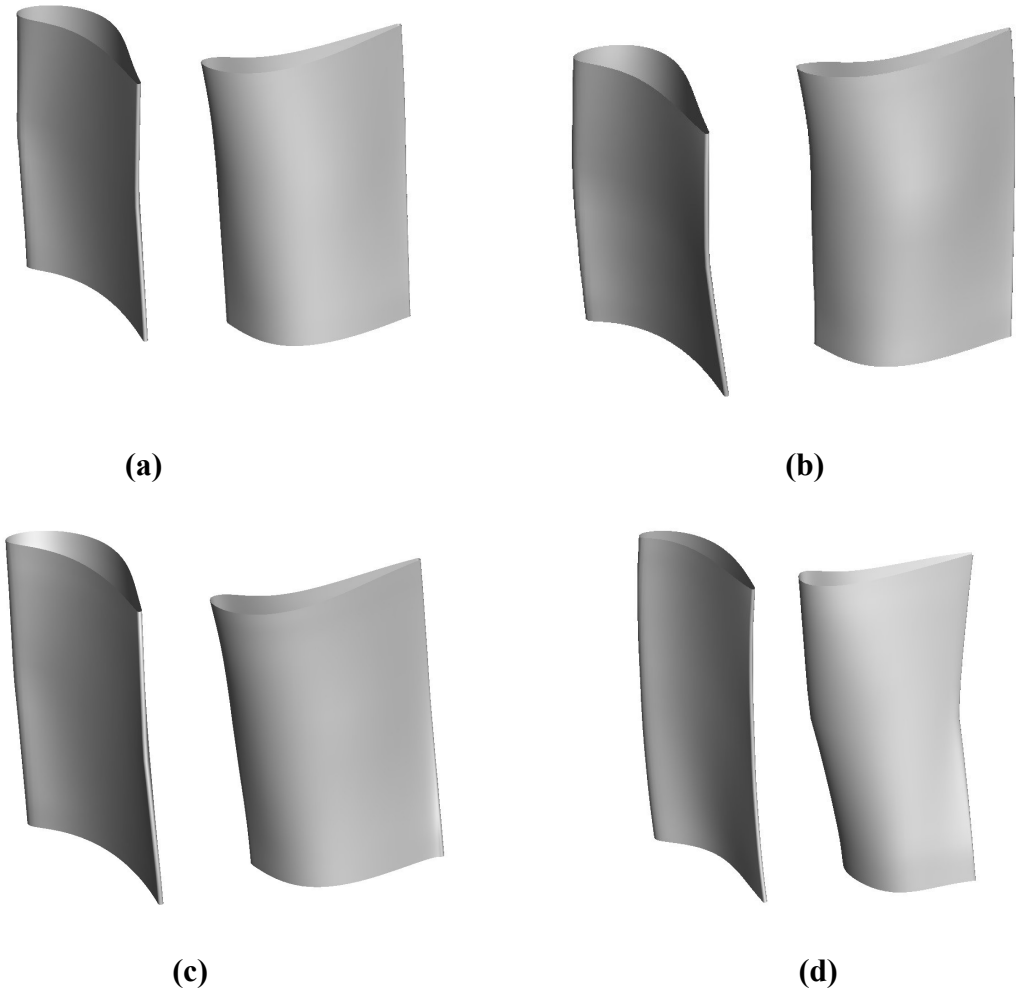

Figure 5.2. (a) Initial high pressure turbine, (b) initial low pressure turbine, (c) optimized high pressure turbine, (d) optimized low pressure turbine

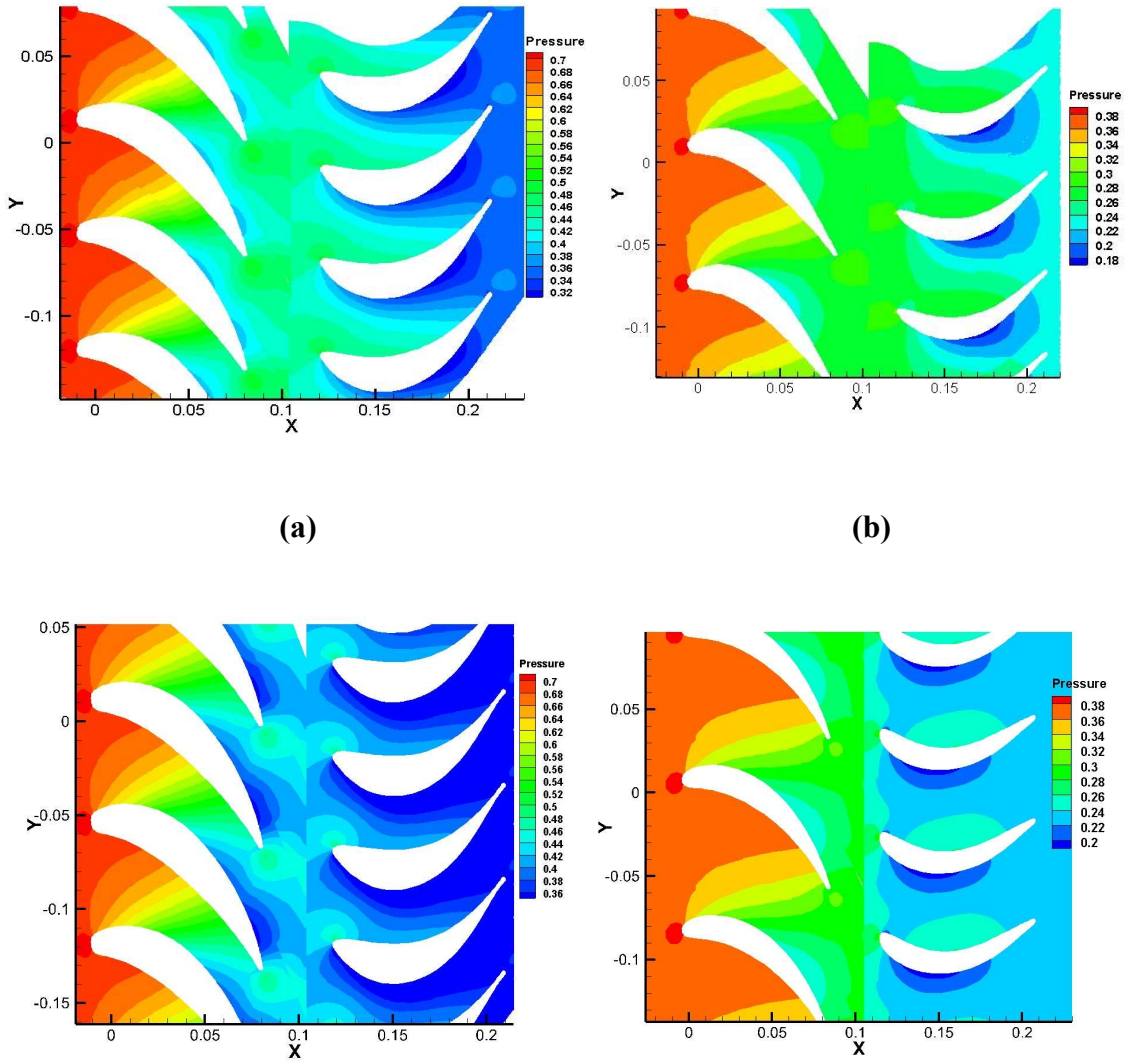

Figure 5.3. Pressure contours at midspan (a) Initial high pressure turbine, (b) initial low pressure turbine, (c) optimized high pressure turbine, (d) optimized low pressure turbine

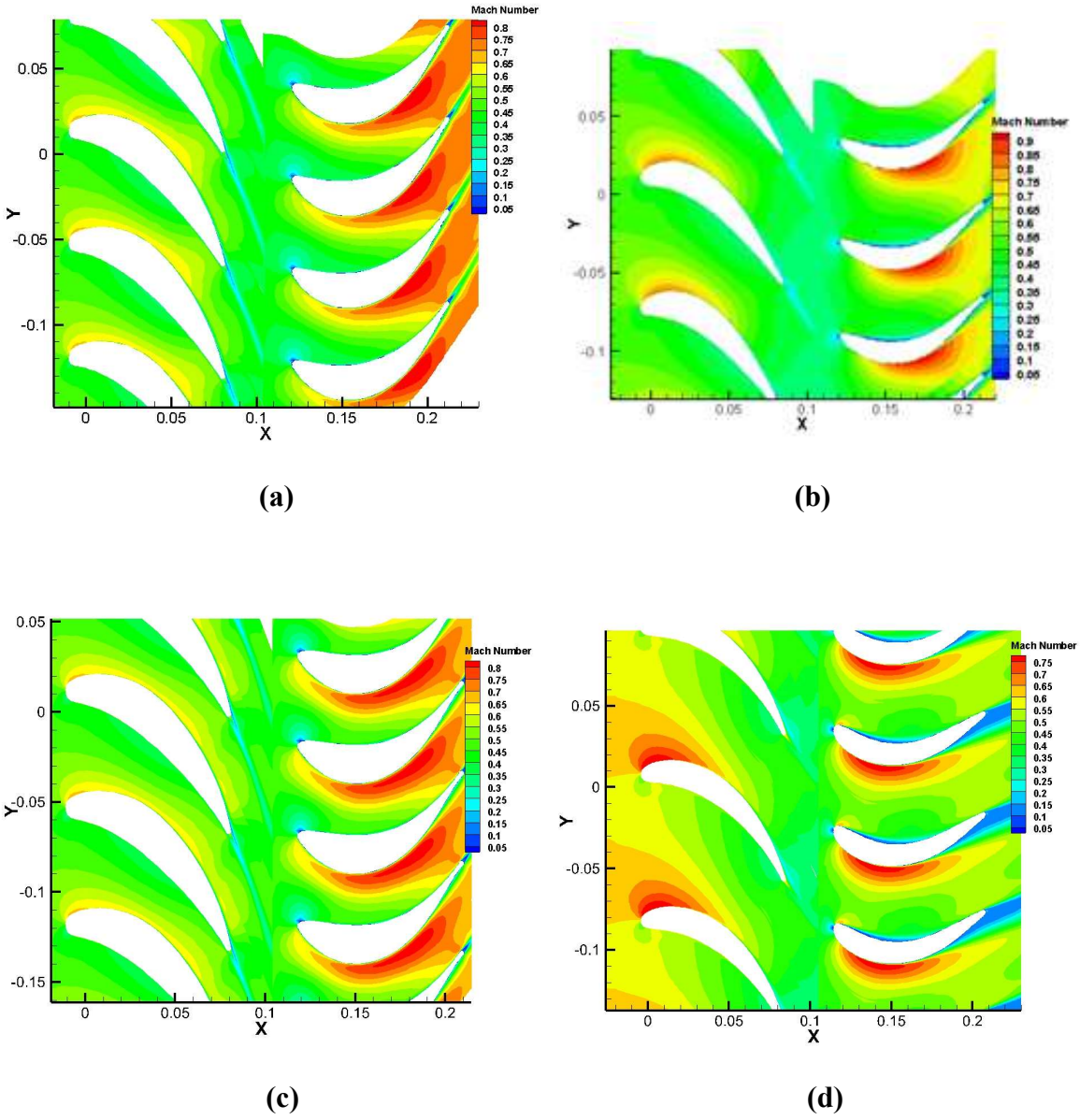

Figure 5.4. Mach number contours at midspan (a) Initial high pressure turbine, (b) initial low pressure turbine, (c) optimized high pressure turbine, (d) optimized low pressure turbine

5.2.2 Turboramjet Optimization Case 2

The second aerothermal optimization of the turboramjet hot section was run at the same cruise condition as the previous case, but with an interstage turbine burner included in the model. The objective function of thrust and TSFC was also chosen for this test case. Table 5.3 shows the results of test case 2 as compared to the initial turboramjet and the optimized turboramjet from test case 1.

Table 5.3 Turboramjet Optimization Results M=3.0, Alt=40,000 ft, with ITB

	Model	Thrust (lbf)	TSFC (lbm/hr lbf)
Turboramjet Baseline	Initial	15,294.6	3.231
	Optimized Model	15,685.8	3.099
Turboramjet with ITB	Optimized Model	16,201.8	2.989
	Optimized Turbines	16,412.7	3.066

Optimization results of the turboramjet with the interstage turbine burner show a 5.9% increase in thrust over the initial baseline turboramjet and a 3.3% increase in thrust over the optimized turboramjet without an ITB. TSFC decreased by 7.5% over the baseline model and 3.5% from the optimized model without an ITB. When the individually optimized high and low pressure turbine stage were placed in the turboramjet with the ITB, they resulted in a 1.3% increase in thrust, but a 2.6% higher TSFC than the stages optimized within the model. Results are consistent with those of the F100 optimization in that the interstage turbine burner provided for superior results in thrust and TSFC. In addition, the stage optimization within the model provided for improved results over the individually optimized high and low pressure stages. As in the previous cases, it is suspected that the turbine inlet temperature contributed to the superior results by the model optimization. In this case, the turbine inlet temperatures exiting both the main burner and the interstage turbine burner were varied. The Tt4 for the main burner for the

model optimization was 3136 R and 3216 R for the ITB. The individually optimized stages provided for a Tt4 of 3334 R and 3236 R for the main burner and ITB respectively. These higher turbine inlet temperatures as compared to the model optimization contributed to the increased thrust for the model, but also to the decreased TSFC of the model. The initial and final stage model optimizations are shown in Fig. 5.4 with the pressure and Mach number midspan contours shown in Figs. 5.5 and 5.6 respectively.

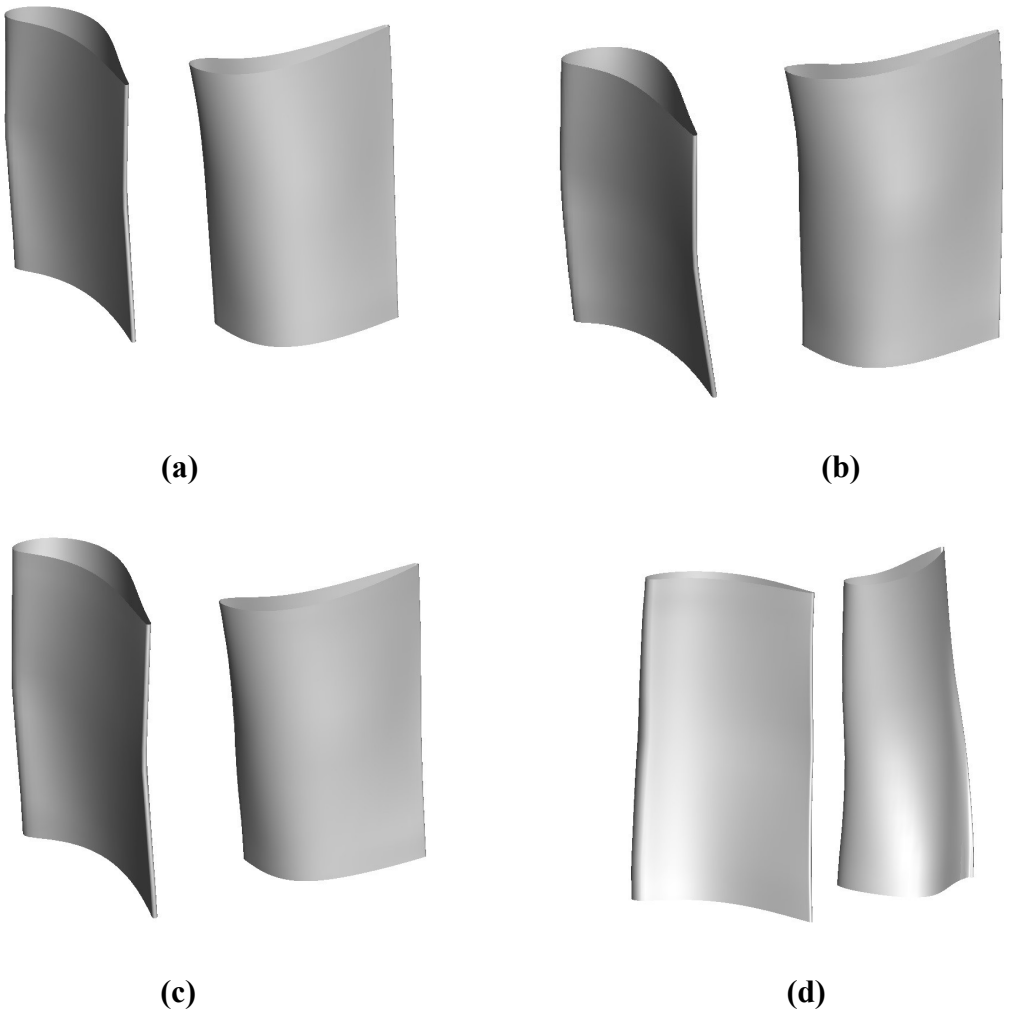

Figure 5.5. (a) Initial high pressure turbine, (b) initial low pressure turbine, (c) optimized high pressure turbine, (d) optimized low pressure turbine

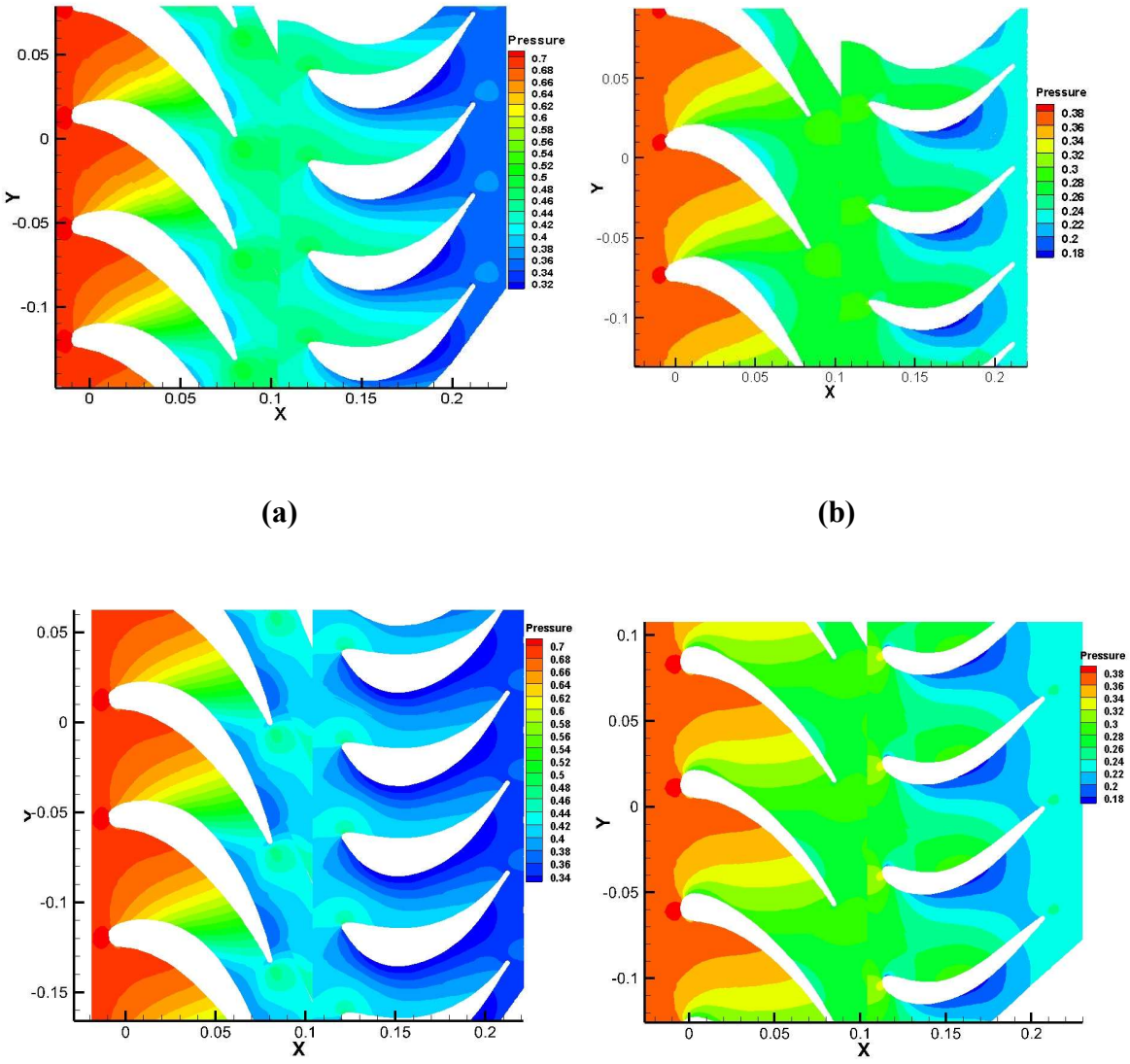

Figure 5.6. Pressure contours at midspan (a) Initial high pressure turbine, (b) initial low pressure turbine, (c) optimized high pressure turbine, (d) optimized low pressure turbine

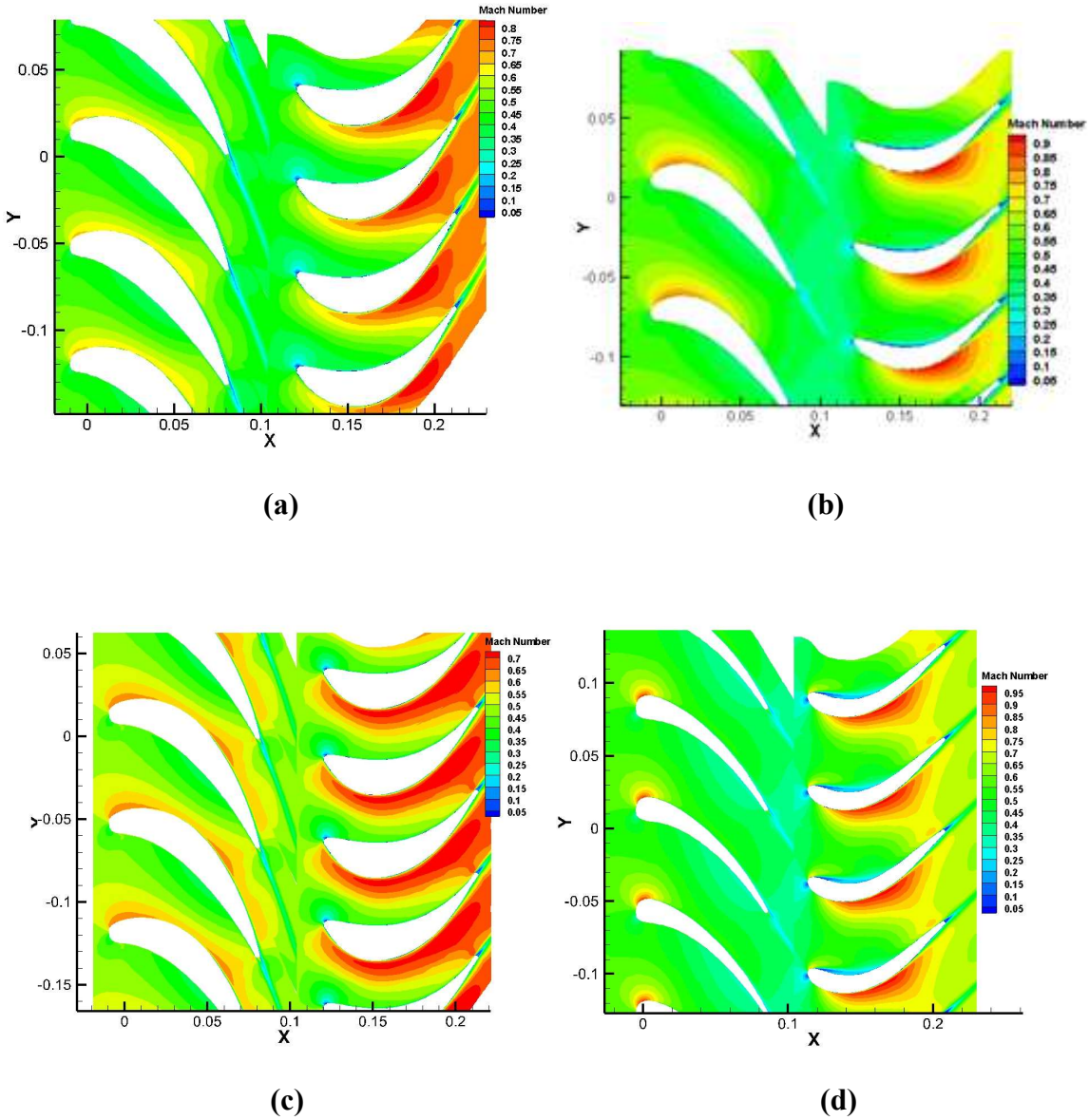

Figure 5.7. Mach number contours at midspan (a) Initial high pressure turbine, (b) initial low pressure turbine, (c) optimized high pressure turbine, (d) optimized low pressure turbine

5.2.3 Turboramjet Optimization Case 3

The third aerothermal optimization of the turboramjet hot section included the ITB in the model as in the previous case, but was run at a cruise condition of a Mach number of 3.0 and altitude of 60,000 feet. The objective function of thrust and TSFC was also chosen for this test case. Table 5.4 shows the optimization results of the turboramjet as compared to the baseline model run at the same cruise condition.

Table 5.4 Turboramjet Optimization Results M=3.0, Alt=60,000 ft, with ITB

	Model	Thrust (lbf)	TSFC (lbm/lbf hr)
Turboramjet with ITB	Initial	16,222.70	3.129
	Optimized Model	16,814.70	2.883
	Optimized Turbines	16,838.50	3.078

The aerothermal optimization increased the thrust 3.6% over the initial model and decreased TSFC 7.9%. When placing the independently optimized turbines into the model, thrust increased 3.8% over the baseline model and TSFC decreased 1.6%. These results are similar to the optimization at 40,000 ft in that the model optimization provided overall better optimization results than the independently optimized turbines. Also, both optimizations provided a signification TSFC reduction as compared to the baseline model. The turbine inlet temperatures also followed a pattern similar to that in the previous optimization case. The turbine inlet temperature for the main burner was 3092 R and 3197 R for the ITB. This is significantly less than the turbine inlet temperatures of 3334 R and 3236 R for the main burner and ITB respectively of the independently optimized turbines, and is the reason why there was not a significant reduction in TSFC as a result of the optimization. The initial and final stage model

optimizations are shown in Fig. 5.8 with the pressure and Mach number midspan contours shown in Figs. 5.9 and 5.10 respectively.

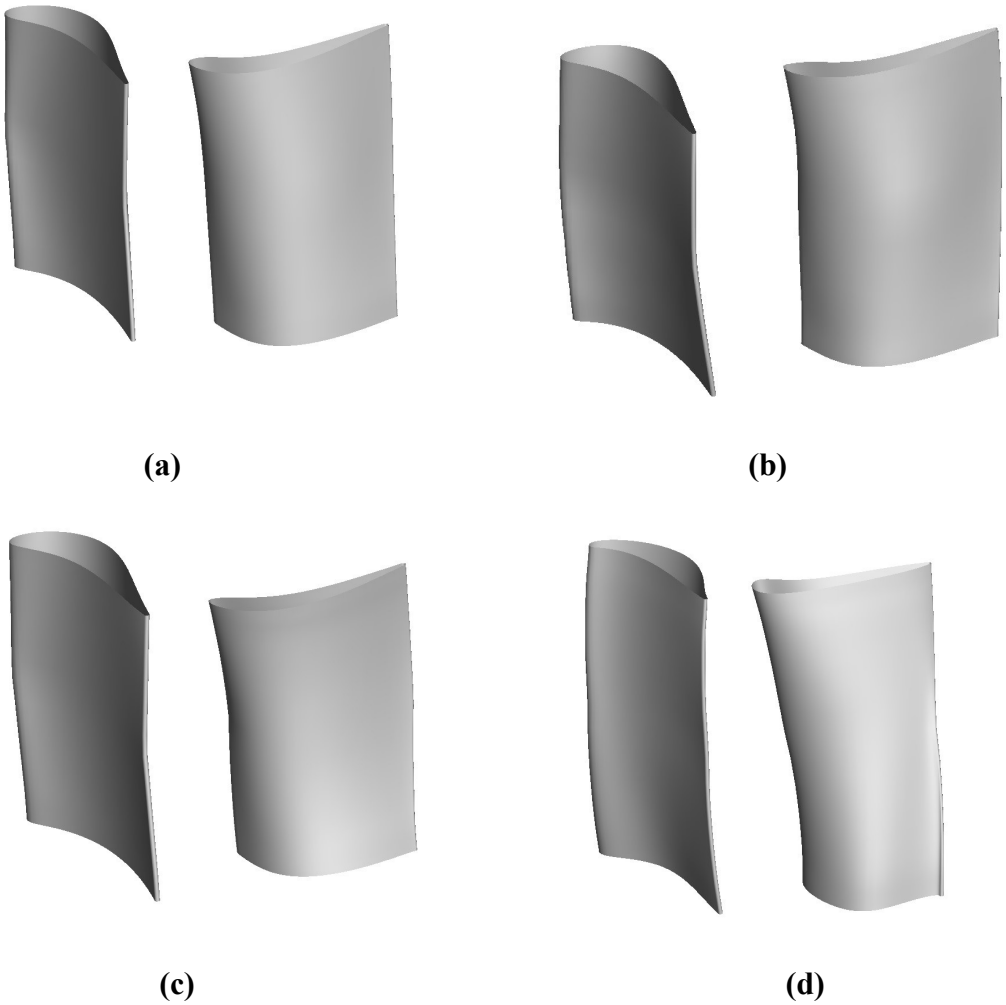

Figure 5.8. (a) Initial high pressure turbine, (b) initial low pressure turbine, (c) optimized high pressure turbine, (d) optimized low pressure turbine

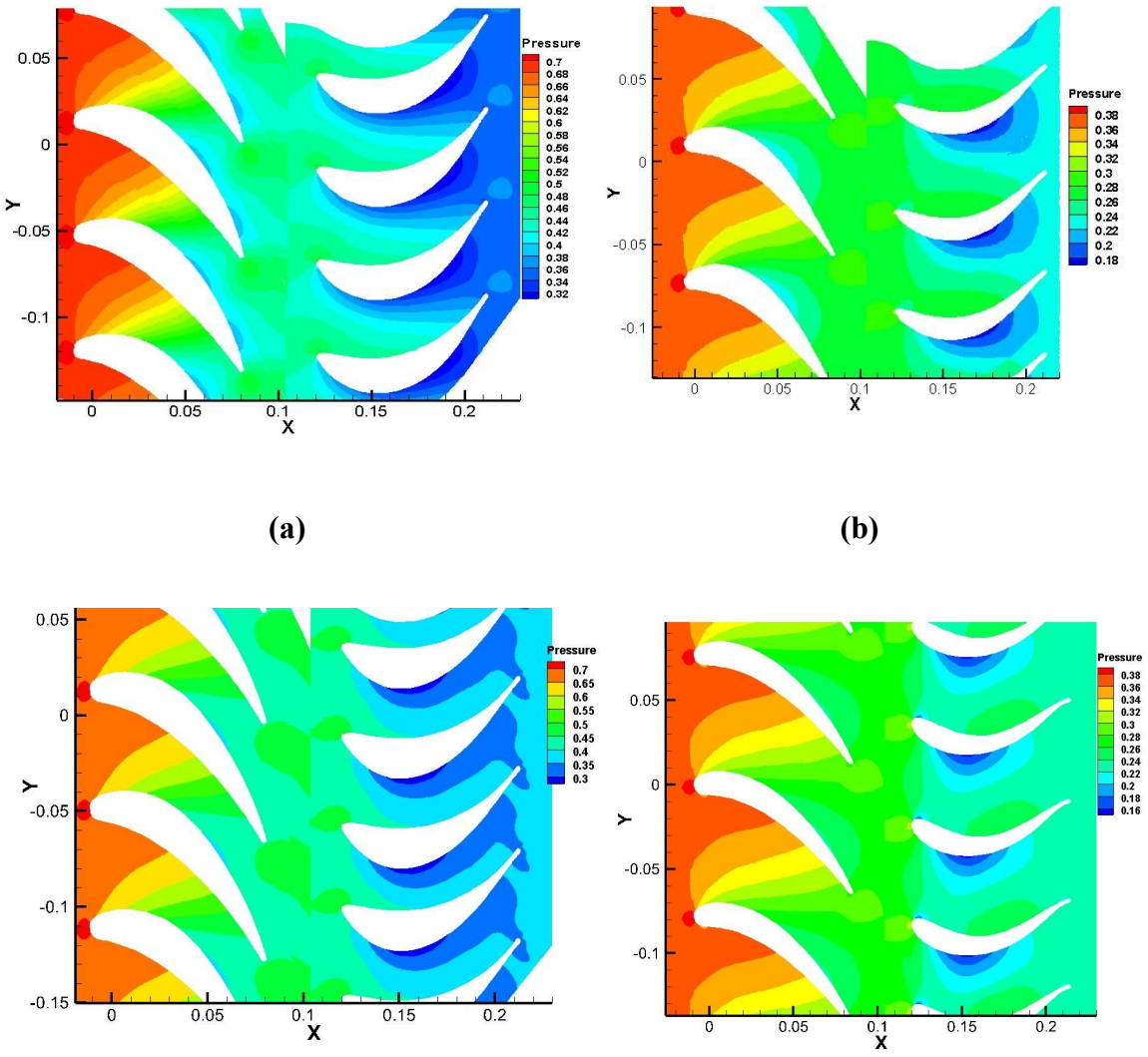

Figure 5.9. Pressure contours at midspan (a) Initial high pressure turbine, (b) initial low pressure turbine, (c) optimized high pressure turbine, (d) optimized low pressure turbine

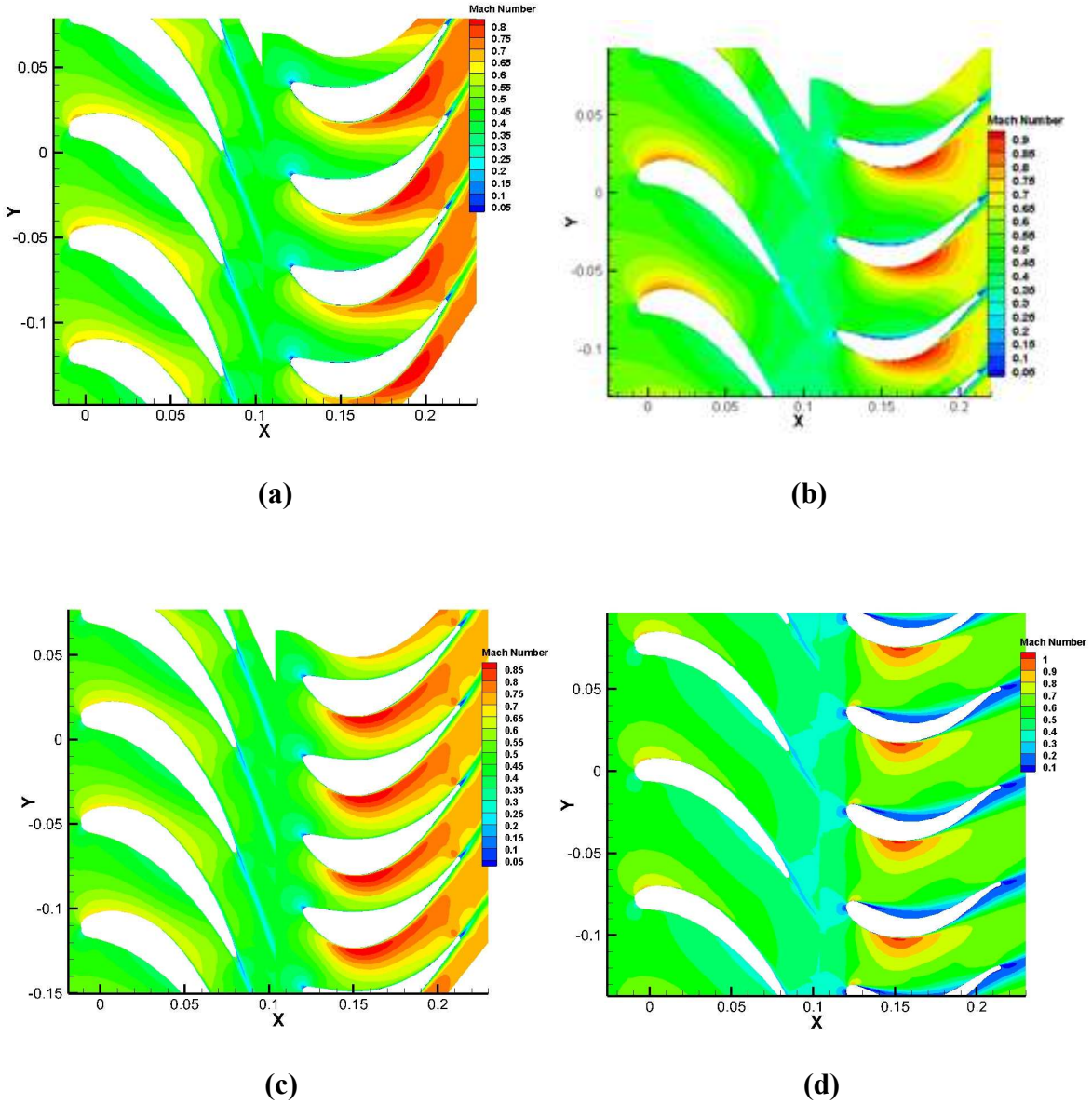

Figure 5.10. Mach number contours at midspan (a) Initial high pressure turbine, (b) initial low pressure turbine, (c) optimized high pressure turbine, (d) optimized low pressure turbine

5.2.4 Turboramjet Optimization Case 4

The fourth aerothermal optimization of the turboramjet hot section included the ITB in the model as in the previous case, but was run at a cruise condition of a Mach number of 3.0 and altitude of 80,000 feet. The objective function of thrust and TSFC was also chosen for this test case. Table 5.5 shows the optimization results of the turboramjet as compared to the baseline model run at the same cruise condition.

Table 5.5 Turboramjet Optimization Results M=3.0, Alt=80,000 ft, with ITB

	Model	Thrust (lbf)	TSFC (lbm/lbf hr)
Turboramjet with ITB	Initial	14,931.7	3.592
	Optimized Model	15,218.8	3.382
	Optimized Turbines	14,974.6	3.678

Consistent with the previous three test cases, the model optimization resulted in improvement in the thrust and TSFC, a 2.1% increase in thrust and 5.8% decrease in TSFC. The turboramjet performance with the independently optimized turbines yielded a 0.3% nominal gain in thrust and actually caused the TSFC to increase by 2.4%. As in the previous three cases, the turbine inlet temperature for the independently optimized turbines of 3334 R and 3236 R for the main burner and ITB respectively differed considerably from that of the turbines optimized within the model which were 3115 R and 3279 R for the main burner and ITB respectively. The initial and final stage model optimizations are shown in Fig. 5.11 with the pressure and Mach number midspan contours shown in Figs. 5.12 and 5.13 respectively.

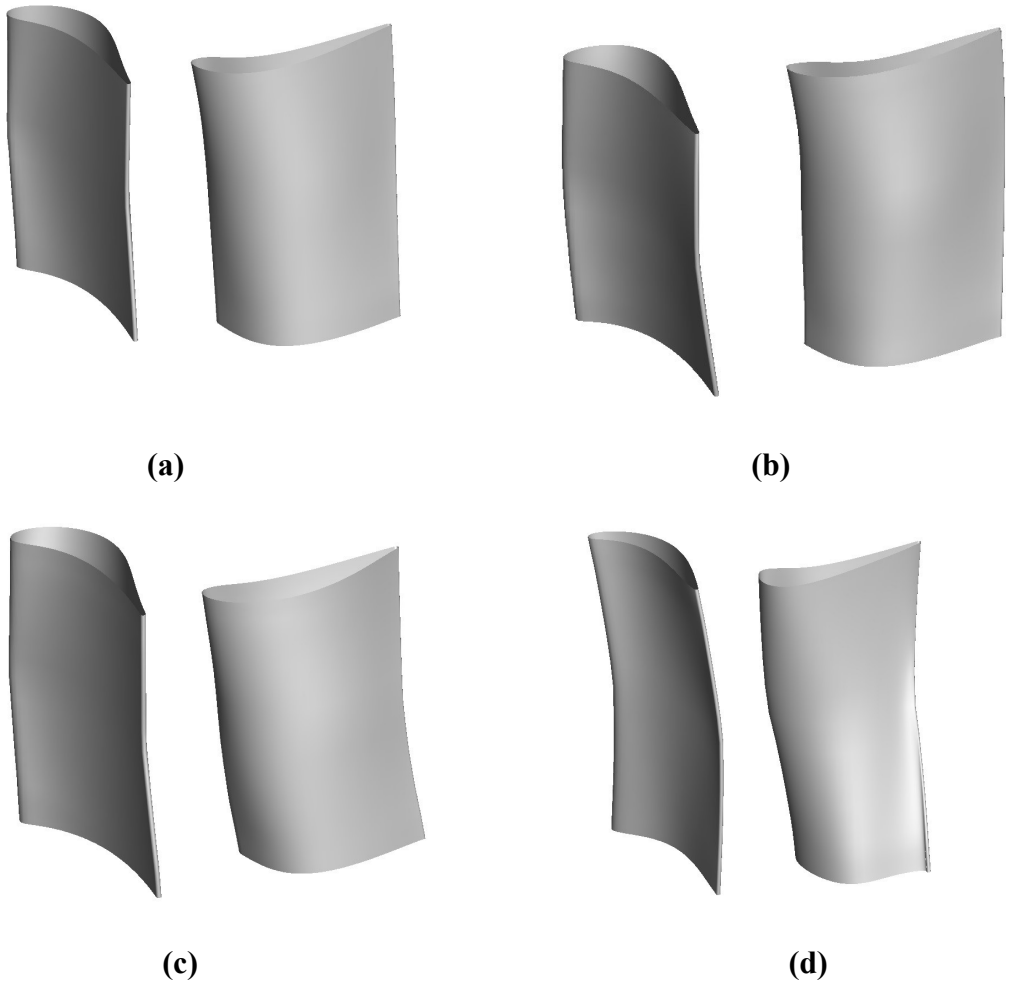

Figure 5.11. (a) Initial high pressure turbine, (b) initial low pressure turbine, (c) optimized high pressure turbine, (d) optimized low pressure turbine

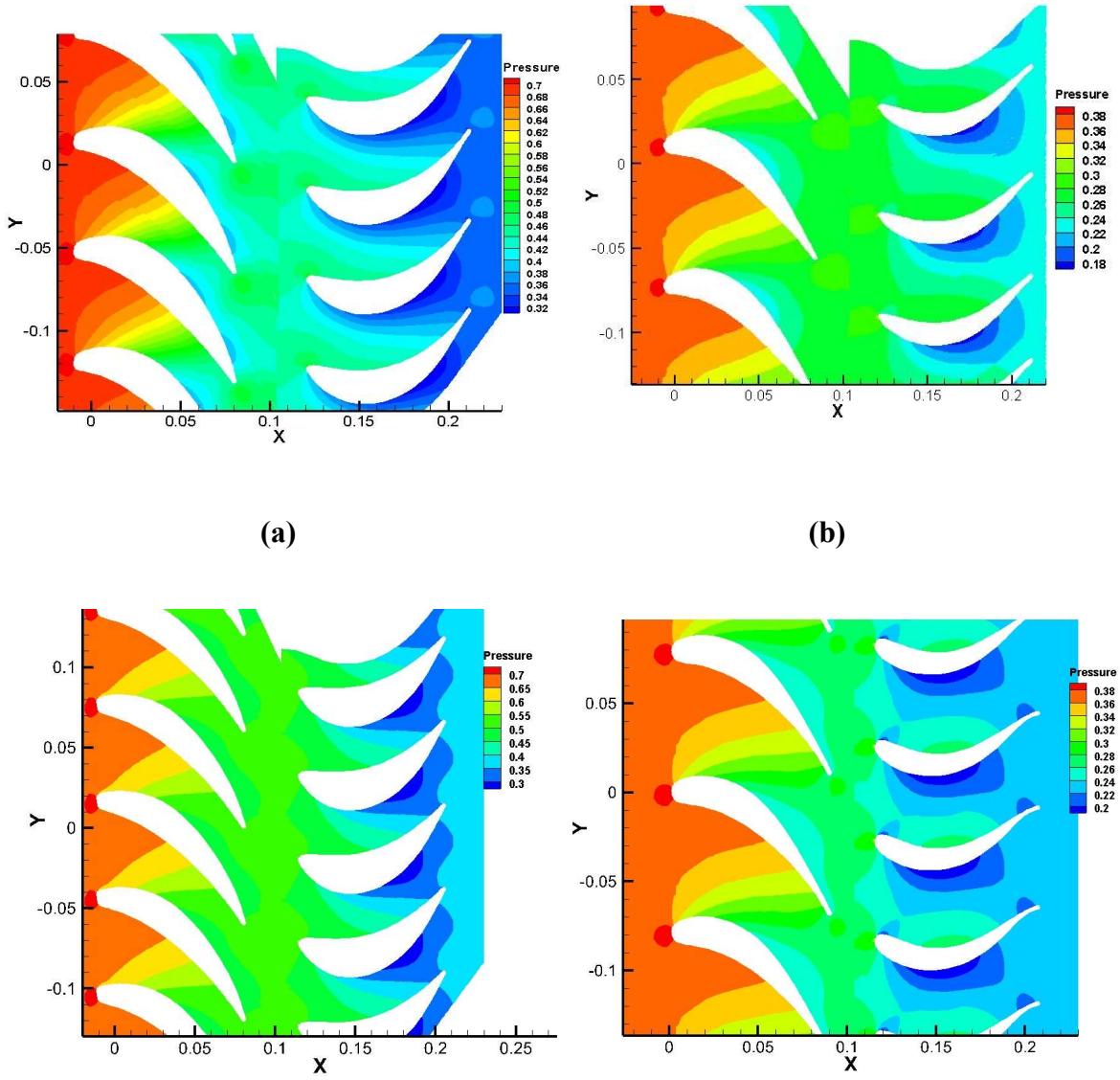

Figure 5.12. Pressure contours at midspan (a) Initial high pressure turbine, (b) initial low pressure turbine, (c) optimized high pressure turbine, (d) optimized low pressure turbine

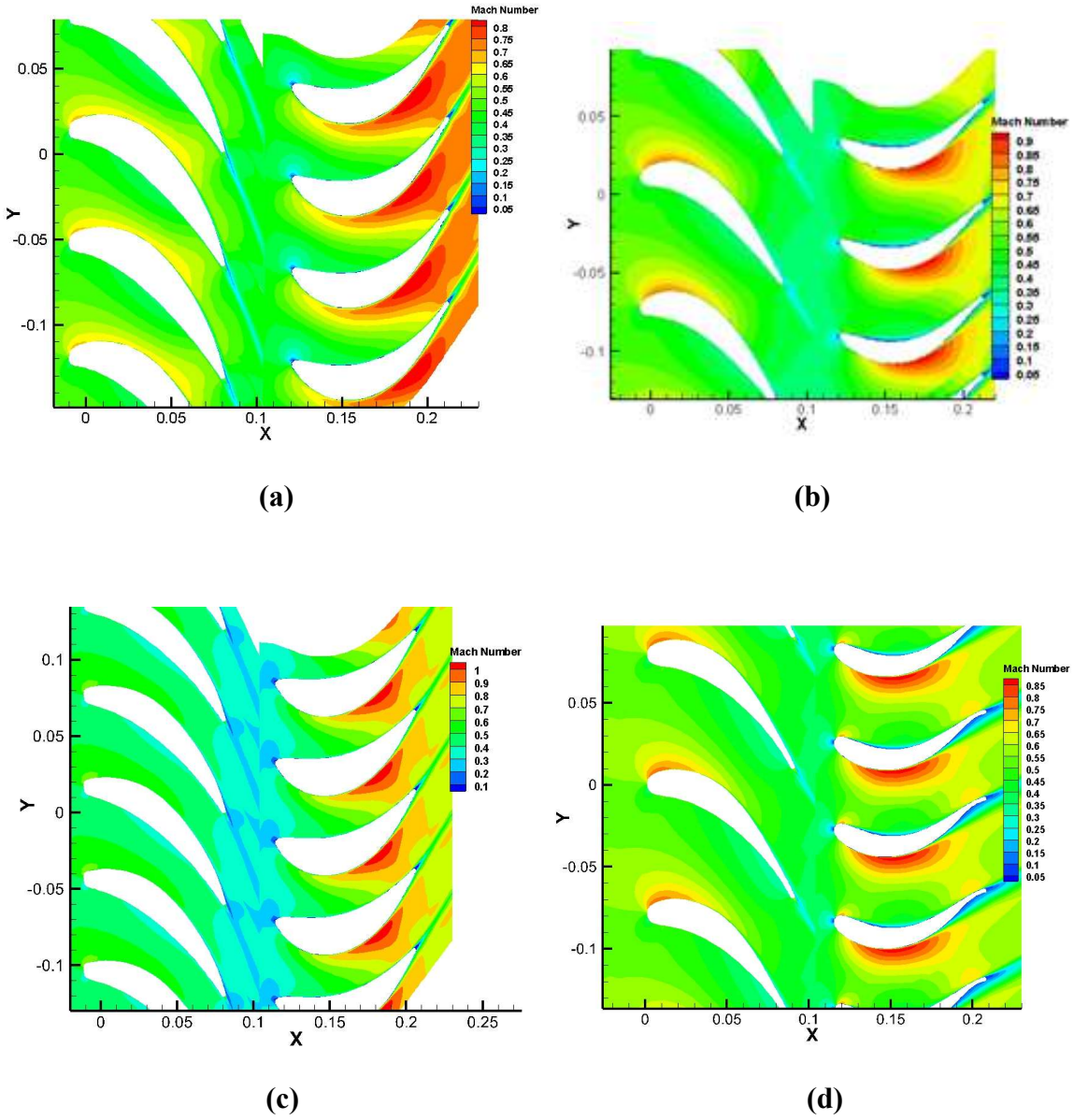

Figure 5.13. Mach number contours at midspan (a) Initial high pressure turbine, (b) initial low pressure turbine, (c) optimized high pressure turbine, (d) optimized low pressure turbine

5.3 Transition Mach Number Analysis

The aerothermal optimization results presented in the previous section indicate a significant increase in thrust and decrease in TSFC for the optimized engine. A simple analysis is presented to estimate the increase in the transition Mach number using the optimized engine. Figure 5.14 shows the Mach number trend versus thrust for the baseline and optimized engine at 40,000 ft. Since only one design point was optimized for the engine at 40,000 ft, the projected transition Mach number increase is calculated assuming the slope for the optimized engine is equivalent to that of the baseline engine.

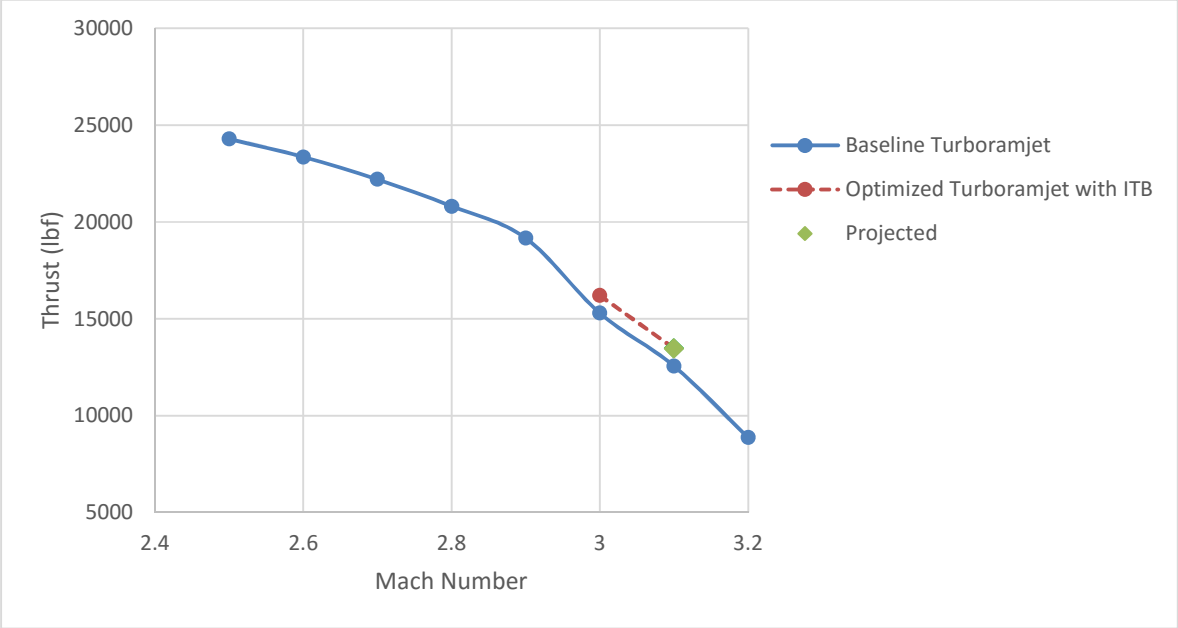

Figure 5.14. Projected transition Mach number for optimized turboramjet with ITB at 40,000 ft.

From the figure, the optimized turboramjet line intersects the thrust of the baseline turboramjet at a Mach number of 3.033. This is a 1.1% increase from the baseline Mach number

of 3.0. Figure 5.15 shows a comparison of the projected transition Mach numbers for the three design altitudes of 40,000 ft, 60,000 ft, and 80,000 ft.

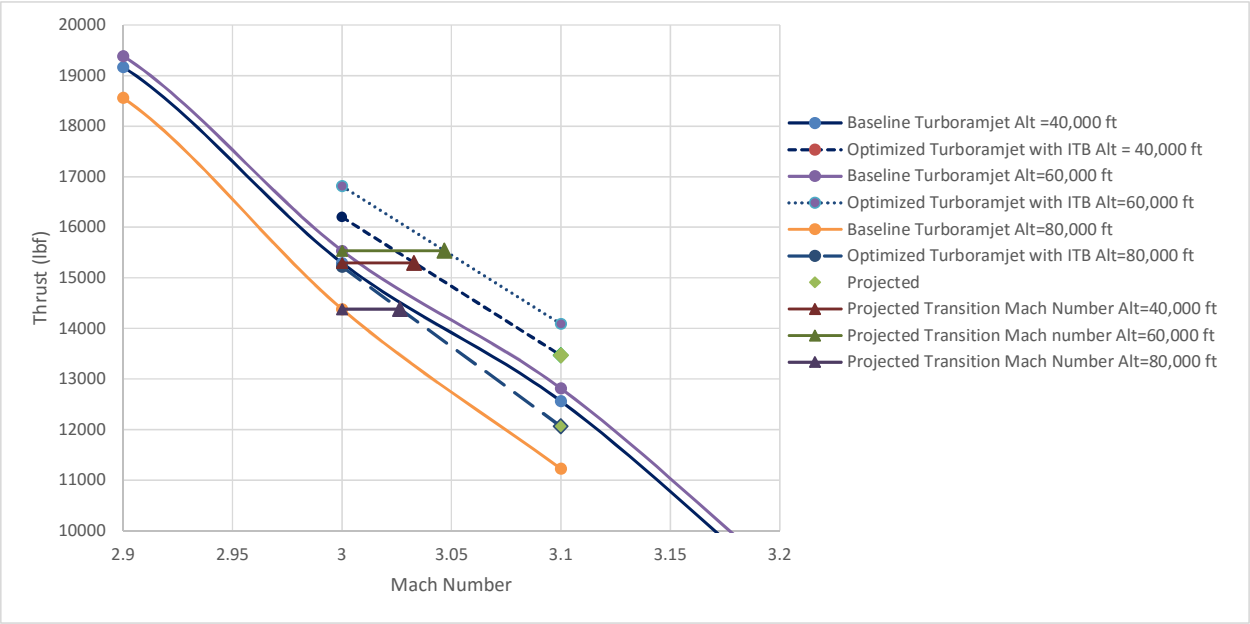

Figure 5.15. Projected transition Mach numbers for optimized turboramjet engines at 40,000 ft, 60,000 ft, and 80,000 ft.

By extending a line of zero slope from the transition thrust required at the transition Mach number of 3.0 from the baseline turboramjet to the projected line of the optimized turboramjet, the projected transition Mach number of the optimized turboramjets of the three design altitudes can be calculated. The transition Mach number for the turboramjet optimized at 60,000 feet is 3.047 and 3.027 for the turboramjet optimized at 80,000 feet. From this simple analysis it can be concluded that a very nominal gain in the transition Mach number is realized with the hot section optimization. Among the three design points analyzed, the largest gain for the transition Mach number is realized at 60,000 ft, with a 1.6% increase. Further design point optimization is warranted to achieve the optimal transition altitude. Although a very modest gain, the hot section optimization does result in an increase in the transition Mach number and holds

promise that additional component optimization within the engine will result in a further increase in the transition Mach number.

5.4 Turboramjet Optimization Conclusions

A hot section aerothermal optimization of a turboramjet with an interstage turbine burner was performed at three different design points (M=3.0 at altitudes of 40,000 ft, 60,000 ft, and 80,000 ft) that spanned the operational envelope of a turboramjet at the transition point from the turbine to ramjet cycle. Additionally, the turboramjet without the ITB was aerothermally optimized at the design point of M=3.0 and altitude of 40,000 ft. Table 5.6 lists and compares the thrust and TSFC performance results for the test cases as a result of the optimization against the baseline model.

Table 5.6 Turboramjet Optimization Comparison Results

			Model Optimization		Independent Turbine Optimization	
Test Case	Model	Design Point	Thrust increase from baseline (%)	TSFC decrease from baseline (%)	Thrust increase from baseline (%)	TSFC decrease from baseline (%)
1	Turboramjet no ITB	M=3.0, Alt=40,000	2.6	4.1	2.0	0.15
2	Turboramjet with ITB	M=3.0, Alt=40,000	5.9	7.5	1.3	-2.6
3	Turboramjet with ITB	M=3.0, Alt=60,000	3.6	7.9	3.8	1.6
4	Turboramjet with ITB	M=3.0, Alt=80,000	2.1	5.8	0.3	-2.4

The following conclusions can be drawn from the four test case results shown in Table 5.6. Test case 1 indicates a performance gain in thrust and TSFC as a result of the optimized high and low pressure turbine stages within the model. Test case 2 shows a performance gain in thrust and TSFC as a result of the interstage turbine burner and optimized turbines over that of the baseline turboramjet model with no ITB. Test cases 3 and 4 show a performance gain in both thrust and TSFC as a result of the turbine stages optimized within the model versus the baseline

turboramjet with an ITB. All of the test cases demonstrate the superiority of the turbine stages optimized within the model versus the independently optimized turbine stages.

In addition it was determined that all of the optimization cases resulted in an increase of the transition Mach number with a decrease in TSFC. The optimization at 60,000 ft resulted in the highest gain with a 1.6% in the transition Mach number. These preliminary results hold promise for future engine component optimizations which may further increase the transition Mach number.

Chapter 6

Conclusions and Future Work

A proposal for the optimization of a turboramjet hot section is presented. A high pressure and low pressure turbine stage was integrated into a turboramjet with an interstage turbine burner and an aerothermal turbine stage optimization was performed. This chapter provides conclusions achieved from the research presented as well as offers suggestions for future work.

6.1 Present Research Conclusions

A hybrid real coded genetic and evolution strategy algorithm was developed for use in the optimization of a three-dimensional turbine stage. Analysis of the algorithm indicated a simultaneous turbine stage optimization resulted in a superior solution to a successive optimization in which the stator was first optimized, followed by the rotor. A three-dimensional stage optimization was performed in which the stator and rotor hub, midspan, and tip airfoil profiles were optimized along with the lean, sweep, and twist stacking lines. Two-dimensional and three-dimensional structural considerations and other performance considerations such as a monatomically increasing Mach number on the suction surface and an acceptable uncovered turning angle were taken into account during the optimization. With 136 design variables in the stage optimization, parallel processing was utilized to reduce computation time by 98% from that of a single processor. A complete aerothermal stage optimization was performed within 35 hours, resulting in a 0.75% increase in stage efficiency and 0.85% in work output. These results

indicated the optimizer was suitable to perform stage optimization in an engine simulation program.

An F100-PW229 equivalent engine was modeled in the engine simulation program NPSS. A validation was performed in which the model matched performance values for that of an F100-PW229 engine within 2%. An ITB was included in the model and the performance was compared to that of the F100 equivalent engine without the ITB. A comparison of the TSFC of the engine with the ITB versus the engine without the ITB resulted in a 14% average decrease in TSFC at the same thrust level at a single altitude. A turboramjet engine was modeled in NPSS utilizing the equivalent F100 engine as the turbine cycle. An interstage turbine burner was added between the high and low pressure turbine stages, the model was paired with the turbine stage optimizer, and a complete aerothermal hot section optimization was performed at three different design points. The aerothermal hot section optimizations performed at the cycle transition Mach number of 3.0 and altitudes of 40,000 ft, 60,000 ft, and 80,000 ft resulted in a 2%-6% increase in thrust and 6%-8% improvement in TSFC over the baseline turboramjet engine. The turbine stage optimizations within the model proved superior to that of the independently optimized turbine stages at all design points.

6.2 Future Work

As in most research, much work has been done, yet much work remains. Due to the nature of this work, there are many different directions one could take to further this research. Improvements to the turbine stage optimizer and integrated model optimizer could further decrease computation time and allow for a more refined solution. In addition, this research paves the way for further optimization of individual engine components within the engine architecture.

The scope of this research was limited to a design hot section optimization. Off-design optimization is the next logical step for the turboramjet and may prove to be a critical exercise in ensuring optimal transition from the turbine to ramjet cycle.

6.2.1 Optimizer Future Work

First, the three-dimensional turbine stage optimizer could be improved in a variety of ways. Increasing the number of control points along the span of the blade for the lean, sweep, and twist geometry may lead to better spanwise definition of the blade geometry and eliminate some of the unconventional shapes that form due to the limited number of control points in that direction. This will increase computation time and a complete sensitivity study is warranted to arrive at the best combination of variables versus computation time. In addition, a more robust structural check to include FEA software rather than the rudimentary check implemented in this work may be warranted if this optimizer is to be used for experimental turbine blades rather than ones that currently exist.

The CFD grid used during the optimization process for this research does not alter as the turbine blade geometries change. This research utilized a high temperature turbine stage as the initial stage to be optimized in which the geometry was not expected to change dramatically given its application in a turboramjet. If this optimizer is to be used in which the turbine blade or stage geometry is expected to change dramatically from the initial parent solution, the grid must be programmed to change with the changing offspring geometries accordingly.

Since the scope of the current work was limited to providing a three-dimensional turbine stage optimizer which achieved convergence in a relatively short timeframe utilizing a viscous flow solver, no sensitivity studies were performed to determine the optimal variables for use in

the genetic algorithm implemented for the optimization. A sensitivity study involving the selection pool method, crossover method, population number, and mutation percentage is recommended to further reduce optimization computation time.

Next, improvements to the integration method of the turbine stage optimizer and NPSS model would serve to further reduce optimization computation time. Due to software limitations and access to the HPCC, only the stage CFD calculations for each offspring were performed in parallel. The model runs in NPSS of each offspring were performed in serial, increasing total optimization computation time by 80%. Implementing parallel processing for both the CFD solutions and the NPSS solutions could result in a complete optimization of high and low pressure stages within an NPSS model in under 1.5 days.

6.2.2 Engine Optimization Future Work

Due to the dearth of publically available data on turbine stage geometries for the F100 and the SR-72 engine currently in development, this research primarily demonstrates an optimization method in which three-dimensional turbine stage is optimized for user defined engine performance parameters. This research was motivated by the development of the new SR-72 turboramjet engine, and should turbine stage data and the engine design of an SR-72 become available, this method would prove highly useful in the optimization of the turbine stages for the engine. Additionally, as the vast majority of flight time is spent in an off-design condition, off-design optimization is warranted and necessary, especially to ensure an optimal transition from turbine to ramjet cycle.

The modular nature of the NPSS simulation software does not limit the optimization of the engine solely to the turbine, but allows for the optimization of additional components within

the engine. In theory, all engine components could be optimized simultaneously, utilizing the engine performance parameters as the objective function. This research provides for a tool in which a complete aircraft engine MDO may be performed by utilizing a modular high fidelity CFD solver along with parallel processing to perform individual component optimizations within an entire engine model, utilizing engine performance parameters as the objective function to obtain an optimally performing aircraft engine.

The blades of the turbine stages were aerothermally optimized utilizing current material performance specifications of the blade superalloy used in current jet engines. A turbine material study could be performed in which the performance of an engine could be optimized utilizing different blade materials.

References

[1]Harwood, M., "A More Fuel Efficient Air Force," *Air Force Times*, URL: http://archive.airforcetimes.com/article/20130922/NEWS04/309220006/A-more-fuel-efficient-Air-Force, 22 Sep 2013.

[2]McGarry, B., "Lockheed Unveils Plans for SR-72," *DefenseTech,* URL: http://defensetech.org/2013/11/04/lockheed-unveils-plans-for-sr-72/, 4 Nov 2013.

[3]Mateu, M. M., "Study of an Air-Breathing Engine for Hypersonic Flight," Technical Report, Sep 2013.

[4] "SR-71 and SR-72 Engine Cycle Comparison," *Aviation Week*, URL: http://awin.aviationweek.com/Portals/aweek/media/hyperengines/hyperengines6.html, 4 Nov 2013.

[5]Chen, M., Tang, H., Zhang, K., Hui, O., and Wang Y., "Turbine-Based Combined Cycle Propulsion System Integration Concept Design," *Proceedings of the Institution of Mechanical Engineers, Part G: Journal of Aerospace Engineering*, June 2012.

[6]Ouzts, P. J., "Mode Transition Design Considerations for an Airbreathing Combined-Cycle Hypersonic Vehicle," *15th AIAA International Space Planes and Hypersonic Systems and Technologies Conference*, AIAA, Dayton, Ohio, 28 April 2008.

[7]Hunt, J. L., "System Challenges for Hypersonic Vehicles," *Aerospatiale Espace & Defense*, NASA Langley Research Center.

[8]Clough, J., "Modeling and Optimization of Turbine Based Combined Cycle Engine Performance," M.S. Thesis, Aerospace Dept, University of Maryland, College Park, MD, 2004.

[9]Thomas, S. R., and Walker, J. F., "Overview of the TBCC Discipline," *National Aeronautics and Space Administration Annual Meeting*, 29 Sep 2009.

[10]Oates, Gordon C., *Aerothermodynamics of Gas Turbine and Rocket Propulsion*. Reston, Virginia: American Institute of Aeronautics and Astronautics, Inc., 1998.

[11]Mattingly, J. D., *Elements of Propulsion: Gas Turbines and Rockets*. Reston, Virginia: American Institute of Aeronautics and Astronautics, Inc., 2006.

[12]Mohammed, A., "Aerodynamic Shape Optimization of Axial Turbines in Three Dimensional Flow," Ph. D. Dissertation, Dept of Mech and Industrial Engineering, Concordia University, Montreal, Quebec, Canada, March 2012.

[13]Dennis, B.H., Egorov, I. N., Han, Z. X., Dulikravich, G. S., Poloni, C., "Multi-Objective Optimization of Turbomachinery Cascades for Minimum Loss, Maximum Loading, and Maximum Gap-to-Chord Ratio." *International Journal of Turbo and Jet Engines*, Vol. 18, 2001, pp. 201-210.

[14]Mengistu, T., Ghaly, W., and Mansour, T., "Global- and Local-Shape Aerodynamic Optimization of Turbine Blades," 11th *AIAA/ISSMO Multidisciplinary Analysis and Optimization Conference,* Portsmouth, Virginia, 6-8 September, 2006.

[15]Curriston, D., "Turbine Aerothermal Optimization Using Evolution Strategies," M.S. Thesis, Aerospace Department, Auburn University, Auburn, AL, May 2014.

[16]Oyama, A., Liou, M. S., Obayashi, S., "Transonic Axial-Flow Blade Optimization: Evolutionary Algorithms/Three-Dimensional Navier-Stokes Solver," *Journal of Propulsion and Power,* Vol. 20, No. 4, July-August 2004, pp. 612-619.

[17]Liu, F., and Sirignano, W. A., "Turbojet and Turbofan Engine Performance Increases Through Turbine Burners," *Journal of Propulsion and Power*, Vol. 17, No. 3, May-June 2001, pp. 695-705.

[18]Liew K. H., Urip, E., Yang, S. L., "Parametric Cycle Analysis of a Turbofan Engine with an Interstage Turbine Burner," *Journal of Propulsion and Power*, Vol. 21, No. 3, May-June 2005, pp. 546-551.

[19]Soon, L. A., "Two Combustor Engine for Military Applications," Ph.D Dissertation, Dept of Power and Propulsion, Cranfield University, Bedford, UK, 2009.

[20]Martins, J.R.R.A., Lambe, A.B., "Multidisciplinary Design Optimization: A Survey of Architectures", *AIAA Journal*, Vol. 51, No. 9 (2013), pp. 2049-2075.

[21]Sanberg, M., Kokkolaras, M., Aidanpaa, J.O., Isaksson, O., Larsson, T., "A Master-Model Approach to Whole Jet Engine Analysis and Design Optimization," *8th World Congress on Structural and Multidisciplinary Optimization*, Lisbon, Portugal, June 1-5, 2009.

[22]Borguet, S., Kelner, V., Leonard, O., "*Cycle Optimization of a Turbine Engine: an Approach Based on Genetic Algorithms,*" Proceedings of the 7th Belgian Congress on Theoretical and Applied Mechanics, Belgium, May 2006.

[23]NASA. NPSS User Guide. National Aeronautics and Space Administration, NASA John H. Glenn Research Center at Lewis Field, 21000 Brookpark Rd., Cleveland, OH 44135-3191, Revision W Edition, March 12, 2008. Software Release NPSS_1.6.5.

[24]Chen, B., and Yuan, X., "Advanced Aerodynamic Optimization System for Turbomachinery," *Journal of Turbomachinery*, Vol. 130, April 2008.

[25]Boyle, R. J., and Giel, P. W., "Three-Dimensional Navier-Stokes Heat Transfer Predictions for Turbulent Blade Flows," *Journal of Propulsion and Power,* Vol. 11, No. 6, Nov.-Dec. 1995, pp. 1179-1186.

[26]Oksuz, O., and Akmandor, I. S., "Multi-Objective Aerodynamic Optimization of Axial Turbine Blades Using a Novel Genetic Algorithm," *Journal of Turbomachinery*, Vol. 132, October 2010.

[27]Chima, R. V., "Calculation of Multistage Turbomachinery Using Steady Characteristic Boundary Conditions," *36th Aerospace Sciences Meeting & Exhibit*, Reno, Nevada, January 12-15, 1998.

[28]Giles, M. B., "Nonreflecting Boundary Conditions for Euler Equation Calculations," *AIAA Journal*, Vol. 28., No. 12, Dec. 1990, pp. 2050-2058.

[29]Denton, J. D., "The Calculations of Three-Dimensional Viscous Flow Through Multistage Turbomachines," ASME Paper 90-GT-19, June 1990.

[30]Whitney, W. J., Szanca, E. M., Bider, B., and Monroe, D. E., "Cold- Air Investigation of a Turbine for High- Temperature- Engine Application. III- Overall Stage Performance." NASA TN D-4389, 1968.

[31]Whitney, W. J., Szanca, S., Harold, J., Behning, F. P., "Cold- Air Investigation of a Turbine for High- Temperature- Engine Application. IV- Two Stage Turbine Performance." NASA TN D-6960, 1972.

[32]Mattingly, J. D., *Elements of Gas Turbine Propulsion*. NewYork: McGraw-Hill, 1996.

[33]Aungier, R. H., Turbine Aerodynamics: *Axial-Flow and Radial-Inflow Turbine Design and Analysis*. NewYork: ASME Press, 2006.

[34]Piegl, L., Tiller, W., *The NURBS Book*. New York: Springer-Verlag New York Inc., 1997.

[35]Chima, R. V., "TCGRID 3-D Grid Generator for Turbomachinery - User's Manual and Documentation, Version 400," July 2011.

[36]De Jong, K.A., *An Analysis of the Behavior of a Class of Genetic Adaptive Systems.* Doctoral Dissertation, University of Michigan, 1975.

[37]Holland, J.H., *Adaptation in Natural and Artificial Systems*. The University of Michigan Press, 1975.

[38]Eshelman, L. J. and Schaffer, J. D., "Real-Coded Genetic Algorithms and Interval Schemata," Foundations of Genetic Algorithms.2, Morgan Kaufmann Publishers, Inc., San Mateo, California, 1993, pp 187-202.

[39]Curriston, D. A., and Hartfield, R. J., "Power Turbine Blade Aerodynamic Optimization Using Non-Restrictive Evolution Strategies," Joint Propulsion Conference, 2013.

[40]Oyama, A., Obayashi, S., and Nakahashi, K.,"Wing Design Using Real-Coded Adaptive Range Genetic Algorithm," *1999 IEEE International Conference on Systems, Man and Cybernetics*, Tokyo, Japan, 1999.

[41]Goldman, L. J., and McLallin, K. L., "Cold Air Annular Cascade Investigation of Aerodynamic Performance of Core-Engine Cooled Turbine Vanes," NASA TM X-3224, April 1975.

[42]Chima, R. V., Yokota, J. W., "Numerical Analysis of Three-Dimensional Viscous Flows in Turbomachinery," AIAA J., Vol. 28, No. 5, May 1990, pp. 798-806.

[43]Chima, R. V., and Liou, M.-S., "Comparison of the AUSM+ and H-CUSP Schemes for Turbomachinery Applications," AIAA Paper 2003-4120. NASA TM-2003-212457.

[44]Young, J. B. and Wilcock, R. C., "Modelling the Air Cooled Gas Turbine: Part 2 – Coolant Flows and Losses," *Journal of Turbomachinery*, Vol.124, 2002, pp. 214 - 222.

[45]Wilock, R. C., Young, J. B. and Horlock, J. H., "The Effect of Turbine Blade Cooling on the Cycle Efficiency of Gas Turbine Power Cycle," *Journal of Engineering for Gas Turbines and* Power, Vol. 127, 2005, pp. 109 - 120.

[46]Dillow, C., "Inside America's Next Spyplane," *Popular Science*, URL: http://www.popsci.com/inside-americas-next-spyplane, 19 May 2015.

Appendix A

Pseudo Code for Model Optimization

Randomly select initial population of user defined size from initial parent solution

Evaluate fitness of initial population: for each offspring, run model from inlet to burner exit through NPSS (performed in series), utilize exit properties of burner as inlet properties to turbine and evaluate HPT solution through SWIFT (run in parallel), utilize exit properties of HPT as inlet properties to ITB, run solution through ITB model in NPSS (run in parallel), utilize exit properties of ITB as inlet properties to LPT and evaluate LPT solution through SWIFT (run in parallel), utilize exit properties of LPT as inlet properties to mixer, evaluate solution through rest of the model in NPSS and obtain objective function for each offspring.

Perform generation loop until stopping criteria is met {

Elitism: Select best two offspring for next generation

Roulette Wheel Method: Select parent pool based on fitness value of offspring

BLX-0.5 Crossover: Select two parents from pool and perform crossover to obtain two new offspring

Mutation: Implement one-fifth rule and mutate parent solution from pool based on defined offspring mutation percentage

Evaluate fitness of each offspring

}

Save and display results

Appendix B

F100 Equivalent Engine in NPSS

```
//-------------------------------------------------------------------
//    F100-PW-229 Baseline  E N G I N E
//   Configured to match the Soon's F100 Engine
//   Generated Spring 2013
//   Caitlin R. Thorn
//   SLS   D E S I G N    P O I N T    O N L Y
//  -------------------------------------------------------------------

//-------------------------------------------------------------------
//   F100 Equivalent   C O N F I G U R A T I O N
//-------------------------------------------------------------------

cout << "\t----------------------------------------------------\n"
    << "\t  F100 Baseline Engine                              \n"
    << "\t----------------------------------------------------\n\n";

// Set model name
MODELNAME = "F100 Baseline Engine";

//-----------------------------------------------------
// set the thermo package
//-----------------------------------------------------
setThermoPackage("CEA", "Air", "H20", "Jet-A(L)", "Jet-A(g)", "", "");
//-----------------------------------------------------
// include the standard intepretted things
//-----------------------------------------------------
#include <InterpIncludes.ncp>
#include "ncp.view"
#include "bleed_macros.fnc"
//-------------------------------------------------------------------
// #include the definition file for the user defined engine
// performance component
//-------------------------------------------------------------------
#include "EngPerf.int" ;
//-----------------------------------------------------
// MODEL DEFINITION
//-----------------------------------------------------
```

```
// ##################### FLIGHT CONDITIONS ####################
Element FlightConditions AMBIENT {
                        // Specify Design conditions
  alt = 0;              // design altitude (ft)
  MN = 0;               // design Mach number

  W = 248;//    // design mass flow (lbm/s)  111.5 kg
  Fl_O.switchTransport = "EQUIL";   //need this for CEA
}

//############################## Inlet ##############################

Element Inlet INLET {
 if ( AMBIENT.MN < 1 ) {
          INLET.eRamBase=1;
   }
   if ( AMBIENT.MN > 1) {
                if (AMBIENT.MN < 5){
                        INLET.eRamBase=1-0.075*(AMBIENT.MN-1)^1.35;
                }
                        else {
                                INLET.eRamBase=800/((AMBIENT.MN^4)+935);
}
}


          Fl_I.switchTransport = "EQUIL"; //need this for CEA
        Fl_O.switchTransport = "EQUIL";

}

// ###################### Splitter ################################
Element Splitter SPLIT {
         BPR =  0.36;  // Bypass Ratio

}

// ############################  FAN ################################
// here the fan represents the outer portion of the Low pressure
// compressor spool
Element Compressor Fan21 {
//        // use these lines if no compressor map is imlemented
//        effDes = 0.83;
//        PRdes = 3.55;

          // use these lines if compressor map is used...
```

```
        #include "fan.map" ; //Compressor sub-element map
        S_map.effDes = 0.83; //0.84;
        S_map.PRdes = 3.8;//3.8

}

// ###################### Bypass Duct/ Mixer ###################
Element Duct Bypass13 {
         dPqPbase = 0.03;       // pressure loss through bypass duct
}

// ################# High Pressure Compressor1 ##########################
Element Compressor HPC21 {
//      // use these lines if no compressor map is implemented
//      effDes = 0.895;         // set the design point
//                              // isentropic efficiency
//      PRdes = 5.6921;

        // use these lines if compressor map is used...
        #include "hpc.map";
        S_map.effDes = 0.84;//.85      // set the design point
                                // isentropic efficiency
        S_map.PRdes = 2.23;

}
Element Bleed BLD25 {
        // ============================== BLEEDS
============================
        // Three Bleeds are taken off of the back side of the High pressure
        // Compressor for turbine and environmental cooling.
        BleedOutPort BL_Cool_251 {
                fracW = 0.0;   // mass flow (5% for cooling LPT)
        }
        BleedOutPort BL_Cool_252 {
                fracW = 0.0;    // mass flow fraction (5% bleed)
        }

        BleedOutPort BL_Env_253 {
                fracW = 0.01;  // mass flow fraction (1% bleed)
        }
}

// ###################### High Pressure Compressor ###################
Element Compressor HPC25 {
//      // use these lines if no compressor map is imlemented
//      effDes = 0.895; //0.8855338;            // set the design point
```

```
                                                // isentropic efficiency
//          PRdes = 5.6921;

          // use these lines if compressor map is used...
          #include "hpc.map" ; // Compressor sub element map
          S_map.effDes = 0.84 ; // 0.85 ; set the maps design point
                                  // isentropic efficiency.
          S_map.PRdes = 14.52914798; // Set the pressure ratio at design

}

// ########################   Bleed starting point   ##########################
Element Bleed BLD3 {
          // ============================== BLEEDS
==============================
          // Three Bleeds are taken off of the back side of the High pressure
          // Compressor for turbine and environmental cooling.
          BleedOutPort BL_Cool_31 {
                    fracW =.108546;// mass flow
          }
          BleedOutPort BL_Cool_32 {
                    fracW =.0868424;// mass flow
          }

}
// ########################   Diffuser into Burner   ##########################
Element Diffuser DIF31 {
       dPqP= 0.025;

}

// ################################ Fuel ################################
Element FuelStart FUEL32{

//          LHV = 18400;          // BTU/lbm - Lower Heating Value of the fuel
                    // default is 18400 BTU/lbm.
          fuelType = "Jet-A(L)";
}

// ################################ Burner ##########################
Element Burner BRN36{
  effBase = 0.99;//        overall component efficiency
  dPqPBase = 1.0 - 0.95; // pressure drop across burner (dP/P)
  countFuelMax = 150;

  switchBurn = TEMPERATURE; // Change from burner default of
```

```
                                // Fuel-air Ratio (FAR) to TEMPERATURE
  TtCombOut = 3160.0;          //  Total temperature at exit (degrees Rankine)

  Fl_I.switchTransport = "EQUIL";
  Fl_O.switchTransport = "EQUIL";
}

// ############################ Bleed Mixer/IGV ############################
Element Bleed MIX40 {
        BleedInPort BlIn40{
//              Pscale = 0.88;
        }

}

// ############################ HP Turbine ############################
Element Turbine HPT41 {
        #include "hpt.map";  //High Pressure Turbine Map
        S_map.effDes = 0.86;//

}

// ############################ Bleed Mixer ############################
Element Bleed MIX44 {
        BleedInPort BlIn44{
//              Pscale = 0.68;
        }

}
// ############################ Bleed Mixer ############################
Element Bleed MIX45 {
        BleedInPort BlIn45{
//              Pscale = 0.68;
        }

}

// ############################ LP Turbine ############################
Element Turbine LPT45 {
        #include "lpt.map"  //Low Pressure Turbine Map
        S_map.effDes = 0.86;//

}
// ############################ Bleed Mixer ############################
Element Bleed MIX55 {
        BleedInPort BlIn55{
```

```
//                  Pscale = 0.68;
        }

}
Element Duct DCT5 {

         dPqPbase = 0.005;     // pressure loss through bypass duct
}
Element Mixer MIX50 {
      Fl_I1.MN=0.50;
}
// ########################   Bleed starting point   ##########################
Element Bleed BLD5 {
        // ============================== BLEEDS
==============================
        // Three Bleeds are taken off of the back side of the High pressure
        // Compressor for turbine and environmental cooling.
        BleedOutPort BL_Cool_51 {
                fracW = 0.08;   //  .08 for AB on
        }

}
// ########################   Diffuser into Burner   ##########################
Element Diffuser DIF6 {
dPqP= 0.025;
}

Element FuelStart FUEL61{

//      LHV = 18400;            // BTU/lbm - Lower Heating Value of the fuel
                // default is 18400 BTU/lbm.
        fuelType = "Jet-A(L)";

}

// ################################ Burner ##########################
Element Burner BRN61{
  effBase = 0.91;//.91  // overall component efficiency
  //dPqPBase = 1.0 - 0.95; // AB off
    dPqPBase = 1.0 - 0.84;    //AB on
  effChemBase = .96; //
  countFuelMax = 1000;
 // switchBurn = "FUEL";       //To turn AB "off" switchBurn = "FUEL"
 // Wfuel=0;                  // Wfuel = 0
   switchBurn = "TEMPERATURE";
   TtCombOut = 4133;//
```

```
  Fl_I.switchTransport = "EQUIL";
  Fl_O.switchTransport = "EQUIL";
}

Element Bleed MIX61 {
        BleedInPort BlIn61{
                Pscale = 0.68;
        }
}
Element Duct DCT7 {
         dPqPbase = 0.005;     // pressure loss through duct
}
// ######################### Nozzle #######################
Element Nozzle Noz8 {
        //Cfg = 0.995;
        Cv = 0.995; //
        dPqP = 1.0-0.97;
        PsExhName = "AMBIENT.Fl_O.Ps";
        switchType = "CON_DIV"; //
    Fl_O.MNfroz = 0.0;
        Fl_Oideal.MNfroz = 0.0;
}

// ########################## Terminate Flow ################
Element FlowEnd Sink39 {
        // sink for the environmental bleed...
}

Element FlowEnd NozSink9 {
        // sink for the core airflow
}

//
%%%%%%%%%%%%%%%%%%%%%%%%%%%%%%%%%%%%%%%%%%%%%%
%%%%%%
//          Put shafts in the model
//
%%%%%%%%%%%%%%%%%%%%%%%%%%%%%%%%%%%%%%%%%%%%%%
%%%%%%

//######################### Low-Pressure Shaft ################
Element Shaft LPShf {
        ShaftInputPort FAN, LPT ;
        Nmech = 11000.0;//
        inertia = 1.0;   // inertia is only needed for
                         // transient analysis
```

```
//        HPX = 0.0;      // Horsepower extracted from the shaft hp
          fracLoss = 1.0 - 0.97;  // Fractional loss on positive port
                                  // torque (1.0 - eta_m)
}

//########################## High Pressure Shaft ###################
Element Shaft HPShf {
          ShaftInputPort HPT, HPC25, HPC21 ;
          Nmech = 14000.0;//
          inertia = 1.0;
//        HPX = 143.178; // Horsepower extracted from the shaft in hp
                         // calculated to include additional shaft
                         // mechanical efficiency leading to the PTO
                      // 143.178 hp  = (105.7 kW)/(eta m = 0.99)
          fracLoss = 1.0 - 0.98; // Fractional loss on positive
                         //port torque (1.0 - eta_m)

}

//########################## Engine Performance ####################
Element EngPerf PERF{
}

//_____________________________________________________________________
//              Flow Connections                    //
//                                          //
//       This is where the flow is defined for the engine //
//_____________________________________________________________________//
//

//############## Ambient to Splitter ##########################
linkPorts( "AMBIENT.Fl_O",          "INLET.Fl_I",          "FL0" );
linkPorts( "INLET.Fl_O",     "SPLIT.Fl_I", "FL1" );

//##############  Bypass air     ###############################
linkPorts( "SPLIT.Fl_02",     "Fan21.Fl_I",            "FLb2" );
linkPorts( "Fan21.Fl_O",      "Bypass13.Fl_I",       "FLb3" );
linkPorts( "Bypass13.Fl_O",  "MIX50.Fl_I2",                  "FLb7" );

//############## Core Air Flow   ###############################
linkPorts( "SPLIT.Fl_01",     "HPC21.Fl_I",                   "FL2"  );
linkPorts( "HPC21.Fl_O",     "BLD25.Fl_I",                   "FL25" );
linkPorts( "BLD25.Fl_O",     "HPC25.Fl_I",          "FL3"  );
linkPorts( "HPC25.Fl_O",      "BLD3.Fl_I",                    "FL31" );
linkPorts( "BLD3.Fl_O",       "DIF31.Fl_I",                   "FL32" );
linkPorts( "DIF31.Fl_O",      "BRN36.Fl_I",                   "FL33" );
```

```
//###############   Fuel Flow   ################################
linkPorts( "FUEL32.Fu_O",   "BRN36.Fu_I",                   "Fu3"  );
linkPorts( "BRN36.Fl_O",     "MIX40.Fl_I",                   "FL4"  );
linkPorts( "MIX40.Fl_O",     "HPT41.Fl_I",                   "FL41" );
linkPorts( "HPT41.Fl_O",     "MIX44.Fl_I",                   "FL44" );
linkPorts( "MIX44.Fl_O",     "MIX45.Fl_I",                   "FL45" );
linkPorts( "MIX45.Fl_O",     "LPT45.Fl_I",                   "FL46" );
linkPorts( "LPT45.Fl_O",     "MIX55.Fl_I",                   "FL51" );
linkPorts( "MIX55.Fl_O",     "DCT5.Fl_I",            "FL52" );
linkPorts( "DCT5.Fl_O",      "MIX50.Fl_I1",                  "FL53" );
linkPorts( "MIX50.Fl_O",     "BLD5.Fl_I",            "FL54" );
linkPorts( "BLD5.Fl_O",      "DIF6.Fl_I",            "FL6" );
linkPorts( "DIF6.Fl_O",      "BRN61.Fl_I",                   "FL61" );
linkPorts( "BRN61.Fl_O",     "MIX61.Fl_I",                   "FL62" );
linkPorts( "MIX61.Fl_O",     "DCT7.Fl_I",            "FL63" );
linkPorts( "DCT7.Fl_O",      "Noz8.Fl_I",            "FL71" );
linkPorts( "Noz8.Fl_O",      "NozSink9.Fl_I",        "FL8"  );
//###############   Fuel Flow Afterburner  ####################
linkPorts( "FUEL61.Fu_O",   "BRN61.Fu_I",                   "Fu6"  );

//############### Bleed port linkage ############################
 linkPorts( "BLD25.BL_Cool_251",  "MIX45.BlIn45",       "BL 1");
 linkPorts( "BLD25.BL_Cool_252",  "MIX55.BlIn55",       "BL 2");
 linkPorts( "BLD25.BL_Env_253",          "Sink39.Fl_I",   "BL 3");
 linkPorts( "BLD3.BL_Cool_31",           "MIX40.BlIn40",          "BL 4");
 linkPorts( "BLD3.BL_Cool_32",     "MIX44.BlIn44",       "BL 5");
 linkPorts( "BLD5.BL_Cool_51",     "MIX61.BlIn61",       "BL 6");

//$$$$$$$$$$$$$$$$$$$$$$$$$$$$$$$$$$$$$$$$$$$$$$$$$$
//         Mechanical (Shaft) connections
// $$$$$$$$$$$$$$$$$$$$$$$$$$$$$$$$$$$$$$$$$$$$$$$$$

//################ Low-Pressure Spool #########################
linkPorts("Fan21.Sh_O", "LPShf.FAN",       "LP3");
linkPorts("LPT45.Sh_O", "LPShf.LPT",       "LP2");

//############### High-Pressure Spool ########################
linkPorts("HPC21.Sh_O",     "HPShf.HPC21",       "HP1");
linkPorts("HPC25.Sh_O",     "HPShf.HPC25",       "HP2");
linkPorts("HPT41.Sh_O",     "HPShf.HPT",         "HP3");

// ^^^^^^^^^^^^^^^^^^^^^^^^^^^^^^^^^^^^^^^^^^^^^^^^^^^^^^^^^^^
//   Begin Run Definition
// vvvvvvvvvvvvvvvvvvvvvvvvvvvvvvvvvvvvvvvvvvvvvvvvvvvvvvvvvvv

cout << "^^^^^^^^^^^^^^^^^^^^^^^^^^^^^^^^^^^^^^^^^^^^^^^^^^^\n"
```

```
<< "         Begin Run Input definitions          \n "
<< "vvvvvvvvvvvvvvvvvvvvvvvvvvvvvvvvvvvvvvvvvvvvvvvvvvvvvvv\n\n";
```

Appendix C

Sample NPSS Output

```
NCP        NPSS_1.6.5 - Rev: --     model:F100 Baseline >     run by:      Caitlin    solutionMode= STEADY_STATE    converge=    1    case:    1
time:  0.000    timeStep:0.0500     therm_package:   CEA      Mode:    DESIGN         iter/pas/Jac/Broy= 17/ 19/ 1/15     run: 08/06/15 14:23:27

                    Summary Output Data
    MN       alt    dTs        W        Fg        Fn      TSFC      Wfuel      WAR      OPR
 0.000       0.0     0.00    248.0   28505.1   28505.1    2.0534   58530.90   0.0000   32.400

         INPUT FLOW
                        W        Pt        Tt        ht       FAR        Wc        Ps        Ts      Aphy       MN      gamt
FL0  INLET.Fl_I     248.00    14.696    518.67      6.18    0.0000    248.00    14.696    518.67  -----.-   0.0000   1.40023
FL1  SPLIT.Fl_I     248.00    14.696    518.67      6.18    0.0000    248.00     0.000      0.00       0.0   0.0000   1.40023
FLb2 Fan21.Fl_I      65.65    14.696    518.67      6.18    0.0000     65.65     0.000      0.00       0.0   0.0000   1.40023
FLb3 Bypass13.Fl>    65.65    55.845    807.00     63.42    0.0000     21.55     0.000      0.00       0.0   0.0000   1.39144
FL2  HPC21.Fl_I     182.35    14.696    518.67      6.18    0.0000    182.35     0.000      0.00       0.0   0.0000   1.40023
FL25 BLD25.Fl_I     182.35    32.772    677.30     31.97    0.0000     93.44     0.000      0.00       0.0   0.0000   1.39668
FL3  HPC25.Fl_I     180.53    32.772    677.30     31.97    0.0000     92.51     0.000      0.00       0.0   0.0000   1.39668
FL31 BLD3.Fl_I      180.53   476.150   1547.46    251.70    0.0000      9.62     0.000      0.00       0.0   0.0000   1.34774
FL32 DIF31.Fl_I     145.26   476.150   1547.46    251.70    0.0000      7.74     0.000      0.00       0.0   0.0000   1.34774
FL33 BRN36.Fl_I     145.26   464.247   1547.46    251.70    0.0000      7.94     0.000      0.00       0.0   0.0000   1.34774
FL4  MIX40.Fl_I     149.10   441.034   3159.97    245.22    0.0264     12.26     0.000      0.00       0.0   0.0000   1.27437
FL41 HPT41.Fl_I     168.69   441.034   2989.90    245.97    0.0233     13.50     0.000      0.00       0.0   0.0000   1.28081
FL44 MIX44.Fl_I     168.69    60.554   2054.71     36.06    0.0233     81.49     0.000      0.00       0.0   0.0000   1.30939
FL45 MIX45.Fl_I     184.37    60.554   2013.96     11.59    0.0213     88.17     0.000      0.00       0.0   0.0000   1.31221
FL46 LPT45.Fl_I     184.37    60.554   2013.96     11.59    0.0213     88.17     0.000      0.00       0.0   0.0000   1.31221
FL51 MIX55.Fl_I     184.37    48.552   1924.91     37.14    0.0213    107.51     0.000      0.00       0.0   0.0000   1.31568
FL52 DCT5.Fl_I      184.37    48.552   1924.91     37.14    0.0213    107.51     0.000      0.00       0.0   0.0000   1.31568
FL53 MIX50.Fl_I1    184.37    48.309   1924.91     37.14    0.0213    108.05    41.098   1851.42     432.9   0.5000   1.31568
FLb7 MIX50.Fl_I2     65.65    54.169    807.00     63.42    0.0000     22.22    41.098    746.53      74.2   0.6419   1.39144
FL54 BLD5.Fl_I      250.02    48.851   1651.77     10.74    0.0156    134.22    40.400   1575.14     507.0   0.5398   1.33157
FL6  DIF6.Fl_I      230.02    48.851   1651.77     10.74    0.0156    123.48     0.000      0.00       0.0   0.0000   1.33157
FL61 BRN61.Fl_I     230.02    47.630   1651.77     10.74    0.0156    126.65     0.000      0.00       0.0   0.0000   1.33157
FL62 MIX61.Fl_I     242.43    40.009   4132.94     61.87    0.0704    251.37     0.000      0.00       0.0   0.0000   1.19159
FL63 DCT7.Fl_I      262.44    40.009   4076.90     57.97    0.0660    270.26     0.000      0.00       0.0   0.0000   1.19371
FL71 Noz8.Fl_I      262.44    39.809   4076.71     57.97    0.0660    271.61     0.000      0.00       0.0   0.0000   1.19366
BL 3 Sink39.Fl_I      1.82    32.772    677.30     31.97    0.0000      0.93     0.000      0.00       0.0   0.0000   1.39668
FL8  NozSink9.Fl>   262.44    38.615   4075.60     57.97    0.0660    279.97    14.696   3347.33     912.6   1.3022   1.19335

         INLETS                                                                  COMPRESSORS & TURBINES
             eRam      Afs     Fram                                                      Wc       PR       TR    efPoly       eff        Nc       pwr
INLET       1.0000  ----.--      0.0                                  Fan21         65.65    3.800   1.5559    0.8581    0.8300  11000.0   -6464.8
                                                                      HPC21        182.35    2.230   1.3058    0.8568    0.8400  14000.0   -9843.6
           DUCTS                                                      HPC25         92.51   14.529   2.2848    0.8853    0.8400  12251.3  -56124.7
               dPqP    MNin     Aphy                                 HPT41         13.50    7.283   1.4551    0.8290    0.8600    256.0   67314.6
Bypass13     0.03000  0.0000     0.00                                LPT45         88.17    1.247   1.0463    0.8567    0.8600    245.1    6664.8
DCT5         0.00500  0.0000     0.00
DCT7         0.00500  0.0000     0.00


                                                                          MAP POINTS - COMPRESSORS & TURBINES
                                                                             WcMap    PRmap                      effMap    NcMap   R/parm
         SPLITTERS                                                   Fan21   1441.71    1.677                     0.8703      1.0   2.0000
               BPR   dP/P1   dP/P2                                  HPC21     123.57   24.136                     0.8216      1.0   2.0000
SPLIT       0.36000  0.0000  0.0000                                 HPC25     123.57   24.136                     0.8216      1.0   2.0000
                                                                    HPT41      16.04    1.000                     0.5950      1.0  76.0000
         MIXERS                                                     LPT45      78.56    4.271                     0.9171    100.0  68.0000
                Aout   nStations
MIX50                                                                    ADDERS AND SCALARS
                                                                         s_WcAud  a_WcAud  s_effAud  a_effAud
         BURNERS                                                Fan21    1.0000   0.0000    1.0000    0.0000
              TtOut      eff     dPqP         LHV      Wfuel       FAR  HPC21    1.0000   0.0000    1.0000    0.0000
BRN36         3160.00   0.9900   0.0500               3.83988   0.02644  HPC25    1.0000   0.0000    1.0000    0.0000
BRN61         4133.00   0.9100   0.1600              12.41870   0.07043  HPT41    1.0000   0.0000    1.0000    0.0000    1.0000    0.0000
                                                                         LPT45    1.0000   0.0000    1.0000    0.0000    1.0000    0.0000
         NOZZLES
             PR     Cfg    CdTh      Cv      Ath  Vactual       Fg
Noz8       2.628  0.9810  1.0000  0.9950   862.06   3494.7  28505.1

         SHAFTS
           Nmech    trqIn    trqNet    pwrIn     HPX    dNqdt
LPShf    11000.0   3182.2    0.0046   6664.8    0.00     0.04
HPShf    14000.0  25253.1   -0.0004  67314.6    0.00    -0.00

         INERTIA
         inertia  inertiaSum
LPShf       1.00        1.00
HPShf       1.00        1.00
Fan21       0.00
HPC21       0.00
HPC25       0.00
HPT41       0.00
LPT45       0.00
```

Appendix D

Sample SWIFT Input Data

'SWIFT input data'

&nl2 nstg=4.000000 ndis=2.000000 icdup=1.000000 cfl=5.600000 avisc2=1.000000 avisc4=1.000000 irs=1.000000 eps=1.500000 itmax=1500.000000 ivdt=1.000000 ipc=0.000000 refms=0.500000 refmr=0.600000 pck=0.350000 hcuspk=0.050000 ausmk=0.400000 &end

&nl3 ibcinw=1.000000 iqin=0.000000 ires=10.000000 iresti=0.000000 iresto=1.000000 &end

&nl4 igeom=1.000000 ga=1.400000 om=-0.862200 prat=0.322300 &end

&nl5 ilt=5.000000 isst=0.000000 itur=2.000000 renr=7140000.000000 prnr=0.700000 tw=0.650320 vispwr=0.667000 prtr=0.900000 cmutm=0.000000 jedge=20.000000 kedgh=15.000000 kedgt=42.000000 iltin=2.000000 dblh=0.006000 dblt=0.006000 tintens=0.030000 tmuinf=0.100000 hrough=0.000000 &end

&nl6 iqav=2.000000 ko=23 24 25 ismout=1.000000 &end

row P0 Mx Mt Mr T0

3.000000 0.550000 0.428000 0.000000 0.000000 0.870000
4.000000 0.520000 0.406000 -0.763700 0.000000 0.850000
5.000000 0.300000 0.503200 0.088700 0.000000 0.800000

Appendix E

Sample TCGrid Input Data

'TCGrid Input Data'

&nam1 merid=0 im=147 jm=36 km=57 itl=24 icap=15 igeom=0 iclus=1 icluss=1 iclusw=1 iclus2d=1 iclusmt=1 i2d=21 k2d=19 igch=0 igin=1 imi=17 igclh=0 igclt=0 jmt=0 kmt=13 &end

&nam2 nle=11.000000 nte=12.000000 dsle=0.002500 dste=0.000300 dsthr=1.000000 dswte=0.000300 dswex=0.002000 dsmin=0.000007 dsmax=0.001000 dsin=0.001500 dsra=0.480000 gap=0.065270 rcorn=0.000000 dshub=0.000010 dstip=0.000010 cltip=0.000000 dsclt=0.000020 &end

&nam3 iterm=200.000000 idbg=0 0 0 0 0 0 0 0 0 aabb=0.500000 ccdd=0.450000 &end

&nam4 zbc= -.05 -.018 .105 -.05 -.018 .105 rbc= .4447 .4447 .4447 .60451 .60451 .60451 &end

&nam5 iswift=1.000000 ztrans=0.015000 tflip=0.000000 dslap=0.001000 fswake=0.800000 iwakex=1.000000 jwakex=2.000000 &end

'Hub/Tib/Blade points'

8.000000 8.000000
-0.100000 0.176500 0.177000 0.178000 0.186000 0.187000 0.207600 0.500000
0.444700 0.444700 0.444700 0.444700 0.444700 0.444700 0.444700 0.444700
-0.100000 0.176500 0.177000 0.178000 0.186000 0.187000 0.207600 0.500000
0.604510 0.604510 0.604510 0.604510 0.604510 0.604510 0.604510 0.604510

19.000000 229 50
0.069856 0.069732 0.069604 0.069473 0.069340 0.069206 0.069073 0.068942
0.068814 0.068691 0.068573 0.068462 0.068358 0.068263 0.068178 0.068103
0.066754 0.065408 0.064065 0.062725 0.061389 0.060057 0.058729 0.057404
0.056084 0.054768 0.053456 0.052148 0.050845 0.049547 0.048254 0.046965
0.045682 0.044403 0.043130 0.041863 0.040601 0.039345 0.038095 0.036850
0.035612 0.034381 0.033155 0.031937 0.030725 0.029520 0.028323 0.027132
0.025949 0.024774 0.023607 0.022448 0.021297 0.020154 0.019020 0.017895
0.016779 0.015672 0.014574 0.013486 0.012408 0.011341 0.010283 0.009236
0.008201 0.007176 0.006162 0.005160 0.004170 0.003193 0.002227 0.001275
0.000335 -0.000591 -0.001504 -0.002402 -0.003287 -0.004156 -0.005011 -0.005851 -
0.006675 -0.007483 -0.008275 -0.009050 -0.009808 -0.010548 -0.011271 -0.011976 -

0.012662 -0.013328 -0.013976 -0.014603 -0.015211 -0.015797 -0.016362 -0.016906 -
0.017427 -0.017925 -0.018401 -0.018853 -0.019281 -0.019684 -0.020062 -0.020414 -
0.020740 -0.021039 -0.021310 -0.021554 -0.021769 -0.021955 -0.022111 -0.022237 -
0.022332 -0.022395 -0.022426 -0.022398 -0.022278 -0.022070 -0.021779 -0.021411 -
0.020969 -0.020458 -0.019882 -0.019245 -0.018551 -0.017804 -0.017006 -0.016163 -
0.015277 -0.014351 -0.013389 -0.012394 -0.011368 -0.010315 -0.009236 -0.008135 -
0.007014 -0.005875 -0.004720 -0.003552 -0.002373 -0.001185 0.000012 0.001214
0.002421 0.003630 0.004841 0.006052 0.007261 0.008468 0.009672 0.010871
0.012065 0.013252 0.014432 0.015604 0.016768 0.017922 0.019068 0.020203
0.021327 0.022441 0.023545 0.024636 0.025717 0.026786 0.027844 0.028890
0.029925 0.030948 0.031961 (etc.)

Appendix F

Three-Dimensional Pressure Contours

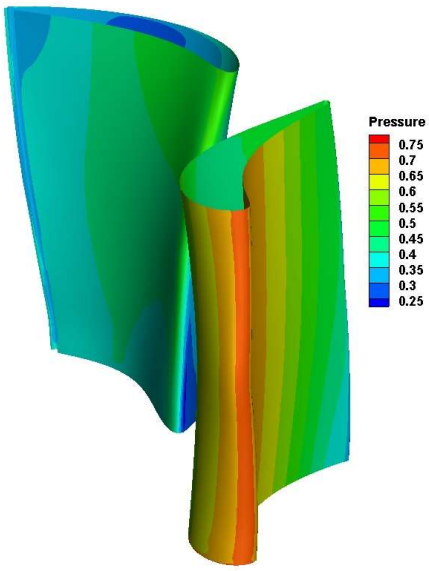

(a)

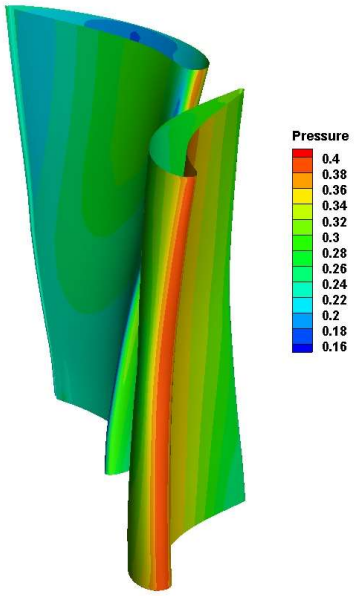

(b)

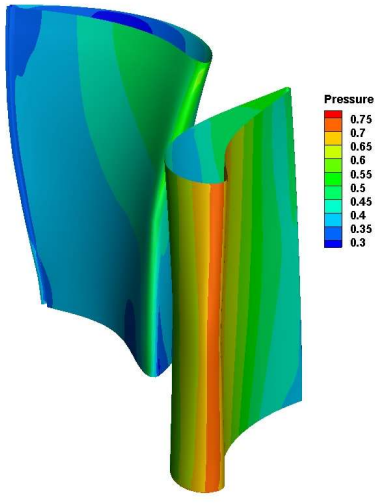

(c)

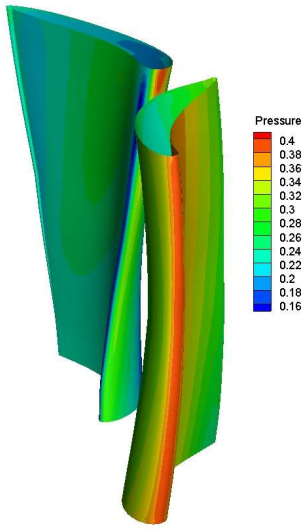

(d)

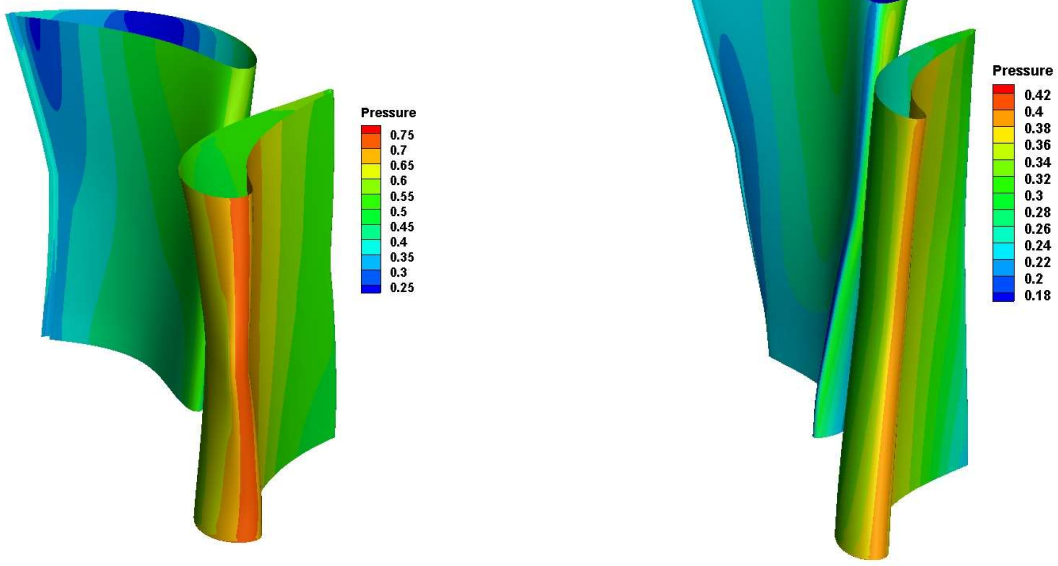

(e) **(f)**

Figure F.1 HPT and LPT pressure contours optimized turboramjet with ITB. M = 40,000 ft (a)-(b), M = 60,000 ft (c)-(d), M = 80,000 ft (e)-(f)